KEK Proceedings 96-10
November 1996
R/D

Proceedings of the Sixth EGS4 Users' Meeting in Japan

July 29 - 31, 1996.

KEK, Tsukuba, Japan

Edited by

H. Hirayama, Y. Namito and S. Ban

NATIONAL LABORATORY FOR
HIGH ENERGY PHYSICS

National Laboratory for High Energy Physics, 1996

KEK Reports are available from:

Technical Information & Library
National Laboratory for High Energy Physics
1-1 Oho, Tsukuba-shi
Ibaraki-ken, 305
JAPAN

Phone: 0298-64-5136
Telex: 3652-534 (Domestic)
(0)3652-534 (International)
Fax: 0298-64-4604
Cable: KEK OHO
E-mail: Library@kekvax.kek.jp (Internet Address)
Internet: http://www.kek.jp

FOREWARD

The Sixth EGS4 Users' Meeting in Japan was held at the National Laboratory for High Energy Physics (KEK) from July 29 to 31. The meeting has been hosted by the Radiation Safety Control Center, KEK. Nearly 100 participants attended the meeting.

The meeting was divided into two parts. Lectures concerning the EGS4 System, Mortran, User code, HOWFAR, how to use PEGS4, how to write source routine and the EGS4 shower display system on PC were given at the first half. Practices to install the EGS4 system on the UNIX workstation or PC and to run PEGS4 or user code were also performed. In the later half, 15 talks related EGS4 were presented. The talks covered the wide fields, like the medical application and the calculation of various detector response etc. These talks were very useful to exchange the information between the researchers in the different fields.

Finally, we would like to express our great appreciation to all authors who have prepared manuscript quickly for the publication of this proceedings.

Hideo Hirayama
Yoshihito Namito
Syuichi Ban
Radiation Safety Control Center
KEK, National Laboratory for High Energy Physics

CONTENTS

IMPLEMENTATION OF THE ELECTRON IMPACT IONIZATION INTO THE EGS4 CODE

Y. NAMITO and H.HIRAYAMA

National Laboratory for High Energy Physics (KEK)
Oho, Tsukuba-shi, Ibaraki-ken, 305, Japan

Abstract

A modification to the general-purpose Monte-Carlo electron-photon transport code EGS4 [2] was made in order to include K-shell electron-impact ionization. Gryziński's formula of electron-impact ionization is employed for the calculation along with a relativistic correction for the formula. The ratio of electron impact ionization cross section to the Møller scattering cross section is prepared by the PEGS4 program, and is used in the EGS4 calculation. A simulation of the photon emission from a Sn target for an incident 100 keV electron was performed using the improved EGS4 code; the calculated K-X ray and bremsstrahlung photon spectra agreed well with the measurements.

1. Introduction

When an electron beam hits a target, bremsstrahlung photons and characteristic X rays are generated. The characteristic X rays are emitted after the production of vacancies in the inner shells. Two major channels exist for the production of vacancies in the inner shells i.e.:

1. A vacancy is created in a photoelectric effect by bremsstrahlung photons.
2. The incident electron scatters an inner-shell electron (electron impact ionization:EII) and creates a vacancy in the inner shell.

In the case that the electron kinetic energy is less than a few 100 keV, channel 1 is narrow since the bremsstrahlung cross section is small and the contribution of channel 2 is compatible to the former one.

The authors calculated the photon spectra from targets irradiated by electrons with an energy less than a few MeV using the EGS4 code, and obtained agreement with a measurement in the part of bremsstrahlung [2, 3]. However the EGS4 calculation and

measurement differed apparently concerning the part of the characteristic X ray; also, ignorance about the electron-impact ionization in the EGS4 calculation was supposed to be the reason of the discrepancy (See Fig.1).

In this study, a modification to the EGS4 was made in order to include the electron-impact ionization. The immediate purpose of the modification is to determine the reason for the discrepancy concerning the characteristic X ray. Electron-impact ionization makes a substantial contribution in a simulation of an ordinary-type X ray generator which uses an electron beam of the energy up to a few 100 keV. A simulation of this kind of X-ray generator using EGS4 thus becomes possible.

2. Electron impact ionization cross section

Powell has reviewed measurement data and formula concerning the electron-impact ionization cross section.[4] The following authors have developed EII formulas. Gryziński developed the EII formula from classical theory [6, 7, 8]. Gryziński's formula agrees reasonably well with a measurement in the case that a relativistic correction is applied to the formula. Without a relativistic correction, Gryziński's formula apparently differs from measurements in the case that the incident electron kinetic energy(E_K) is greater than a few hundred keV. Kolbenstvedt made a EII cross section formula for a K-shell electron by adding the contribution due to ionization by a virtual photoeffect and a contribution due to close collisions [9]. Kolbenstvedt's formula apparently differs from Gryziński's formula in the case $E_K <\sim 4$ times the binding energy of the orbit electron (E_B); the former's cross section is about 0.7-0.8 times the peak value of the the cross section; the latter's cross section approaches 0 when E_K approaches E_B. Seltzer made a numerical evaluation of the EII cross section, and obtained good agreement with measurements over a wide range of incident electron energies [10].

Deiwiks et al measured the positron and electron impact ionization cross section[5]. Deiwiks et al have indicated that the positron impact-ionization cross section is apparently smaller than the electron-impact ionization in the case that the positron kinetic energy is less than $\sim 5 \times E_B$.

The SANDYL code [11] treats the electron impact ionization using Gryziński's formula in a nonrelativistic version. The ETRAN code treats K-shell ionization by electron impact using Kolbenstvedt's cross section.[12, 13]

3. Method of calculation

Gryziński's formula for the electron-impact ionization [7, 8] is used together with a relativistic correction, because this formula agrees well with measurements, and its value

near to E_B is close to Seltzer's numerical evaluation.

$$\sigma_{EII} = \frac{0.0656 N_e}{E_B^2} \frac{f_V^{(0)rel}}{f_V^{(0)}} \frac{1}{x} \left(\frac{x-1}{x+1}\right)^{3/2} \left[1 + \frac{2}{3}\left(1 - \frac{1}{2x}\right) \ln\left\{2.7 + (x-1)^{1/2}\right\}\right], \quad (1)$$

$$f_V^{(0)} = f_V|_{\theta=\pi/2} = \left(\frac{v_1}{v_2}\right)^2 \left(\frac{v_2^2}{v_2^2 + v_1^2}\right)^{3/2} = \frac{E_B}{E_K}\left(\frac{E_K}{E_K + E_B}\right)^{3/2}, \quad (2)$$

$$f_V^{(0)rel} = \frac{\kappa_1}{\kappa_2}\frac{2+\kappa_1}{2+\kappa_2}\left(\frac{1+\kappa_2}{1+\kappa_1}\right)^2 \times \left\{\frac{(1+\kappa_2)^2}{(1+\kappa_2)^2 + (\kappa_1/\kappa_2)\left((2+\kappa_1)/(2+\kappa_2)\right)\left((1+\kappa_2)/(1+\kappa_1)\right)^2}\right\}^{3/2}, \quad (3)$$

$$\kappa_1 = \frac{E_B}{m_0 c^2}, \quad \kappa_2 = \frac{E_K}{m_0 c^2}, \quad x = \frac{E_K}{E_B}. \quad (4)$$

Here, σ_{EII} is the vacancy-creation cross section due to electron-impact ionization (barn/atom), N_e is the number of electrons in a shell (=2 in the case of the K shell), E_B and E_K are the binding energy of the orbit electron (MeV) and the incident-electron kinetic energy(MeV), respectively. $f_v^{(0)}$ and $f_v^{(0)rel}$ are velocity functions in the nonrelativistic and relativistic formula, respectively. m_0c^2 is the electron rest mass.

After a vacancy is created in a K shell by EII, a K-X ray or Auger electron is sampled using the K-shell fluorescence yield. In the case of K-X-ray emission, K_{α_1}, K_{α_2}, K_{β_1} and K_{β_2} are sampled according to the intensity ratio. The calculation method to treat 4 kinds of K-X rays was taken from Hirayama's improvement of EGS4 [14]. Auger electron is not followed.

When a vacancy is created in the K shell by EII, K-shell binding energy is subtracted from the energy of either one of the two electrons related to the Møller scattering. This energy subtraction is done in order to maintain energy conservation. The difference in the K-shell binding energy and K-X ray energy is deposited locally. In the case that EII occurs, and no K-X ray is generated (i.e. Auger electron emission), the K-shell binding energy is deposited locally.

In this study, only K-shell ionization by electron impact was treated; also, neither L, M and outer-shell ionization by electron impact nor any shell ionization by positron impact was treated.

4. Example of calculation result

Placious measured bremsstrahlung and the K-X ray from various targets [15, 16]. In Pacious's measurement, 50 or 100 keV electrons are normally incident on the target, and those photons emitted toward 70° and 110° from the direction of the incident electron is measured. Among the various measured spectra, photons from a Sn target (target thickness, 21.6 mg/cm^2; incident electron kinetic energy, 100 keV) were simulated by the improved EGS4 code, since the K-X ray appears clearly in the spectra.

The EGS4 calculations were performed both with and without electron-impact ionization. The improvements of EGS4(PRESTA [17], use of ICRU-37/NBS radiative stopping powers [18] and improved angular distribution of bremsstrahlung photons [19]) were employed in all of the EGS4 calculations. As discussed in the appendix, the default EGS4 tend to underestimate the Møller scattering and bremsstrahlung in the case that the electron energy is less than about 5 MeV. Since the electron-impact ionization is calculated using the ratio of EII to the Møller scattering, an underestimation of the Møller scattering also causes an underestimation of EII. This underestimation of the bremsstrahlung and Møller scattering is corrected, as discussed in the appendix.

A comparison of the EGS4 calculation with measurements is shown in Fig. 1. The K-X ray intensity by EGS4 with EII agreed with the measurement within 10% in the spectra at both 70° and 110°, while the K-X ray intensity by EGS4 without EII was only about half of the measured intensity. The K-X rays generated in the photoelectric effect by the bremsstrahlung photons and the K-X rays generated in electron-impact ionization were of the same order. ¿From this point, the reason for the under estimate of the K-X ray intensity in the previous EGS4 calculation [3] has been found to be an ignorance of the electron-impact ionization. Also, an EGS4 calculation with EII agreed well with ETRAN calculation (not shown), which also considers EII [16].

Appendix A. Modification of the program

The following subroutines and functions of PEGS4 were modified or added in order to implement electron-impact ionization:

- EIITM: Calculate the K-shell electron-impact ionization cross section.
- EFUNS: Calculate the ratio of the K-shell electron-impact ionization cross section (σ_{EII}) to the Møller-scattering cross section σ_M (σ_{EII}/σ_M).
- MAIN: Piecewise Linear Fit(PWLF) the ratio (σ_{EII}/σ_M) together with other electron cross sections and branching ratios.
- LAY: Output the PWLF result of the ratio (σ_{EII}/σ_M).

The following subroutines and functions of EGS4 were modified in order to implement the electron-impact ionization:

- HATCH: Read in the ratio (σ_{EII}/σ_M).
- EDGSET: Pass PHOTK to MOLLER. PHOTK is the ratio of the K-shell photoeffect cross section to the total photoeffect cross section.

- MOLLER: Sample the electron-impact ionization using the ratio (σ_{EII}/σ_M). Then, determine the K-X ray emission or the Auger-electron emission and sample the K-X ray energy.

- ELECTR: Return to SHOWER after calling of MOLLER if the particle at the top of the STACK is a photon.

In the PEGS4 and EGS4 calculation, the flag variable is used to enable EII, and a default calculation without EII is performed when the flag is turned off. In the PEGS4 calculation, IMPACT=2 enables an EII cross-section preparation; IMPACT=0 or no mention of IMPACT turns off the EII cross-section preparation. In the EGS4 user code, IMPACR(I)=1 speciies the inclusion of EII in region I, and IMPACR(I)=0 specifies the ignorance of EII in region I.

Appendix B. ESIG evaluation in USTEP loop

In a class-II simulation of charged-particle transport, Møller scattering, Bhabha scattering and bremsstrahlung production are treated as separate interactions only when the produced particle energy is beyond some threshold, on the other hand soft collisions are treated as continuous energy loss. In the EGS4 code, the interaction cross section (Σ) is defined as either (Møller scattering cross section + bremsstrahlung cross section) or (Bhabha cross section + bremsstrahlung cross section) for an electron and a positron, respectively. One problem concerning this treatment is that the interaction cross section is energy dependent, and the electron and positron energy changes continuously. EGS4 has a correction capability for this problem. This correction is effective when the interaction cross section is an increasing function of the energy, but is not effective when the interaction cross section is a decreasing function of the energy. For example, the interaction cross section of Sn has its minimum value at around 5 MeV. Thus, the interaction cross section of Sn is not adequately evaluated below 5 MeV. This causes an underestimation of both the Møller scattering and bremsstrahlung. Also, this causes an underestimation of the electron-impact ionization, since the electron-impact ionization is sampled using the ratio of the electron-impact ionization to the Møller scattering in this study.

Two groups of the authors developed the methods to solve the underestimation of the Møller scattering and the bremsstrahlung. Ma and Nahum intensively studied the effect of this problem using their own algorithm [20]. Aarnio et al used maximum interaction cross section to determine interaction point in FLUKA [21].

In this study, Ma and Nahum's method is applied for this correction after including two modifications. The starting points for this correction is: "If there are *N(E)*-particles

of energy E, the number of discrete event is $\Sigma(E)N(E)$". Here, $\Sigma(E)$ represents discrete event cross section. This is described in a differential equation:

$$\frac{dN}{dE} = -\Sigma(E)N(E). \tag{5}$$

For an analytical calculation, Eq.(5) is solved as:

$$N(E) = N_0 \exp\left(-\int_E^{E_0} \Sigma(E')dE'\right) = N_0 \exp\left(-\int_x^{x_0} \frac{\Sigma(E(x'))}{dE/dX(E(x'))}dx'\right) \tag{6}$$

Here, N_0 is the number of electrons when their energy is E_0.

In order to carry out an actual Monte-Carlo calculation, Eq(5) is rewritten as:

$$\frac{dN}{dE} = -\left(\frac{\Sigma(E)}{f\Sigma_0}\right) f\Sigma_0 N(E). \tag{7}$$

Here f is a Ma and Nahum's factor to make $(\Sigma(E)/f\Sigma_0) < 1$. And Σ_0 is an arbitary constant at this stage. The place of discrete event is sampled by:

1. Particle travels ($f\Sigma_0$DEMFP). DEMFP is calculated by $(-\log\xi)$. ξ is a random number between 0 and 1. Σ_0 is a descrete event cross section at the beginning of each USTEP.

2. When a descrete event occurs, another random number $\xi_2(0 < \xi_2 < 1)$ is used to reject that event if $(\Sigma(E)/f\Sigma_0) < \xi_2$.

The modified points are:

- The evaluation of Σ_0 is moved into the USTEP-loop.
- $\Sigma(E)$ is used as discrete event cross section when partice energy is E. This is the same way as the original EGS4 code does.

The following macro is used in the calculation to implement the modification described in this appendix.

```
REPLACE{;SIG=SIG0*RHOF;} WITH
{;IF(EKE.LE.3.*TE(MEDIUM))[FMFPCM=1.;]
ELSE[FMFPCM=1.+(EKE-3.*TE(MEDIUM))/(10.*TE(MEDIUM)+EKE*EKE);]
IF(LELEC.LT.0) [$EVALUATE SIG0 USING ESIG(ELKE);]
ELSE ["E+"$EVALUATE SIG0 USING PSIG(ELKE);]
SIG=SIG0*RHOF*FMFPCM;}

REPLACE {;]UNTIL (RFICT.LE.SIGF/SIG0);} WITH
{;]UNTIL (RFICT.LE.SIGF/(FMFPCM*SIG0));}
```

In Fig.1, the difference of dashed line and dotted line indicates the effect of a correction of an underestimation of the bremsstrahlung.

References

[1] W. R. Nelson, H. Hirayama, and D. W. O. Rogers, *The EGS4 code system*, SLAC-265 (Stanford University, Stanford, 1985).

[2] Y. Namito, W. R. Nelson, S. M. Seltzer, A. F. Bielajew and D. W. O. Rogers, *Low-energy x-ray production studies using EGS4 code system*, Med. Phys. **17**, 557 (1990)(abstract).

[3] H. Hirayama and Y. Namito, *A benchmark calculation using EGS4 code - Bremsstrahlung photon production by thick target irradiated by electrons with energy less than a few MeV-*, Japan Atomic Energy Society Fall Meeting D29, Sapporo (Sep. 1994)(abstract).

[4] C. J. Powell, *Cross sections for ionization of inner-shell electrons by electrons*, Rev. of Mod. Phys. **48**, 33-47 (1976).

[5] J. Deiwiks et al, *Energy loss of slow positrons in foils*, Proceedings of the 10th international conference on positron annihilation, Materials Science Forum **175-178**, 951-954 (1995).

[6] M. Gryziński, *Two-particle collisions. I. General relations for collisions in the Laboratory system*, Phys. Rev. **138**, A305-A321, (1965).

[7] M. Gryziński, *Two-Particle Collisions. II. Coulomb Collisions in the Laboratory System Coordinates*, Phys. Rev. **138**, A322-A335 (1965).

[8] M. Gryziński, *Classical Theory of Atomic Collisions. I. Theory of Inelastic Collisions*, Phys. Rev. **138**, A336-A358 (1965).

[9] H. Kolbenstvedt, *Simple theory for K-ionization by relativistic electrons*, J. of Appl. Phys. **38**, 4785-4787 (1967).

[10] S. Seltzer, *Cross sections for the bremsstrahlung production and electron-impact ionization*, in: Monte Carlo transport of Electron and Photons, eds. T. M. Jenkins, W. R. Nelson and A. Rindi, (Plenum, New York, 1988) page 103-109.

[11] H. M. Colbert, *SANDYL A computer program for calculating combined photon-electron transport in complex systems*, Sandia National Laboratory, SLL-74-0012 (1974).

[12] M. J. Berger and S. M. Seltzer, *ETRAN Monte Carlo code system for electron and photon transport through extended media*, CCC-107, Radiation shielding information center, Computer code collection, Oak Ridge National Laboratory, June (1968).

[13] S. M. Seltzer, *An overview of ETRAN Monte Carlo methods*, in: "Monte Carlo transport of Electron and Photons", eds. T. M. Jenkins, W. R. Nelson and A. Rindi, (Plenum, New York, 1988) page 153-181.

[14] H. Hirayama and D. K. Trubey, *Effects of incoherent and coherent scattering on the exposure buildup factors of low-energy gamma rays*, Nucl. Sci. Eng. **99**,145-156 (1988).

[15] R. Placious, *Dependence of 50- and 100-keV Bremsstrahlung on Target Thickness, Atomic Number and Geometric Factors*, J. Appl. Phys. **38**, 2030 (1967).

[16] M. J. Berger, *ETRAN-Experimental Benchmarks*, in: "Monte Carlo transport of Electron and Photons", edd. T. M. Jenkins, W. R. Nelson and A. Rindi, (Plenum, New York, 1988) page 216, Figure 8.27b.

[17] A. F. Bielajew and D. W. O. Rogers, *PRESTA: The parameter reduced electron - step transport algorithm for electron Monte Carlo transport*, PIRS No.042 NRCC (July 1986).
A. F. Bielajew and D. W. O. Rogers, *The parameter reduced electron-step transport algorithm for electron Monte Carlo transport*, Nucl. Instrum. and Meth.**B18**, 165-181 (1987).

[18] D. W. O. Rogers, S. Duane, A. F. Bielajew and W. R. Nelson, *Use of ICRU-37/NBS radiative stopping powers in the EGS4 system*, PIRS-0177 NRCC (March 1989).

[19] A. F. Bielajew, R. Mohan and C. Chui, *Improved bremsstrahlung photon angular sampling in the EGS4 code system*, PIRS-0203 NRCC (November 1989).

[20] Chang-ming Ma and A. E. Nahum, *A new algorithm for EGS4 low-energy electron transport to account for the change in discrete interaction cross-section with energy*, Nucl. Instrum. and Meth.**B72**, 319-330 (1992).

[21] P. A. Aarnio, A. Fassò, A. Ferrari, J.-H. Möhring, J. Ranft, P. R. Sala, G. R. Stevenson and J. M. Zazula, *Electron-photon transport: Always so good as we think? Experience with FLUKA*, in: International conference on Monte Carlo simulation in high Energy and Nuclear Physics (MC93), eds. P. Dragovitsch, S. L. Linn and M. Burbank (World Scientific 1993) page 100-110.

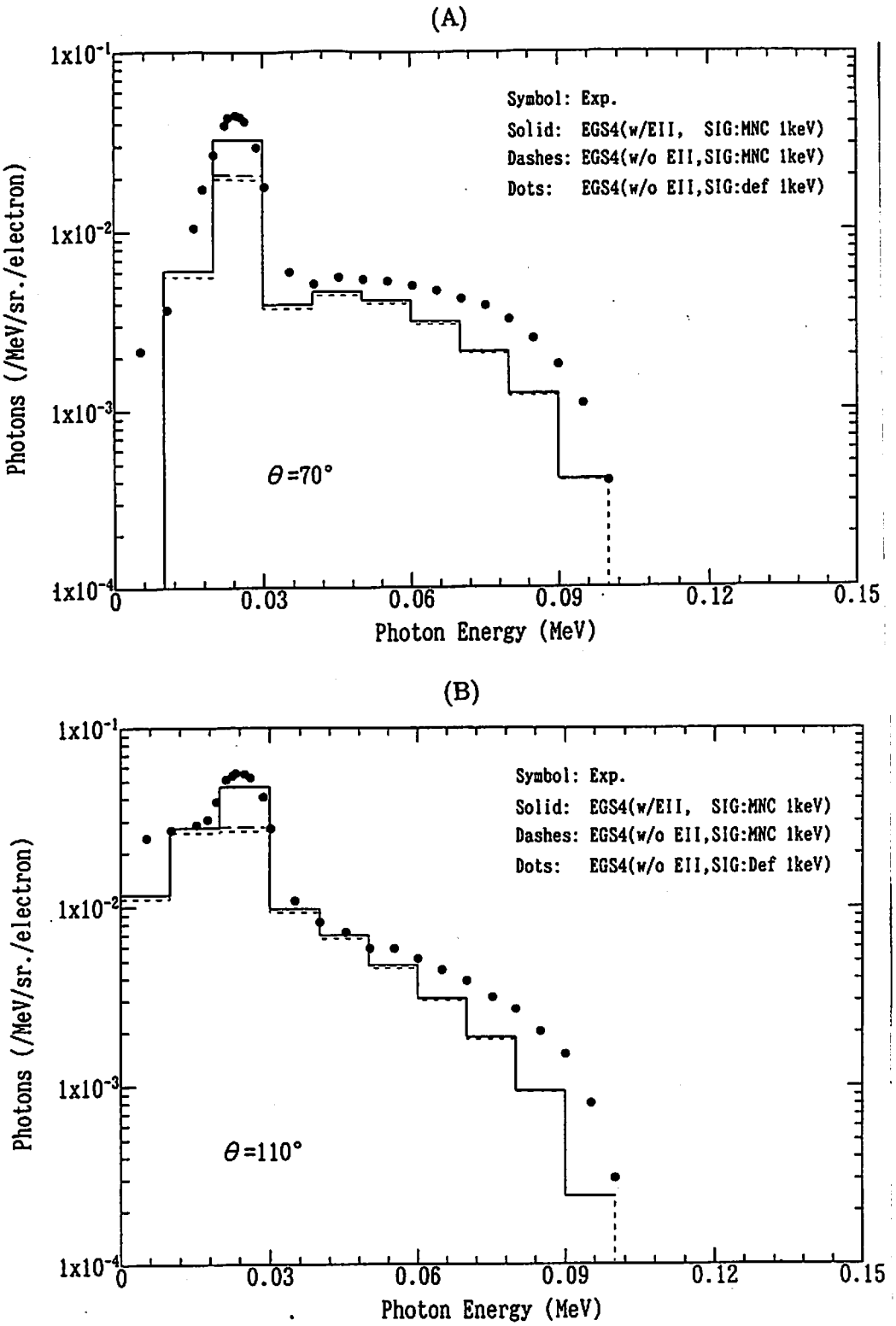

Figure 1: Spectra of the bremsstrahlung and K-X rays from a Sn target (21.6 mg/cm^2). A 100 keV electron beam is normally incident on the target. Photons emitted toward (A) 70° and (B) 110° from the incident electron direction are shown, respectively. The closed circle is a measurement by Placious. The solid and dashes line show the EGS4 calculation with and without electron-impact ionization (Møller scattering and bremsstrahlung underestimation is corrected). The dotted line shows the EGS4 calculation in the condition that electron-impact ionization is not included and the Møller scattering and bremsstrahlung underestimation is not corrected. The dashed line and solid lines overlap many times.

IMPLEMENTATION OF AN L-SHELL PHOTOELECTRON AND AN L X-RAY FOR ELEMENTS INTO THE EGS4 CODE

H. HIRAYAMA, Y. NAMITO and S. BAN

National Laboratory for High Energy Physics
1-1 Oho, Tsukuba-shi, Ibaraki 305 Japan

Abstract

The subroutines PHOTO and EDGSET were modified in order to treat photoelectrons from L photoabsorption and L fluorescence photons in elements. The L_1, L_2 and L_3 shells are treated separately. An L fluorescence photon after K fluorescence is also treated. The flag IEDGFL(IR) is used to produce fluorescence photons or to disable them for each region (IR). When IEDGFL is set to the atomic number of the element at each region, fluorescence photons can be produced after K and L photoabsorption. If IEDGFL is negative and its absolute value is the atomic number of the element, although a photoelectron after the L photoabsorption is produced, a fluorescence photon is treated as energy absorption. In the case that IEDGFL is equal to zero, a photoelectron produced after K only photoabsorption is treated without a fluorescence photon.

1. Introduction

K-edge fluorescence photons in elements can be treated in the EGS4 system using the special version of SUBROUTINE PHOTO described in SLAC-265.[1] In the current SUBROUTINE PHOTO, photoelectrons produced by photons below the K-edge of the material are not transported, and are treated as energy deposition at the interaction point. This causes some difficulties to calculate the detector response, such as TLD for low-energy photons. L-shell fluorescence photons also play an important rule, especially for high-Z materials.

It is necessary to introduce atomic-energy levels related to the L-shell in order to treat photoelectrons and to produce L-shell fluorescence photons below the K-edge. The photoelectric reaction related to L-shell electrons must be treated with each subshell, which is L_1, L_2 or L_3. There are many channels to produce L-shell fluorescence photons

after an L-shell electron vacancy is created by a photoelectric reaction. Moreover, L-shell fluorescence photons can be created after K-shell fluorescence photon production if it is related to the L-shell.

The procedures to treat the above mentioned phenomena in the revised subroutines PHOTO and EDGSET are presented in this report.

2. Data Related to L-shell

2.1 Atomic Energy Levels

The values presented in Table 9 in Appendix III of the Table of Isotopes[2] are used as the atomic energy levels of three L-subshells.

2.2 Total Atomic Level Widths for Each Subshell

The total atomic level widths for each subshell are necessary to determine the subshell which causes photoabsorption. The theoretical atomic-level widths were taken from Figs. 2-4 of Krause.[3]

2.3 Relative Shell Contribution to Photoelectric Cross Section

The relative shell contribution to the photoelectric cross section was taken from Table VIII of Storm and Israel.[4] For elements that are not included in the table, the data can be interpolated supposing that they are proportional to the atomic number (Z). These data were used to determine the shell to which a photoelectron belongs.

2.4 Fluorescence Yields for L Subshells

The fluorescence yields for the L subshells are the probability that a fluorescence photon is emitted after the creation of an L subshell vacancy. These data were taken from Table 3 of Krause[3].

2.5 L X-ray Energies and Their Relative Intensities

There are 51 X-rays related to L-shell vacancies. Among them, major 20 X-rays were selected. Their relative intensities are larger than 1% of L_{α_1} for ^{100}Fm. In Table 1, these X-rays for lead are given together with their energy and relative intensity. The L X-rays energies and their relative intensities are taken from Table IV and VI of Storm and Israel.[4] For elements that are not included in the table, the data are interpolated

supposing that they are proportional with the atomic number (Z).

2.6 Coster-Kronig Yields

In the case that a vacancy is created in the L_1 or L_2 subshell, a Coster-Kronig transition must also be considered. Coster-Kronig is a nonradiative transition like Auger, but create a new hole at the L_2 or L_3 subshell. The Coster-Kronig yields were taken from Table 3 of Krause[3].

3. Change in EDGSET

All of the data related to the L X-rays mentioned in the previous section are included in the form of a DATA statement, just as for the current version EDGSET. Data related to the L-subshells and L X-rays are not given for all elements. If the data for a selected element are not given (=0), they are interpolated supposing that they are proportional to the atomic number, as mentioned in the previous sections.

4. Change in PHOTO

SUBROUTINE PHOTO, which treats K X-rays, was modified so as to include L X-rays, as shown below.

The meanings of the main variables used in the SUBROUTINE PHOTO are given in Table 2. The flag IEDGFL(IR) is used to produce fluorescence photons or disable to them for each region (IR). When IEDGFL is set to the atomic number of the element at each region, fluorescence photons can be produced after K and L photoabsorption. If IEDGFL is negative and its absolute value is the atomic number of the element, although a photoelectron after K and L photoabsorption is produced, the fluorescence photon is treated as energy absorption. In the case that IEDGFL is equal to zero, a photoelectron after only K photoabsorption is treated without a fluorescence photon.

A flow chart of SUBROUTINE PHOTO and the lists of SUBROUTINE EDGSET and PHOTO are given in Fig. 1 of Ref. 5.

5. Comparison with Measurement

Pulse-height distributions of Ge detector for L X-rays from lead by 40 keV photons were calculated by the EGS4 with this implementation and were compared with measured ones to check the revisions mentioned above.

Measurements were performed at a 2.5-GeV synchrotron-light facility (KEK-PF). The experimental arrangement is shown in Fig. 1. Photons from a vertical wiggler were used after being monochronized by a Si(1,1,1) double-crystal monochromator. The incident

beams were 40 keV linialy polarized photons. In Fig. 1 the propagation and polarization vectors of an incident photon are shown as $\vec{k_0}$ and $\vec{e_0}$. Incident photons passed through a collimator (C_0) with an opening diameter (D_0) of 2mm and a free ionization chamber (S). The photon intensity was monitored by the FAIC, which was calibrated by a calorimeter [6].

The lead sample of 0.568 g/cm^2 was set with the normal vector of $(-\frac{1}{2}, -\frac{1}{\sqrt{2}}, \frac{1}{2})$. The effective thickness for incident photons of this sample was more than ten mean free paths. The sample was contained in a vacuum chamber and vacuum pipes were placed between the vacuum chamber and the Ge detectors in order to reduce any scattering due to air.

Photons throurg collimators (C_1 and C_2) located in the X and Y directions were detected by Ge detectors (Ge-1 and Ge-2).

EGS4 calculation was devided to two parts. At first, photons emitted to the Ge detector was calculated. The calculation was performed considering both the linear polarization[7] and Doppler broadening[8] of phtons. Next, pulse-height distributions of a Ge detector were calculated for photons having a spectrum obtained at the previous step with 5.01 mm diameter.

Fig. 2 shows the comparison of the pulse-height distribution of the holizontal Ge detector (Ge-1) in absolute values. It is clear that L X-rays obtained from the EGS4 calculation agree very well with the measured ones both in their energy and intensities.

It can be concluded that the implementation of L X-rays is done correctly from the comparisons above. This inplementation will be very useful for the study of low-energy photons together with the our previous improvements concerning the linear polarization and Doppler broadening.

References

[1] W. R. Nelson, H. Hirayama, and D .W .O Rogers, *EGS4 code system*, **SLAC-265**, (1985).

[2] C. M. Lederer and V. S. Shirley,*Table of Isotopes, Seventh Edition*, A Wiley-Interscience Publication (1978).

[3] M. O. Krause,*Atomic Radiative and Radiationless Yeields for K and L Shells*, J. Phys. Chem. Ref. Data, **8** 307(1979).

[4] E. Storm and H. I. Israel,*Photon Cross Sections from 1 keV to 100 MeV for Elements Z=1 to Z=100*, Atomic Data and Nucl. Data Tables, **7** 565(1979).

[5] H. Hirayama, Y. Namito and S. Ban,*Implementation of an L-Shell Photoelectron and an L X-ray for Elements into the EGS4 Code*, **KEK Internal 96-10**, (1996).

[6] Y. namito, S. Ban and H. Hirayama, Nucl. Instrum. Methods Phys. Res. Sect. A **332**, 277(1993).

[7] Y. namito, S. Ban and H. Hirayama, Nucl. Instrum. Methods Phys. Res. Sect. A **349**, 489(1994).

Table 1. L X-ray Energy and Relative Intensity to L_{α_1} for lead[4]

L X-ray	Energy(keV)	Intensity(%)
L_1-M_2=β_4	12.307	31.6
L_1-M_3=β_3	12.795	34.6
L_1-M_9=β_{10}	13.275	1.15
L_1-M_5=$\beta_{9/1}$	13.377	1.71
L_1-N_2=γ_2	15.097	8.13
L_1-N_3=γ_3	15.218	9.67
L_1-O_2=$\gamma_{4/1}$	15.757	1.59
L_1-O_3=$\gamma_{4/2}$	15.775	1.86
L_2-M_1=η	11.349	3.56
L_2-M_4=β_1	12.614	130.
L_2-N_1=γ_5	14.309	.917
L_2-N_4=γ_1	14.765	26.7
L_2-O_4=γ_6	15.180	3.26
L_3-M_1=l	9.184	5.91
L_3-M_4=α_2	10.449	11.4
L_3-M_5=α_1	10.551	100.
L_3-N_1=β_6	12.144	1.45
L_3-N_4=β_{15}	12.600	2.14
L_3-N_5=β_2	12.622	31.6
L_3-$O_{4,5}$=β_5	13.016	2.57

Table 2. Meaning of main variables used in SUBROUTINE PHOTO

Name of variable	Meaning
IEDGFL	atomic number of the material at each region >0:fluorescence photon is produced after K or L photoeffect 0:K photoelectron only is treated without fluorescence photon <0, ABS(IEDGFL) is atomic number of the material at each region :K and L photoelectrons are treated without fluorescence photon
EKAL1	energy of K α_1
EKAL2	energy of K α_2
EKBE1	energy of K β_1
EKBE2	energy of K β_2
BKR1	$(\sigma_K/\sigma_{photo.}) \cdot \omega_K$
BKR2	BKR1$\times\sigma_{K_{\alpha_1}}/\sigma_K$
BKR3	BKR1$\times(\sigma_{K_{\alpha_1}} + \sigma_{K_{\alpha_2}})/\sigma_K$
BKR4	BKR1$\times(\sigma_{K_{\alpha_1}} + \sigma_{K_{\alpha_2}} + \sigma_{K_{\beta_1}})/\sigma_K$
BKPHOT	probability of K absorption
EDGL1	atomic energy level of L_1 subshell
EDGL2	atomic energy level of L_2 subshell
EDGL3	atomic energy level of L_3 subshell
PWL1	probability of L_3 or L_2 photoabsorption above L_1 edge
PWL2	probability of L_3 photoabsorption between L_1 and L_2 edge
XLY1	coresponding to BKR1 to BKR4 for L_1 photoabsorption
XLY2	coresponding to BKR1 to BKR4 for L_2 photoabsorption
XLY3	coresponding to BKR1 to BKR4 for L_3 photoabsorption
ELX1	L X-ray energy related L_1 subshell
ELX2	L X-ray energy related L_2 subshell
ELX3	L X-ray energy related L_3 subshell
BL1	branching ratio related L_1 subshell
BL2	branching ratio related L_2 subshell
BL3	branching ratio related L_3 subshell

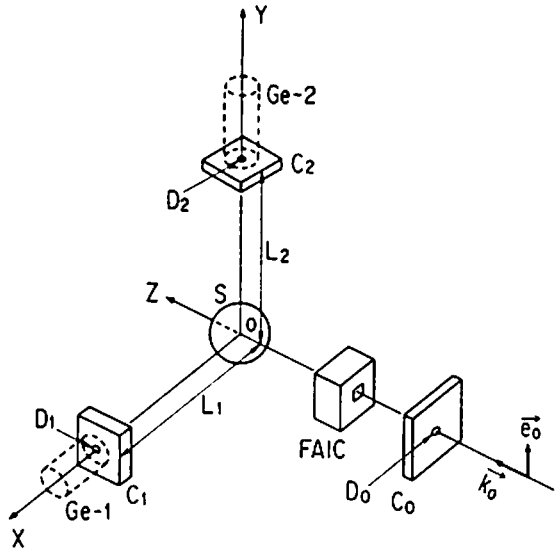

Fig. 1. Experimental arrangement. The incident photon beam passed through collimator (C_0) with an opening diameter (D_0) of 2 mm and a tree air ionization chamber (FAIC), and scattered bu a sample (S) located at point O. The normal vector of the sample was $(-\frac{1}{2}, -\frac{1}{\sqrt{2}}, \frac{1}{2})$. Photons passing through collimators in the X and Y direction (C_1 and C_2) were detected by Ge detectors (Ge-1 and Ge-2, respectively). The distances from the surface of the sample to the exit of the collimator (L_1 and L_2) were 424 and 436 mm and opening diameter of the collimators (D_1 and D_2) were 5.01 and 5.04 mm.

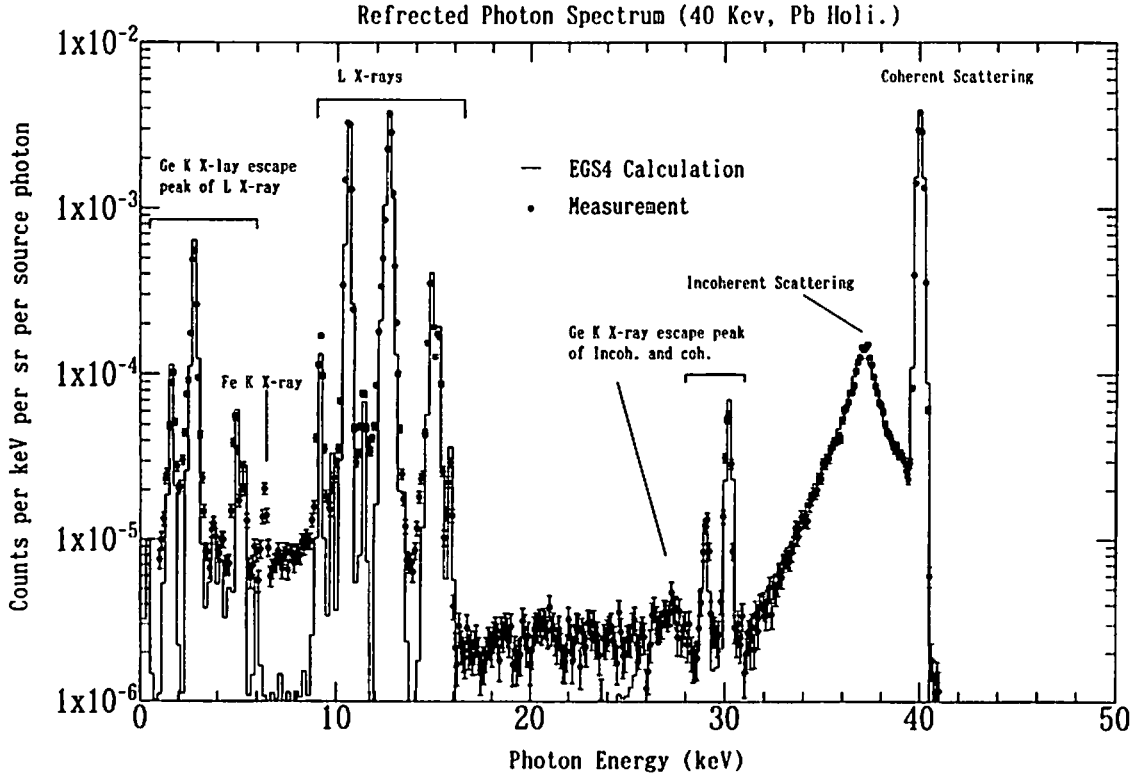

Fig. 2 Pulse-height distribution of scattered-photon from Pb sample (k_0=40 keV). EGS4 calculations are with polarization, incoherent scattering, Doppler Broadening and L X-rays.

CALCULATION USING MCNP CODE FOR BREMSSTRAHLUNG PHOTONS EMITTED FROM RADIOISOTOPE BATTERY

A. OHASHI, K. UEKI and T. SENDA

Ship Research Institute, MOT
6-38-1, Shinkawa, Mitaka, Tokyo 181, Japan

1. Introduction

A radioisotope battery is one of the choice for energy source of meteorological observation and development of undersea and space[1]. We considered a Strontium-90 (β-decay, half-life: 28.8y) heat-source model of a radioisotope battery and improved it in two aspects-radiation dose reduction and improvement of thermal conductivity-adding functionally graded structure to the model. The present study reports the dose reduction on the surface of the heat source model and the analysis of Naumann and Waechter's experiment[2] using a continuous energy Monte Carlo calculation code, MCNP 4A[3].

2. Model and Analysis

Figure 1 shows the two models which were calculated. The base structure was considered with another research group for improvement of heat transfer characteristics, while three layered structure was adopted on the view point of shielding. The base structure

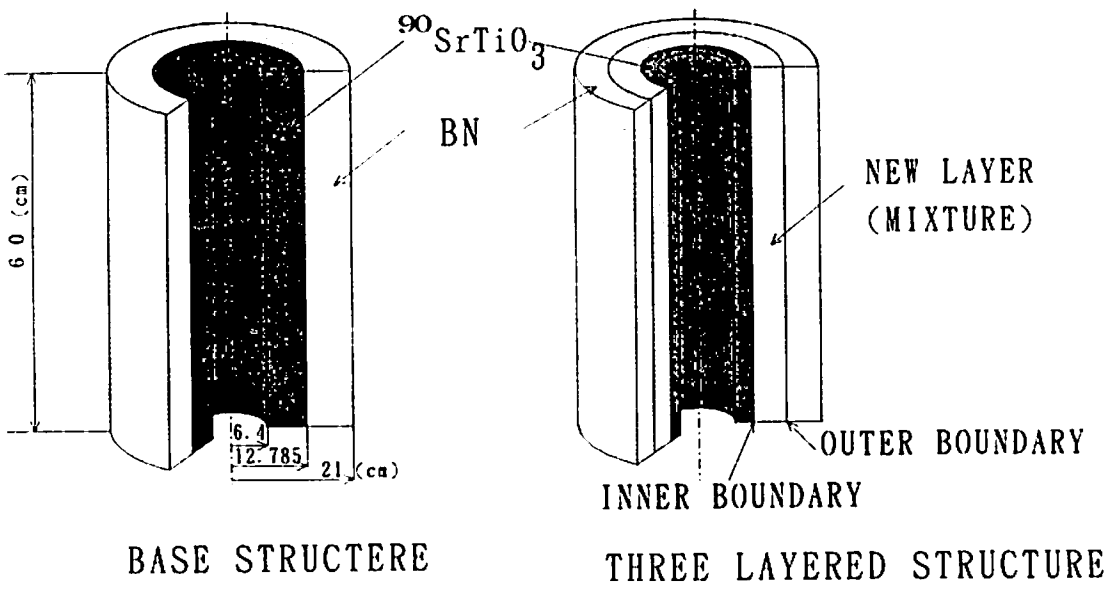

Figure 1. Calculation model.

was assumed to be a concentric cylinder of 60 cm height which formed void, strontium titanate ($^{90}SrTiO_3$, ρ : $5.12g/cm^3$) and boron nitride (BN, ρ : $2.26g/cm^3$) from the inside. The weight of these two materials was made to be identical each other. If a new layer (mixed layer) between $^{90}SrTiO_3$ and BN is added to the base structure conserving each total weight of the two materials, the number of production of bremsstrahlung photons can be reduced because of the drop of average atomic number in the new layer, and also the spectrum of the mixed layer become softer than that of the $^{90}SrTiO_3$ layer. These are factors for radiation dose reduction. On the other hand, there is another factor for radiation dose increase since generated position of bremsstrahlung photons goes outer. Consequently, radiation dose on the surface of the heat source can be minimized by arranging those two factors.

In the present paper, the inner and outer radiuses of mixed layer were changed by 0.5 cm step to simulate the effect of dose reduction. The density of mixture was calculated theoretically from the inner and outer radiuses. Although Strontium has many isotopes, we treated Strontium-90 only. From this condition the model included 2.9E+19 Bq of Strontium-90 at the outset and its thermal output became 52 kW.

3. Condition for Monte Carlo Simulation

Averaged absorbed dose on the cylindrical side of the model in Figure 1 was calculated by means of surface crossing estimator in MCNP 4A. The response function for the absorbed dose was quoted from Ref. 4. Cell importance for electron and weight window for photon were used for variance reduction. To generate more high-energy photon tracks in the bremsstrahlung process, BBREM card was adopted also.

Figure 2 shows normalized spectrum for calculation as a function of 0.15 MeV step. This spectrum was compounded from those of Strontium-90 and Yttrium-90 which were cited from Ref. 5. Source bias was employed to produce more high-energy source electron.

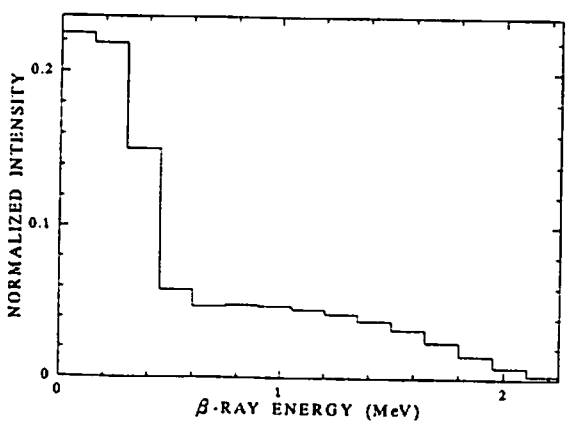

Figure 2. β-ray spectrum for calculation

The effects of cutoff energy for electron were tested to the calculated results and figure of merit, since it take much time for the calculation including electron transportation. These calculations were performed by use of the geometry of the base structure. Figures 3 and 4 show dependence of results of calculation and figure of merit to cutoff energy for electron. From Figure 3 the results decreases with increasing the cutoff energy because cutoff energy kills electrons which can still generate bremsstrahlung photons. On the contrary, the figure of merit rises in keeping with the cutoff energy in Figure 4. From these data we adopted 0.2 MeV for the cutoff energy because it is no effect to the result and possible to save time.

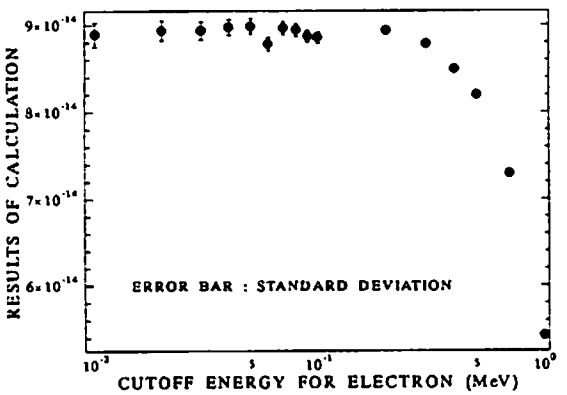

Figure 3. Dependence of results of calculation to cutoff energy for electron.

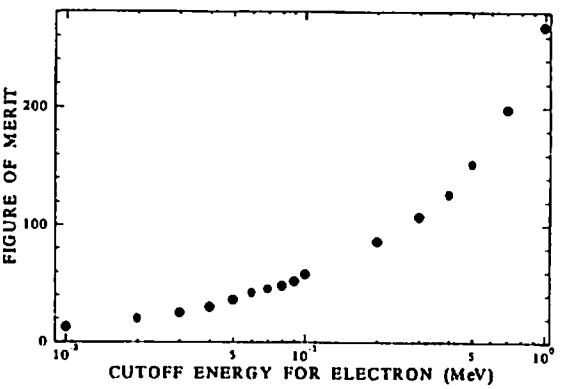

Figure 4. Dependence of figure of merit to cutoff energy for electron.

Many calculations are required to derive the minimized absorbed dose and its inner and outer radiuses in the three layered structure. Hence it still takes much time for the calculations in our computer environment. For this reason, simplified calculations were performed to search for the tendency of the dose variation to the radiuses, which were set to 2.245 MeV as monoenergy electron source and 2.24 MeV as cutoff energy for electron. In this calculation MCNP 4A kills source electron within one substep and generates bremsstrahlung photons by thick target bremsstrahlung approximation. The simplified calculations were performed changing the inner and outer radiuses in the condition of 0.5 cm step to derive the tendency of the dose variation. We selected some sets of the inner and outer radiuses whose results showed the value within one standard deviation from the minimum value of simplified calculation. These selections were recalculated by normal calculations with the 0.2 MeV cutoff energy to obtain the minimized absorbed dose.

Workstations of Hewlett Packard Company (9000/735,755) were used for calculations. It took one hour for simplified calculation with 15 million source electrons and five hours

for normal calculation with three million source electrons.

4. Results and Consideration for Three Layered Structure

Figure 5 shows the results of simplified calculation. The horizontal axis indicates the inner radius of mixed layer for the three layered structure. Eight graphs correspond to the radius of the outer boundary in the figure. Each vertical line of the graphs reveals relative intensity of absorbed dose in linear scale and gives the same range each other. Error bar expresses standard deviation from the Monte Carlo simulation. The results of each graph show the lower values in the range from 11.5 to 12 cm of the inner radius. In regard of the outer radius, the lower absorbed doses are observed between 15.5 and 18.0 cm of the radius. It is considered that the minimum absorbed dose locates within these range.

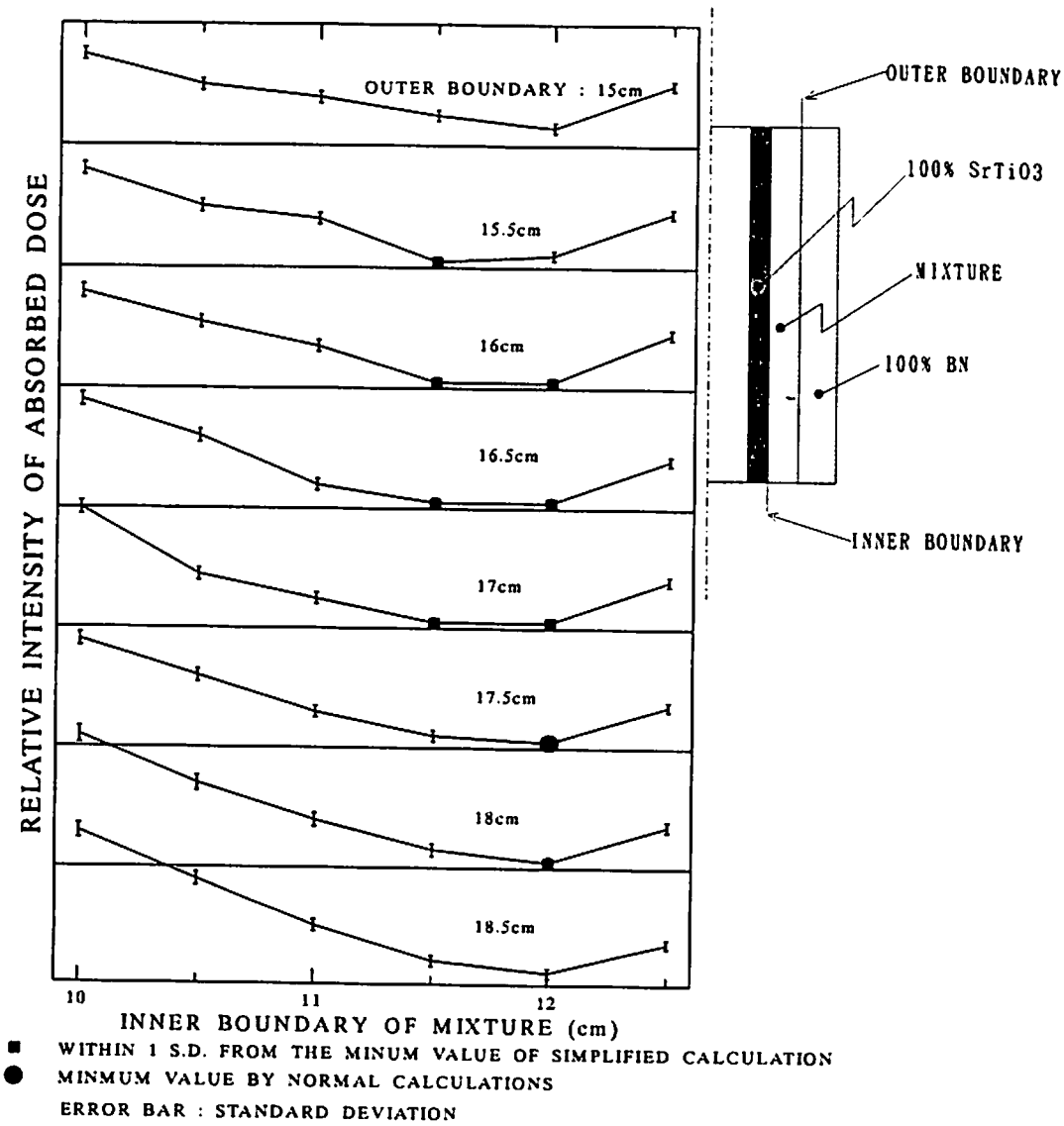

Figure 5. Results of simplified calculation.

In this figure, filled square indicates the results which show the values within one standard deviation from the minimum value of the simplified calculations. These geometry was recalculated by normal calculations with the 0.2 MeV cutoff energy. The minimum value of the normal calculation was shown in it by filled circle (inner radius: 12.0 cm, outer radius: 17.5 cm). The ratio of the value to that of the base structure was 83 $\pm$ 1 %. Since the radiuses of mixed layers were changed by 0.5 cm step, it is possible that the ratio would become lower if the step became smaller. But it is very difficult to show the difference between the minimum value and the new result because of the precision of the results.

5. Simulation for Naumann and Wacher's Experiment

Naumann and Waecher determined the attenuation curve in lead for bremsstrahlung photons from $^{90}Sr + ^{90}Y$. Figure 6 shows the diagram of Naumann and Waecher 's experiment. They measured ionization current of bremsstrahlung photons which penetrate lead shield. Using these data, we tested the reliability of our calculation.

The benchmark calculation was performed with the same variance reduction technique and source spectrum as those of the calculation for radioisotope battery. In addition to that, exponential transform was adopted in lead shield. To decide cutoff energy, we tested the variation of the calculated exposure on the surface of Aluminum plate in Figure 6 to cutoff energy. From the result, the cutoff energy was set to 0.09 MeV.

Coupled calculation method in MCNP 4A was used with SSR and SSW cards. This method can divide a calculation to two using a surface source. In this calculation surface source was dumped by use of SSR card first, whose particle crossed on the plain including the detector side of aluminum plate in Figure 6 without shield. With lead shield this surface source was read by SSW card in subsequent calculation to obtain the attenuation curve. Hence it is possible to save much time because only backscattered particles from the lead shield are computed in the source side from the surface source for the subsequent calculation.

Energy deposition in ionization chamber was calculated for each shield thickness. It took two days in all with 13 million source electrons using Hewlett Packard Company's workstation, 9000/755.

The calculated results were shown in Figure 7 with the measured values. The agreement of the data was very good except 4 cm lead thickness.

6. Coclusion

The possibility of absorbed dose reduction for the heat source of a ^{90}Sr radioisotope battery was studied by adding functionally graded structure to the heat source using a

continuous energy Monte Carlo code MCNP 4A. When a mixed layer was made from 12.0 cm to 17.5 cm between the layer of $SrTiO_3$ and BN of the heat source, absorbed dose showed minimum value and 17 % reduction to the dose of base structure.

Naumann and Waecher's experiment was simulated by means of MCNP 4A code. The calculated values showed good agreement with the measured values. Hence we can make sure of the reliability of our calculation.

In the future, the calculation for more multi-layerd and more realistic model should be gone ahead. After that the model have to be integrated with the results of improvement of thermal conductivity.

References

[1] N. ITO et al., *Development of Radioisotope Thermoelectric Generator System*, MITSUBISHI JUKO GIHO, **29**, 531-536(1992), in Japanese.

[2] H. H. Naumann and K. H. Waechter, *Shielding for Radioisotope Bremsstrahlung Source Sr^{90} + Y^{90}*, Int. J. Appl. Radiat. Isotopes, **16**, 613-615(1965).

[3] J. F. Briesmeister, Ed., *MCNP-A General Monte Carlo N-Particle Transport Code, Version 4A*, LA-12625(1993).

[4] ICRP Publication 21, Pergamon Press, 1971.

[5] Allen B. Brodsky, Ed., *CRC handbook of radiation measurement and protection*, CRC Press, 1978.

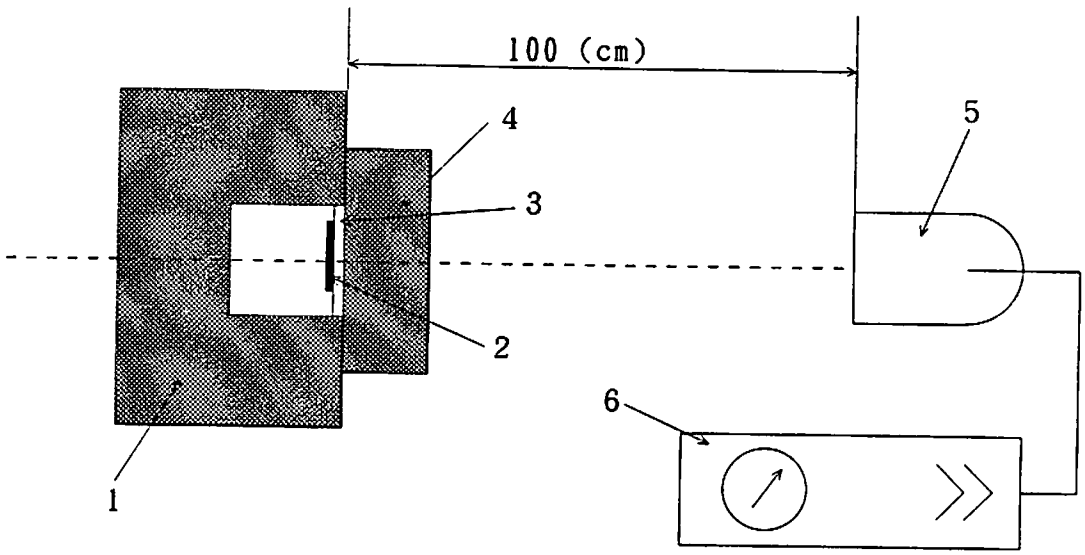

Figure 6. Diagram of Naumann and Waechter's experiment.
1. Lead block of wall thickness 15 cm with 5 cm x 5 cm;
2. ^{90}Sr-^{90}Y source, diameter 22 mm; 3. Al plate 3 mm thick;
4. Lead absorber; 5. Ionization chamber; 6. Vibrating condenser electrometer.

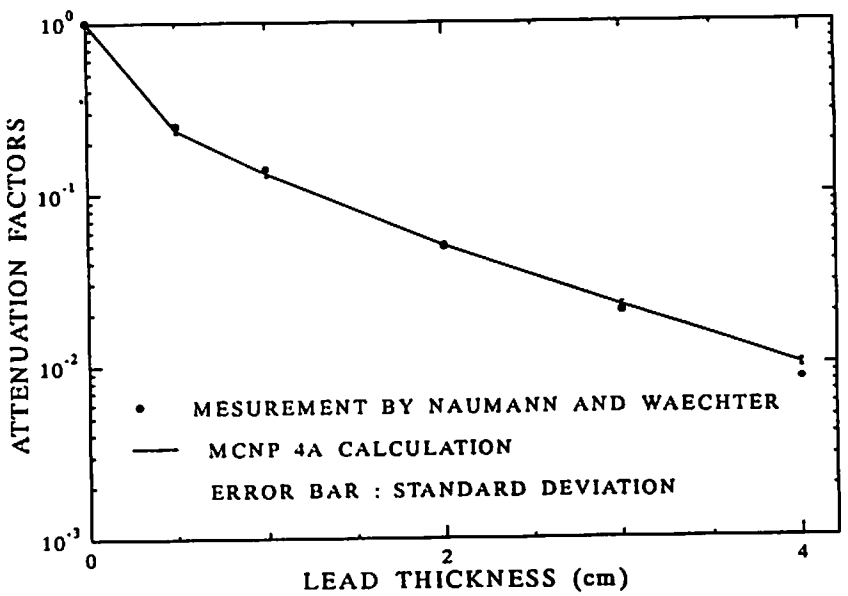

Figure 7. Comparison of the attenuation factors measured by Naumann and Waechter with MCNP 4A calculation.

ON THE BEHAVIOUR OF SECONDARY ELECTRONS FROM MATERIALS OF VARIOUS ATOMIC NUMBERS

J. TADA

Tsukuba University
1-1-1 Tennodai, Tsukuba-shi, Ibaraki, 305 Japan

H. HIRAYAMA

National Laboratory for High Energy Physics (KEK)
1-1 Oho, Tsukuba-shi, Ibaraki, 305 Japan

1. Introduction

Absorbed dose is the most fundamental dosimetric quantity in the current system of radiation dosimetry. As the quantity is defined as spatial density of mean energy imparted to a small volume of the matter, its value is extremely influenced by the distribution of the matter around the point of interest. It is not easy to understand the property of the absorbed dose of X- and gamma rays near the boundary of matters where charged particle equilibrium does not hold, since almost all of the energy imparted are brought by the Coulomb interaction between charged particles in the volume. In this respect, it is important to know the behaviour of the secondary electrons in the vicinity of the interface of materials.

In this paper, results of a numerical analysis of the behaviour of the forward scattered secondary electron (FSSE) from materials with various atomic numbers are discussed. Concerning to this problem, Hine[1] reported experimental results as shown in the Fig.1. His experiment is to observe the changes (increase) of the response of an ionization chamber irradiated with gamma rays by putting a thin foil of various materials in front of it. The chamber wall was made of aluminium of 0.0064 mm thick (which is approximately equal to the CSDA range of 25 keV electron), and the thicknesses of the foils were chosen approximately equivalent to the range of secondary electrons (according to his expression). As seen in the figure, it is reported that the yield of FSSE become minimum at materials of medium atomic numbers.

Hine interpreted the reason by the difference of dominant process which produces sec-

ondary electrons. However, his experiment is not sufficient to clarify the behaviour of FSSE in the following contents: First, photon sources employed in the experiment are not mono-energetic (Table 1). As a result, it becomes difficult to analyze the energy dependence of the phenomena quantitatively. Second, the observation inevitably influenced by the attenuation of the secondary electron in the air gap between the foil and the chamber wall, and in the chamber wall itself. Third, the observation also influenced by the characteristic X-rays produced in the foil. Fourth, influence of the thickness of the foils is not evaluated in the experiment.

It is not easy to resolve these problems experimentally. However, it is possible to avoid these difficulties with a sophisticated numerical simulation, since it enables us to analyze the dependence of the phenomena on each parameters directly. We employed the well established Monte Carlo simulation code EGS4 here.

2. Calculation

In order to simulate the situation that plane parallel beam of photons incidents normally on the surface of the foil, combination of the finite slab geometry of 20 cm radius and the pencil beam of mono-energetic photons are employed (Fig.2). As is well known, quantities summed throughout the surface of downstream side of the slab in this geometry correspond to those at a point on the surface in the case of parallel beam.

The cut off energy of both electrons and photons are set 0.01 MeV, thus electrons and photons having energies less than 0.01 MeV are considered to be absorbed at the position where they are generated. In order to take into account photoelectrons from L-shell and L X-rays, an optional sub-program of EGS-4 developed in KEK is employed[2]. "PRESTA" option is also employed to modify spatial step size near the interface of slabs.

The number of histories of each simulation is ten million which is divided into fifty batches. Fourteen kinds of materials, i.e., carbon, sodium, aluminium, titanium, iron, copper, germanium, molybdenum, tin, gadolinium, tungsten, platinum, lead and uranium are used for the simulation.

As seen in the Figs.3 and 4 foil thickness of approximately four times of the CSDA range of Compton electron of maximum energy (in sodium; RComp, Max $\sim$0.02 cm for photons of 300 keV, while RK-el. $\sim$0.05 cm) is necessary to saturate the yield of FSSE in the light materials, while foil thickness of approximately equal to the CSDA range of Compton electron of maximum energy (in germanium; RComp, Max $\sim$ 0.01cm for photons of 300 keV, while RK-el. $\sim$ 0.025cm) is necessary for medium and heavy materials.

3. Results and Discussions

The atomic number- and photon energy dependence of the yield of FSSE is shown in

Fig.5. in the figure, the ordinate is the ratio of the energy fluence of FSSE to that of incident photons. As seen in the figure, the atomic number giving minimum yield of FSSE depends on the photon energy.

Contributions of Compton electron and photoelectron to the yield of FSSE is shown in Fig.6. This result ascertains the interpretation given by Hine.

At material of low atomic numbers, the dominant process to generate FSSE is Compton scattering whose cross section is proportional to the atomic number of material. As the cross section of secondary electron attenuation, i.e., that of multiple coulomb scattering of electrons by atomic nuclei is approximately proportional to the second power of the atomic number, the yield of the FSSE decreases with the atomic number for materials of low atomic numbers.

On the other hand, the dominant process of secondary electron production at materials of high atomic numbers is the photoelectric effect whose cross section is proportional to fourth or fifth power of the atomic number. Thus, production of secondary electrons exceeds their attenuation, and the yield of the FSSE increases rapidly with the atomic number at materials of high atomic numbers.

4. Summary

The results of the numerical analysis almost agrees with the conclusions of Hine based on his experimental results. However our analysis shows that the material giving minimum yield of FSSE is not always "that of medium atomic numbers" but is strongly dependent on photon energy. Moreover, the yield of FSSE is sensitive to the thickness of the foil, and the experimental condition of the thickness of foils "approximately equivalent to the range of secondary electrons" may be insufficient for the materials of low atomic numbers.

References

[1] G. J. Hine, Phys. Rev., **82**, 755-756 (1951).

[2] H. Hirayama, Y. Namito and S. Ban, KEK Internal 96-10 (1996).

TABLE 1 Gamma rays sources used in the experiment of Hine

Isotope	Energy and yield of gamma rays (in MeV and %)
^{24}Na	1.369 (100), 2.745 (100)
^{60}Co	1.173 (100), 1.333 (100)
^{65}Zn	1.116 (51), 0.008 (34: K X-rays of Cu)
^{134}Cs	0.605 (98), 0.796 (85), 0.569 (15)
^{61}Cu	0.511 (120), 0.283 (13), 0.589 (13), 0.656 (10)
^{198}Au	0.412 (96)

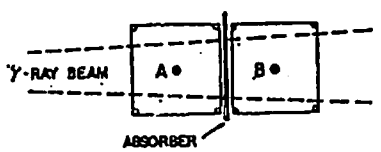

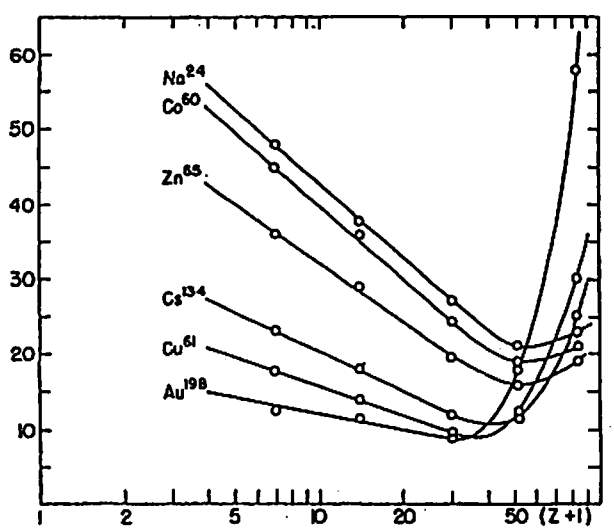

Fig.1 The experimental results reported by Hine[1].

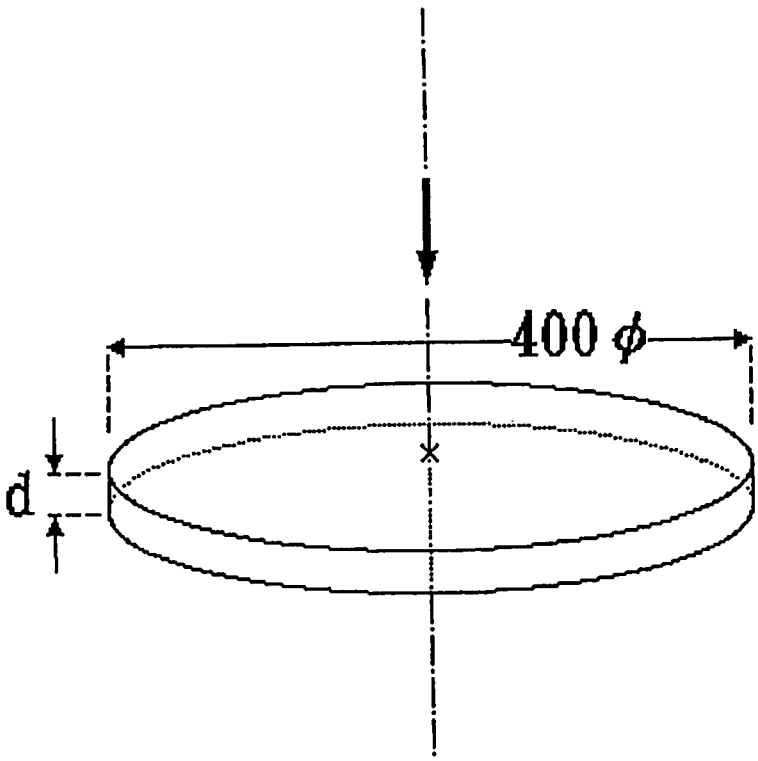

Fig.2 Geometry of the numerical analysis.

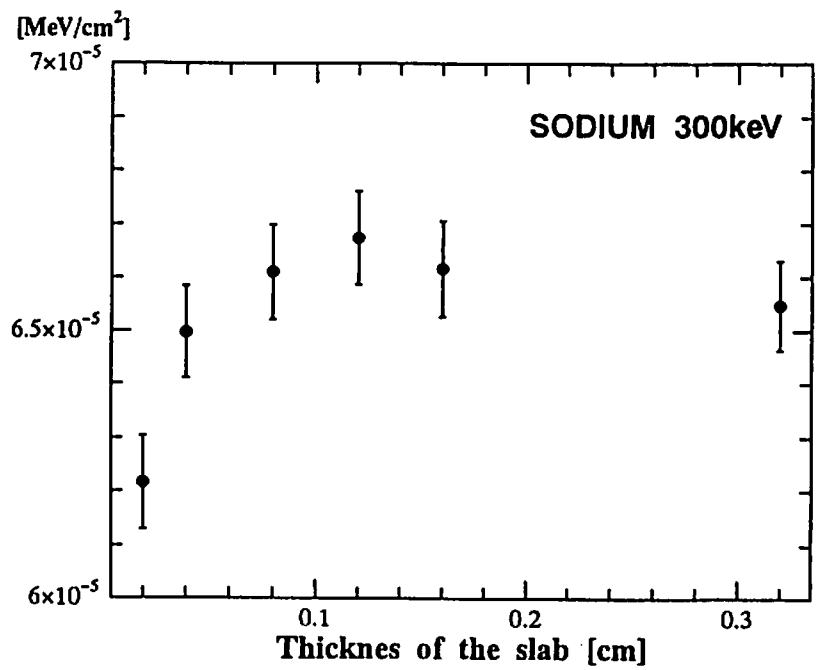

Fig.3 Slab thickness dependence of energy fluence of forward scattering secondary electrons from Sodium

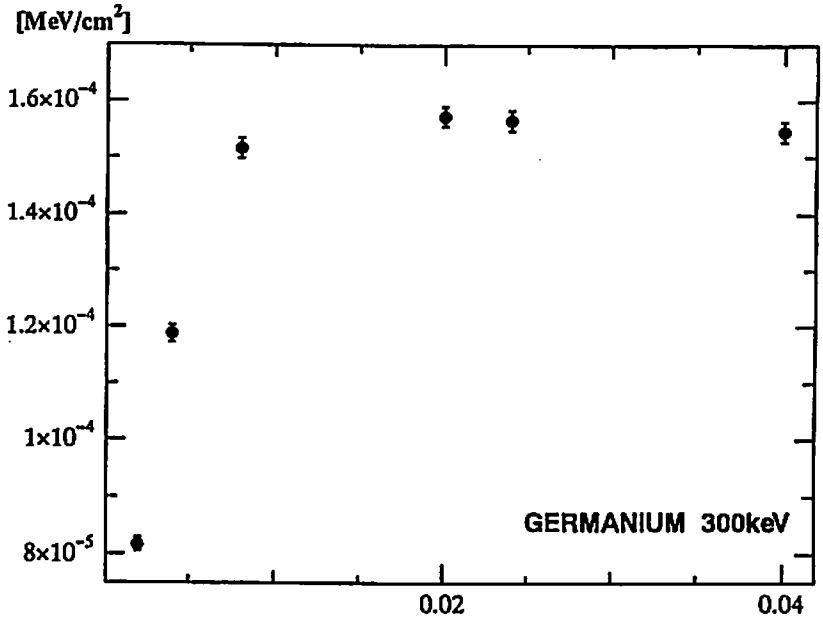

Fig.4 Slab thickness dependence of energy fluence of forward scattering secondary electrons from Germanium

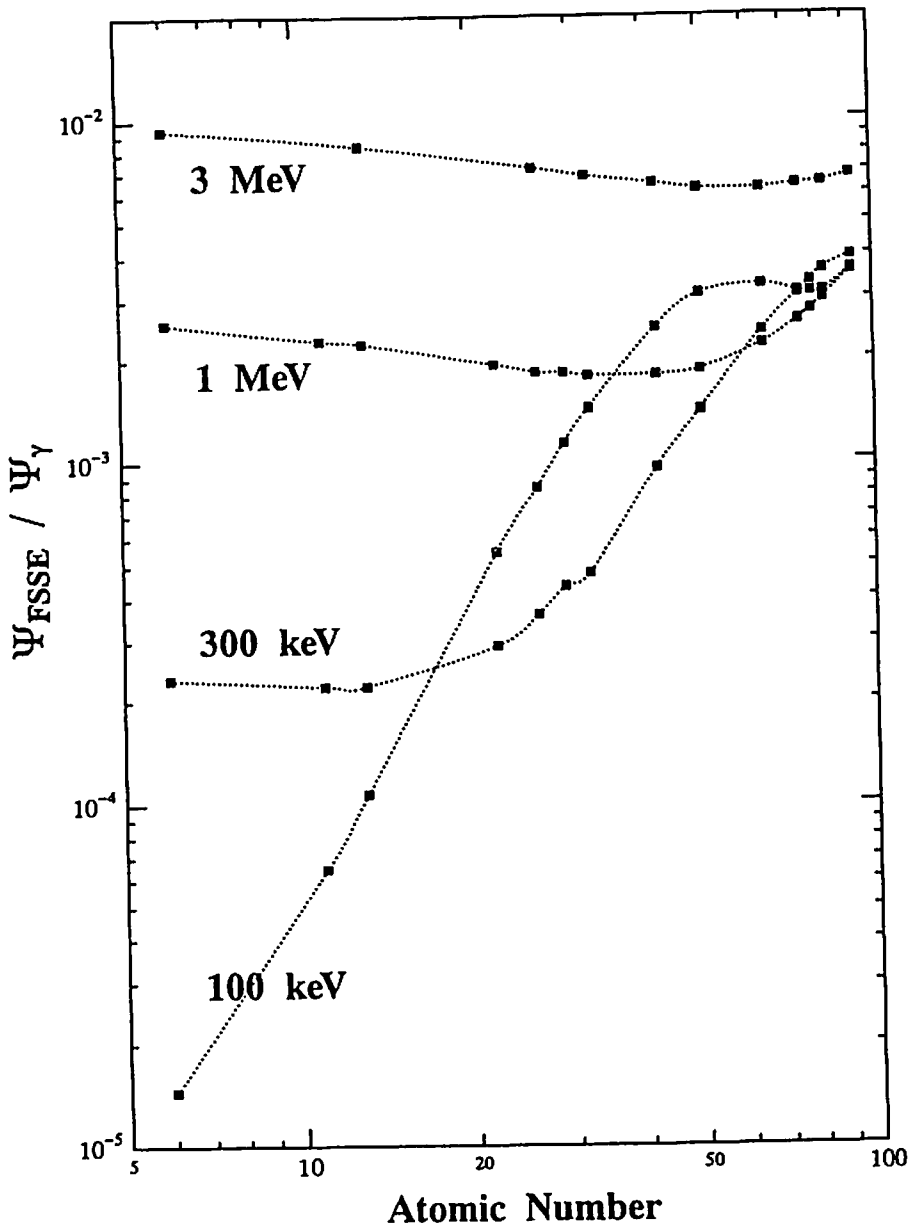

Fig.5 Material and Energy dependence of the yield of FSSE. The ordinate is scaled with logarithm of the ratio of energy fluence of FSSE to that of incident photons.

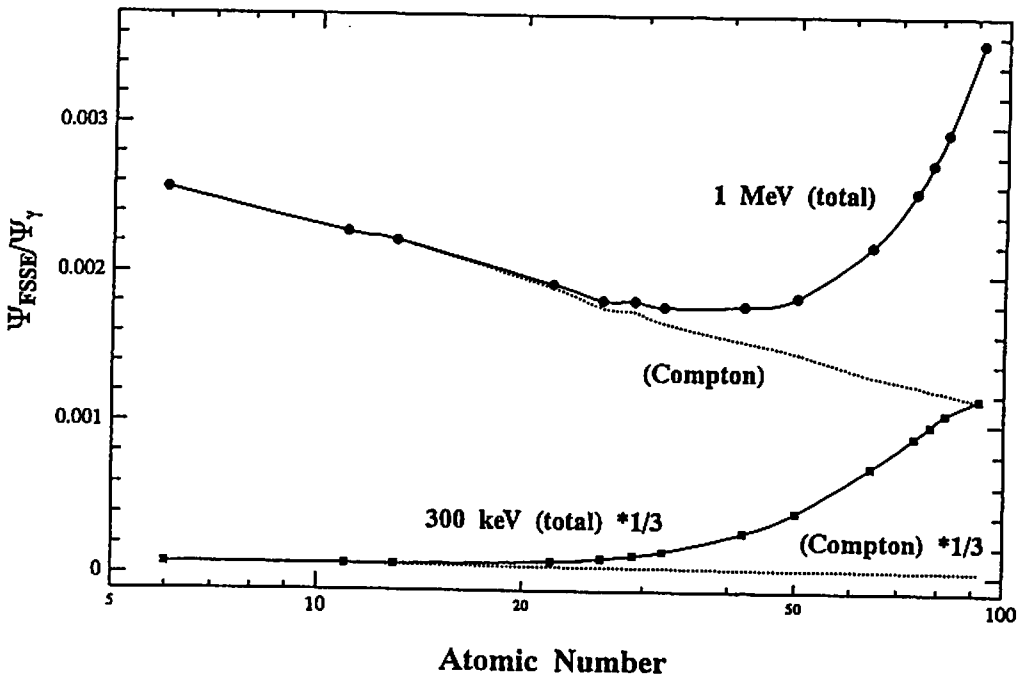

Fig.6 Contributions of Compton electron and photoelectron to the yield of FSSE.

CHARACTERIZATION OF ^{13}N AND ^{15}O INDUCED IN AIR OF A HIGH ENERGY ELECTRON ACCELERATOR ROOM

A. ENDO, J. HENSHAW* and M.A. MIGNANELLI*

Department of Health Physics,
Japan Atomic Energy Research Institute,
Tokai, Ibaraki 319-11, Japan

* *Materials and Chemistry Group,*
AEA Technology plc,
Harwell, Didcot,
Oxfordshire OX11 0RA, United Kingdom

Abstract

The amounts of ^{13}N and ^{15}O, present as aerosol and gas in the air of a 100 MeV electron linear accelerator (linac) facility, were analyzed along with their chemical forms. Measurements showed that most of the ^{13}N and ^{15}O are gaseous forms and that their chemical forms are N_2, O_2, NO_x and O_3. Simulations with EGS4 and a radiation chemistry model were performed to study the chemical reactions of ^{13}N and ^{15}O with the radiolytic products of the air molecules. From the comparison between the experiment and simulations, significant factors that control the chemical compositions of ^{13}N and ^{15}O were identified.

1. Introduction

During the operation of high energy accelerators, the primary and secondary particles produce various radionuclides in the gaseous atmosphere through the spallation, photonuclear, and neutron capture reactions of the air nuclei and the machine components. The significant radionuclides observed in a high energy electron accelerator are ^{13}N and ^{15}O generated by the (γ, n) reactions of ^{14}N and ^{16}O. These radionuclides are present as both aerosols and gases and become a potential source of radiation exposure. In estimating internal doses due to the inhalation of the induced airborne radionuclides, their physicochemical properties, such as the particle size of the aerosols and the chemical form of the gases, are significant factors. This is because these factors affect the transport, deposition, and clearance of the inhaled radionuclides in the respiratory tract.

We have measured the fractions of aerosol and gaseous components of the ^{13}N and ^{15}O species generated in a 100 MeV electron linac facility and analyzed their chemical compositions. Computer simulations with EGS4 and a radiation chemistry model were performed to analyze the observed chemical compositions of ^{13}N and ^{15}O, and the significant factors that control the chemical reactions of ^{13}N and ^{15}O are discussed.

2. Experiment

The experiment was carried out in the JAERI 100MeV electron linac facility (Fig. 1) [1]. An electron beam was operated at 100 MeV kinetic energy, 1 μs pulse width, 50 pps repetition frequency, and 10 μA average current and was incident to a copper target of 6.0 cm thickness and 2.2 cm diameter. The activated air was evacuated from the target room through a steel pipe to a measuring system placed in a low radiation area outside the concrete shielding. The concentrations of aerosol and gaseous components were measured using a particulate air sampling filter and a gas flow-through ionization chamber, respectively. The chemical forms of the gaseous components were analyzed by a radio-gas chromatograph.

3. Simulations

The observed chemical compositions of ^{13}N and ^{15}O were analyzed by computer simulations using EGS4 and a radiation chemistry model. In order to simulate the chemical reactions of ^{13}N and ^{15}O, it is required to obtain concentrations of ^{13}N, ^{15}O, and the primary radiolytic products from the air molecules and to solve the set of chemical rate equations that would be expected for their reactions. The procedures to calculate these parameters are described below.

3.1 EGS4 simulation

Monte Carlo simulations with the EGS4 code [2] were performed to get the photon fluence spectrum and energy deposition in the air. These quantities are used to calculate the concentrations of ^{13}N, ^{15}O, and the primary radiolytic products. First, the angular dependence of bremsstrahlung spectra was calculated to identify the region where the (γ, n) reactions of the air nuclei occur. Figure 2 shows a simulation geometry. A monoenergetic electron beam of 100 MeV was incident on the central axis of the copper target and photon fluence spectra were obtained for 18 regions, covering θ from 0° to 180°, by scoring the track lengths of photons in each region. On the basis of the simulation, the value of θ that covers a significant region for the air activation was determined. Next,

the photon fluence spectrum and energy deposition in this region were calculated. Cut off energies were set at 1 MeV for electrons and positrons and at 1 keV for photons in all the simulations.

The concentrations of ^{13}N and ^{15}O were calculated based on the photon fluence spectrum and the cross sections of the (γ, n) reactions. The rates of production of primary radiolytic products were calculated from the energy deposition rate and the G values, the number of species produced per 100 eV energy absorbed [3].

3.2 Radiation chemistry model

There are two significant steps to determine the chemical forms of ^{13}N and ^{15}O generated by the (γ, n) reactions; the first step is the hot atom process and the second one is the chemical reactions with the air molecules and the primary radiolytic products. In the present simulation, we assume several kinds of chemical forms of thermalized ^{13}N and ^{15}O just after the completion of the hot atom process by the (γ, n) reaction and study the following chemical reactions with the air molecules and the primary radiolytic products.

The chemistry model employed was based on the model used in the previous study [4], which was developed to simulate the radiolysis of air. The model consists of 94 chemical reactions involving ions, radicals and molecules that are considered to be important for the radiolysis of N_2, O_2, and H_2O. The model was extended to account for the chemical reactions of ^{13}N and ^{15}O species, and 700 chemical reactions in all were prepared for the present simulations. By solving the chemical rate equations for these reactions simultaneously using the FACSIMILE code [5], a computer code developed to solve stiff differential equations, we can obtain the time-dependent concentrations of the ^{13}N and ^{15}O species.

The chemical forms of ^{13}N and ^{15}O thermalized just after the completion of the hot atom process by the (γ, n) reaction were considered to involve ^{13}N atom, ^{13}NN, ^{15}O atom, and ^{15}OO. It was assumed that ^{13}N and ^{15}O are generated as these initial species with the concentrations calculated, as outlined in subsection 3.1. The chemical reactions of these initial species with the air molecules and the primary radiolytic products were followed by performing the numerical integration with FACSIMILE.

4. Results and Discussion

Figure 3 shows the compositions of ^{13}N and ^{15}O observed in the JAERI 100 MeV electron linac. It was found that more than 98 % of ^{13}N and ^{15}O are present as gaseous species and that their chemical forms are a mixture of N_2, O_2, NO_x and O_3.

Figure 4 shows ratios of the saturated activities of ^{13}N and ^{15}O calculated from the photon spectrum in each region. The ordinate is expressed as ratios for the activities

produced in the 0°– 5° region. It was found that the generated activities drastically decrease with increasing θ and that more than 90 % of the total activities for both ^{13}N and ^{15}O are included in the θ range between 0° and 35°. These results suggest that the (γ, n) reactions of the air nuclei mainly occur in the cone region of which θ is up to 35°. On the basis of the result, the photon fluence spectrum and energy deposition were calculated for a cone region, for which θ is 35°, and the concentrations of ^{13}N, ^{15}O and the primary radiolytic products were calculated.

Figure 5 shows the time-dependent concentrations of ^{13}N and ^{15}O species generated from the ^{13}N and ^{15}O atoms. The significant species for ^{13}N is ^{13}N atom up to 10^{-4} s of the irradiation time. At 10^{-3} s, the concentration of ^{13}NO, produced by the following reaction, becomes comparable with that of ^{13}N.

$$^{13}N + O_2 = {}^{13}NO + O$$

Later, ^{13}NO further reacts with the radiolytic products to produce other nitrogen oxide compounds and the ^{13}NN molecule.

For ^{15}O, the concentration of $^{15}OO_2$ becomes comparable with that of the ^{15}O atom at 10^{-5} s and increases up to 10^{-1} s. After that, the $^{15}OO_2$ concentration decreases since it reacts with N and O atoms and NO, generated from the radiolysis of air, to form various nitrogen oxide compounds and the ^{15}OO molecule.

Figure 6 shows the calculated results for which ^{13}N and ^{15}O are generated as ^{13}NN and ^{15}OO, respectively. ^{13}NN and ^{15}OO are the only species observed within the range of the irradiation time of concern. This is because although nitrogen and oxygen molecules, involving N_2, ^{13}NN, O_2 and ^{15}OO, take part in the chemical reactions with the primary radiolytic products, the isotopes make up only a small fraction of the gas molecules that participate in the chemical reactions.

It was found from the experiment that ^{13}N and ^{15}O produced in the 100 MeV electron linac room are mainly present as gaseous species and that their chemical forms are a mixture of N_2, O_2, NO_x and O_3. The simulations with the radiation chemistry model showed that such compositions could not be calculated if ^{13}N and ^{15}O are generated as either atoms (^{13}N, ^{15}O) or molecules (^{13}NN, ^{15}OO) by the (γ, n) reactions. From a comparison between the experiment and simulations, it is suggested that thermalized ^{13}N and ^{15}O are present as both atoms (^{13}N, ^{15}O) and molecules (^{13}NN, ^{15}OO) and that, of these species, ^{13}N and ^{15}O atoms are converted into nitrogen oxides and ozone through the reactions with the primary radiolytic products. Estimation of the fractions of atoms (^{13}N and ^{15}O) and molecules (^{13}NN and ^{15}OO) just after the hot atom process and further analysis of the reaction mechanism are in progress [6].

5. Conclusion

The fractions of aerosol and gaseous components and their chemical forms were analyzed for ^{13}N and ^{15}O induced through the (γ, n) reactions in the air of the JAERI 100 MeV electron linac facility. It was found that most of the ^{13}N and ^{15}O are present as gaseous forms and that their chemical forms are N_2, O_2, NO_x and O_3. Computer simulations with EGS4 and a radiation chemistry model have been performed. Comparison between the experimental results and the simulations have showed that ^{13}N and ^{15}O atoms, generated by the (γ, n) reactions, react with the primary radiolytic products of air and produce nitrogen oxide compounds and ozone. However, molecular ^{13}NN and ^{15}OO remain in their initial chemical forms.

References

[1] A. Endo, M. Kikuchi, S. Izawa and Y. Ikezawa. *Characteristics of the chemical forms of ^{11}C, ^{13}N and ^{15}O induced in air by the operation of a 100 MeV electron linear accelerator.* Health Phys., **68**, 80–88 (1995).

[2] W.R. Nelson, H. Hirayama and D.W.O. Rogers. *The EGS4 Code System.* SLAC-265 (1985).

[3] C. Willis and A.W. Boyd. *Excitation in the radiation chemistry of inorganic gases.* Int. J. Radiat. Phys. Chem., **8**, 71–111 (1976).

[4] A. Endo, J. Henshaw and M.A. Mignanelli. *Computer simulation method to predict concentrations of noxious gases in electron accelerator rooms.* AEAT-0058 (1996).

[5] A.R. Curtis and W.P. Sweetenham. *FACSIMILE/CHEKMAT user's manual.* AERE R 12805 (1988).

[6] A. Endo, J. Henshaw and M.A. Mignanelli. *to be published.*

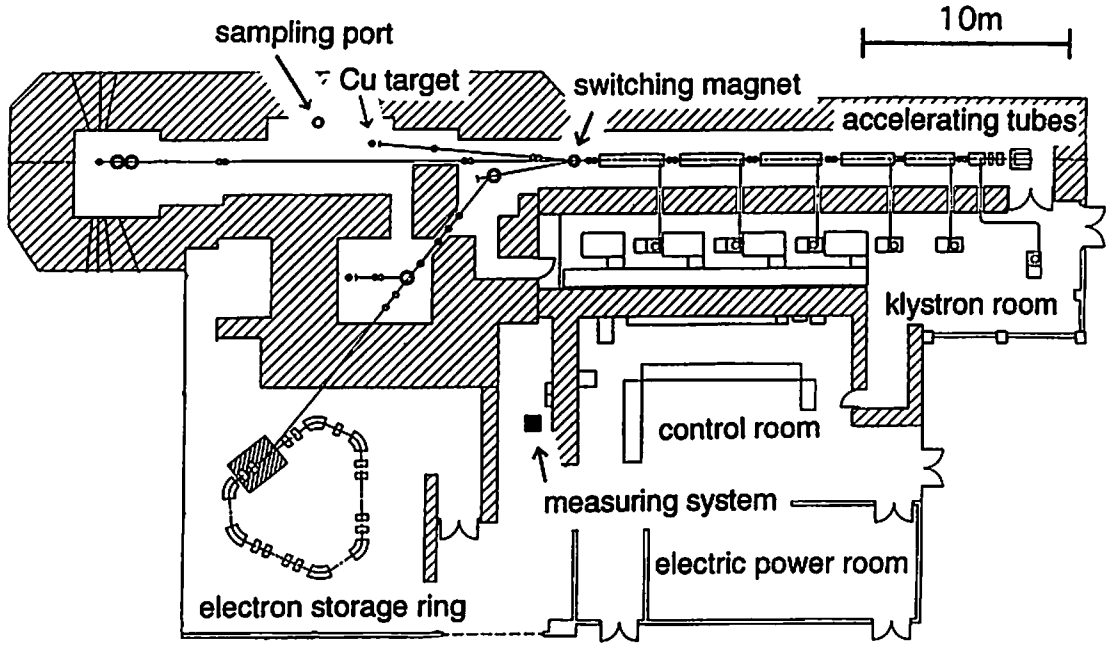

Figure 1. Electron linac facility of JAERI and configurations of the copper target and the measuring system.

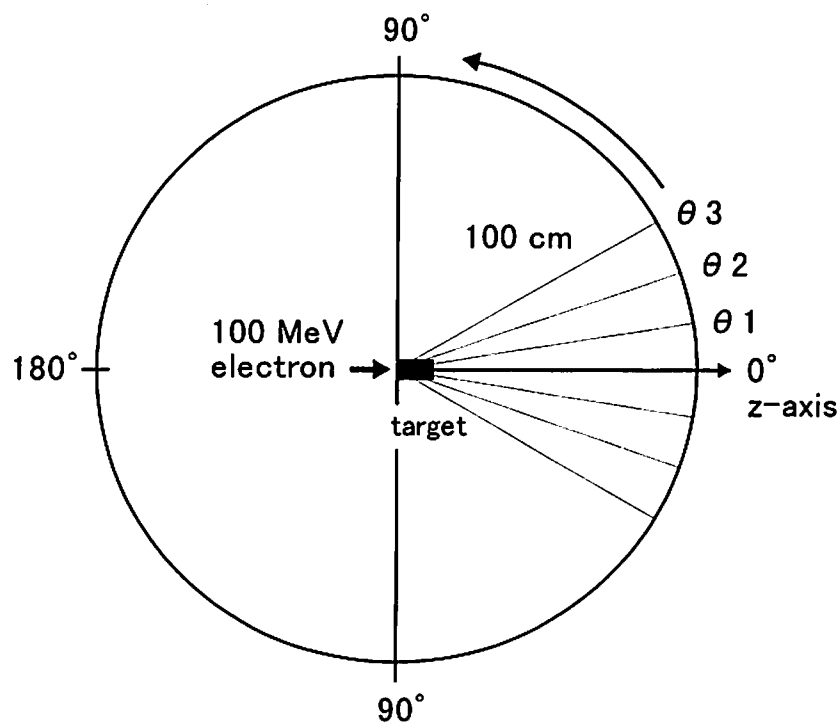

Figure 2. Simulation geometry for calculating angular dependence of bremsstrahlung spectra.

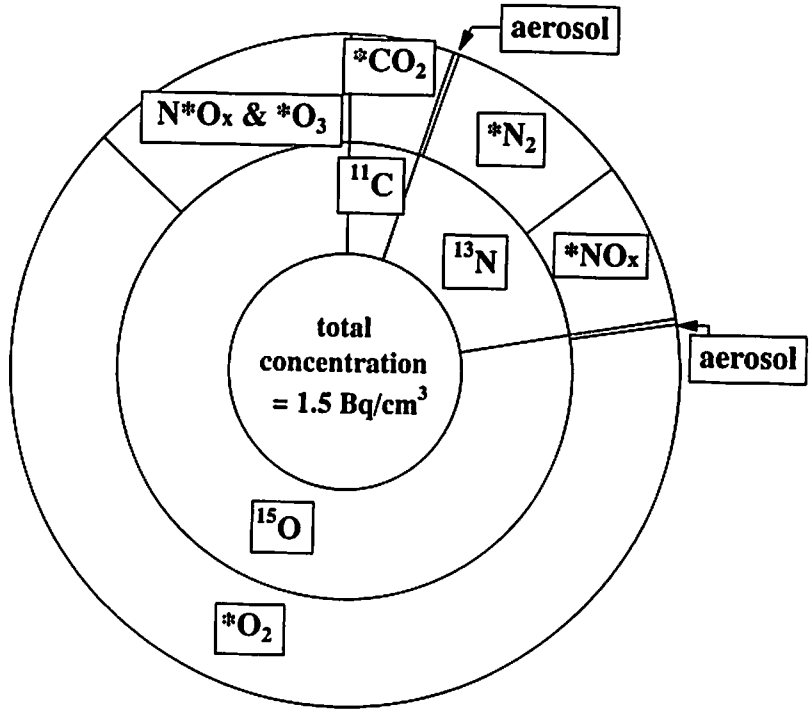

Figure 3. Compositions of induced airborne radionuclides observed in the JAERI electron linac. The inner graph shows the compositions of the radionuclides and the outer one shows their chemical compositions. Radionuclides are denoted as *C, *N and *O.

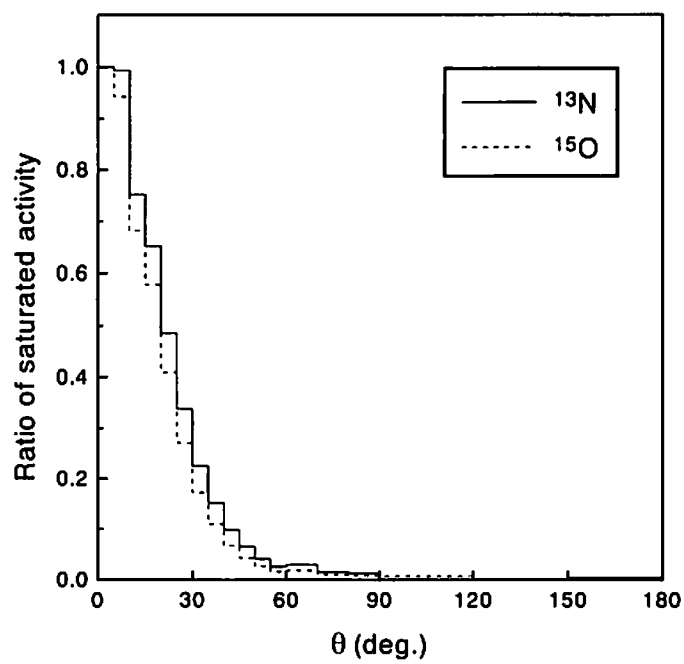

Figure 4. Angular dependence of the radioactivities of ^{13}N and ^{15}O generated.

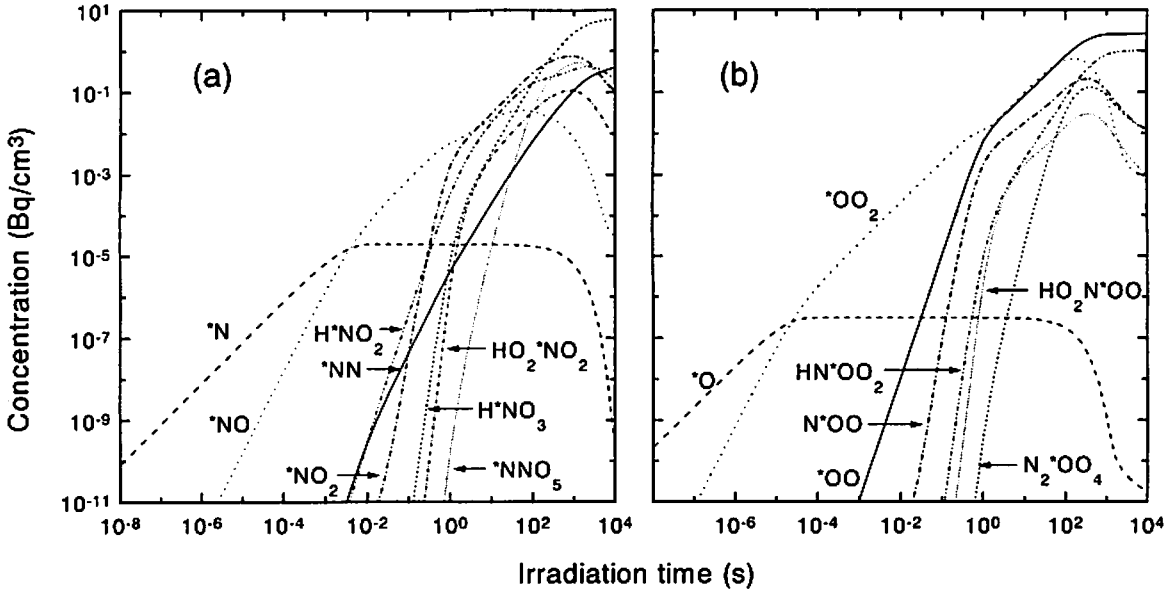

Figure 5. Time-dependent compositions of ^{13}N and ^{15}O species for which ^{13}N and ^{15}O are generated as ^{13}N and ^{15}O atoms by the (γ, n) reaction. (a) ^{13}N species, (b) ^{15}O species. ^{13}N and ^{15}O are denoted as *N and *O, respectively.

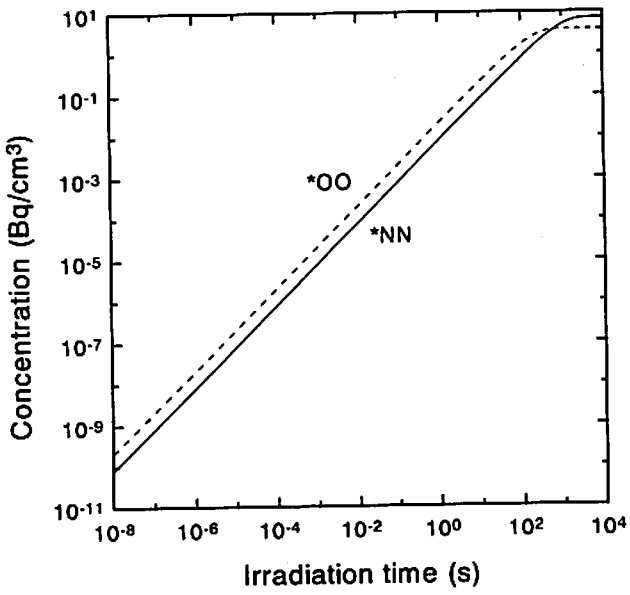

Figure 6. Time-dependent compositions of ^{13}N and ^{15}O species for which ^{13}N and ^{15}O are generated as ^{13}NN and ^{15}OO molecules by the (γ, n) reaction. ^{13}N and ^{15}O are denoted as *N and *O, respectively.

ANALYSIS OF $4\pi\gamma$ IONIZATION CHAMBER RESPONSE USING EGS4 MONTE CARLO CODE

H. SUZUKI, K. SIBAIKE, H. HASHIMOTO AND Y. KAWADA

Faculty of Engineering, Seikei University
3-3-1 Kitijoji Kitamachi, Musasino-shi, Tokyo 180, Japan

Y. HINO

Electrotechnical Laboratory
1-1-4 Umezono, Tsukuba, Ibaraki 305, Japan

1. Introduction

Pressurized $4\pi\gamma$ ionization chambers are often used as secondary standard instruments for radioactivity measurements of γ-ray emitting nuclides. When the detector of this kind is calibrated for the incident γ-ray energy more than 200 keV, the shape of the response curve as a function of the γ-ray energy is monotonous, and it is easy to determine the response curve by fitting experimental data obtained with only limited number of standard sources of different nuclides.

However, in the lower energy region below 200keV, the shape of the response curve is not simple and very dependent of the materials and size of the chamber wall and the filling gas. In this lower energy region, moreover, it is rather difficult to find suitable standard sources emitting only single photon per decay.

Theoretical calculations based upon analytical means or Monte Carlo simulations are therefore very helpful to determine the response curve in this lower energy region[1]. In this study, the energy response curves of three different types of pressurized $4\pi\gamma$ ionization chambers were studied by adopting EGS4 Monte Carlo simulation code[2], and were compared with the experimental results. The effects of the axial and radial displacements of source position from center were also demonstrated.

2. Method of Calculation

The average energy deposition in the gases within the pressurized $4\pi\gamma$ ionization cham-

bers per one emission of a γ-ray has been calculated using EGS4 Monte Carlo simulation code. The ionization current I(A) is given by

$$I = EAe/W \tag{1}$$

where

E : average energy deposited in the gas per one emission of γ-ray (eV),

A : total γ-ray emission rate as expressed by equivalent activity (Bq),

e : electron charge (C) and

W : average energy expended in the creation of an ion pair in the gas (eV).

We adopted 26.4 eV for argon and 34.8 eV for nitrogen, respectively. We calculated the response of several types of pressurized $4\pi\gamma$ pressure ionization chambers; Centronics IG11/A10 (filled with 1 MPa argon, 1 inch diameter reentrant well), Centronics IG11/A20 (2 MPa argon, 1 inch diameter reentrant well) and Centronic IG12/N20 (2 MPa nitrogen, 2 inch diameter reentrant well). All these chambers were manufactured by Centronic Ltd. according to the original design by Sharpe and Wade[3]. The sectional view of the IG11 chambers are shown in Fig.1.

The responses as a function of the photon energy were calculated for monoenergtic photons emitted from a point source located at the center of the reentrant well, and were compared with experimental results. The vaiation of ionization current due to the axial and radial displacement of source position, as illustrated in Fig.2 and Fig.3, were also investigated.

3. Results and Discussions

The calculated results of the response, ionization current per one emission of photon, are shown in Figs.4~5 as a function of photon energy (closed triangles and squares) together with experimental results (open triangles and squares) obtained with ampoule sealed radioactivity standard solutions of eleven different nuclides such as ^{241}Am, ^{109}Cd, ^{51}Cr, ^{85}Sr, ^{137}Cs, ^{60}Co etc.[4]. The results of more detailed calculation in the lower energy part are shown in Fig.6. The calculations agreed well with the experimental ones for all these cases.

Calculated results of changes of ionization current due to the axial displacement of the source position in the use of the IG11/A20 are shown in Fig.7. As was expected, the center position gave the highest sensitivity, and the response decreases gradually with increasing the distance from the center. In the above position dependence curve, a critical

unsymmetry was seen, which should be due to the difference in the structure of the top and bottom parts of the chamber.

The effect of the radial displacement of the source position were examined carefully by the use of the EGS4 code, and the results are shown in Fig.8 in the case of IG12/N20. It should be noted here that higher response was obtained in the off-center position than the response in the center position. In the lower energy region below 200 keV, however, highest response was obtained at the central axis.

4. Conclusion

Monte Calro calculations of the response of three different types of pressurized reentrant chambers were made according to the EGS4 code. Excellent agreements between these calculations and the experimental results suggest that the use of EGS4 simulation code is very helpful for the fitting and/or interpolating of the response curve in the precise calibration of $4\pi\gamma$ chambers.

In the use of such kind of instruments as the secondary standards of radioactivity of γ/X ray emitting nuclides, precisions up to the order of 0.1% are often required and the possible effects of measuring conditions such as source positions, amounts of radioactive solution and size and material of source containers etc. should be taken into account to achieve this order of the precision. To evaluate and correct these effects, the EGS4 code is also very useful tool.

References

[1] T. Torii and Y. Hino, Proc. 4th EGS4 Users' Meeting in Japan (1994, KEK).

[2] W. R. Nelson, H. Hirayama and D. W. O.Rogers, The EGS4 Code System, SLAC Report 265 (1985).

[3] J. Sharpe and F. Wade, *T.P.A. Mk II ionization chamber*, AERE EL/R806 (1951), See also NCRP, A Handbook of Radioactivity Measurements Procedures, 2nd Ed., NCRP Report No.58 pp. 215-218 (1984).

[4] Y. Hino Y. Kawada and Nazaroh, Nucl. Instrum. Methods **A 369**, 392-396(1996).

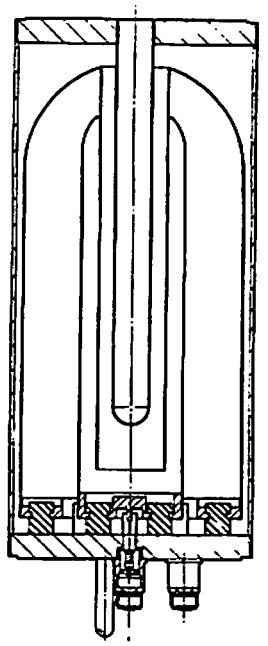

Fig.1 Sectional view of a one-inch-diameter reentrant-well IG=11 pressure ionization chamber

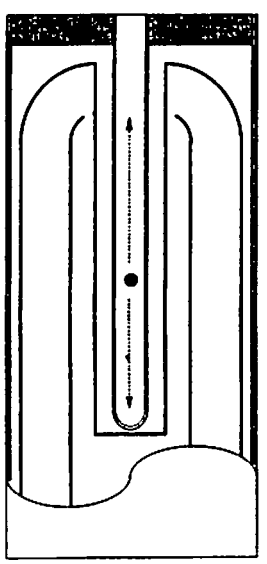

Fig.2 Axial displacement of source position

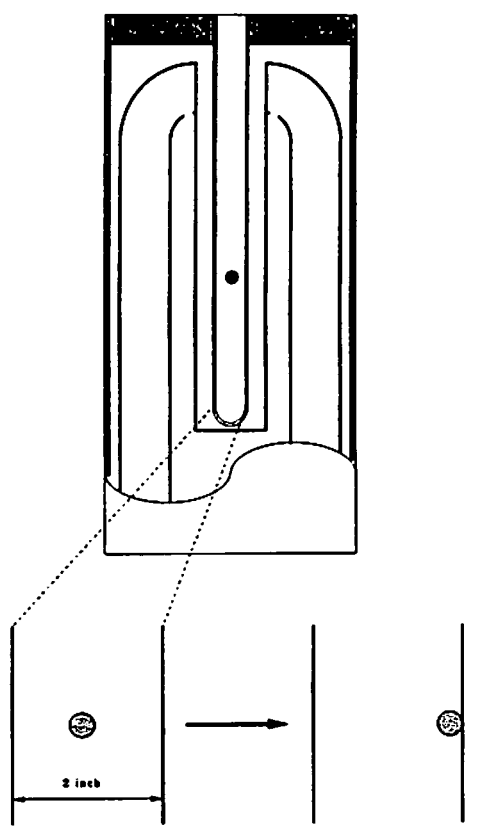

Fig.3 Radial displacement of source position

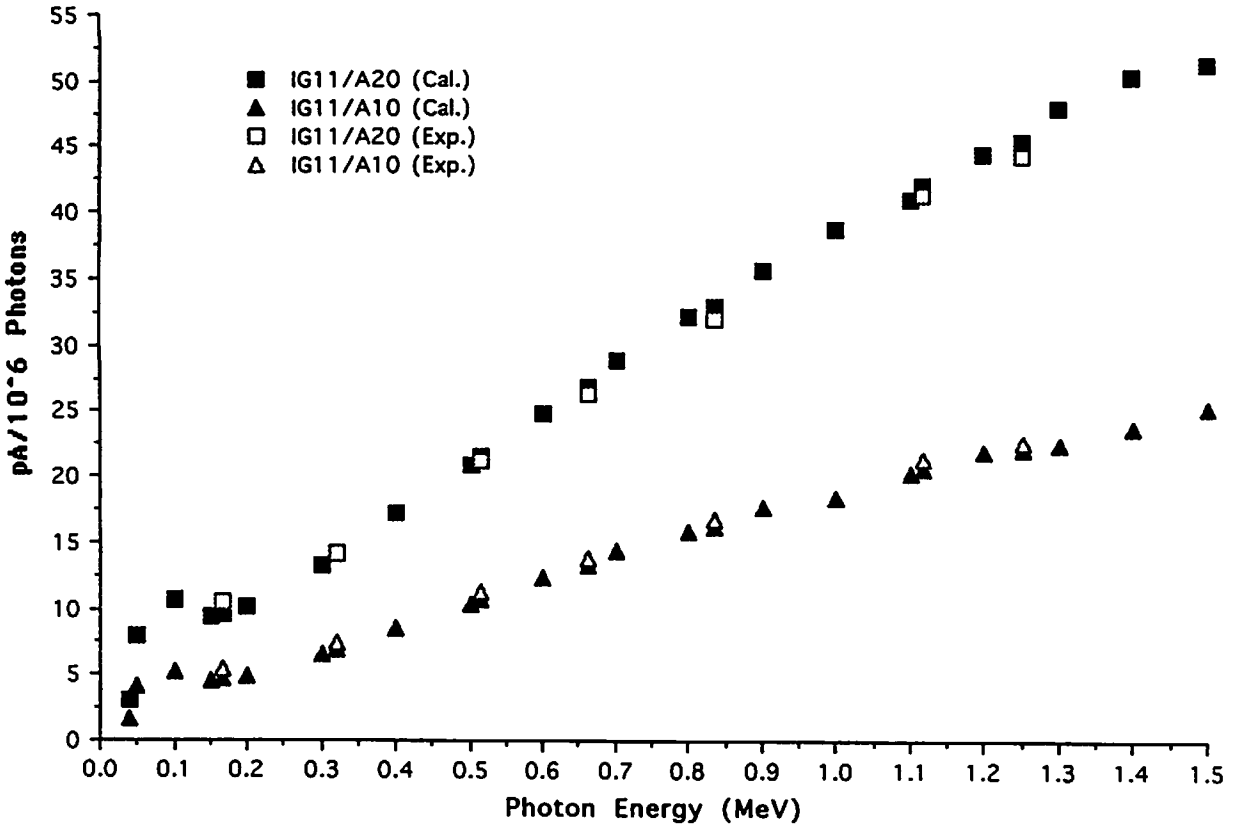

Fig.4 Response function of ionization chambers (filled with 1 MPa or 2 MPa argon)

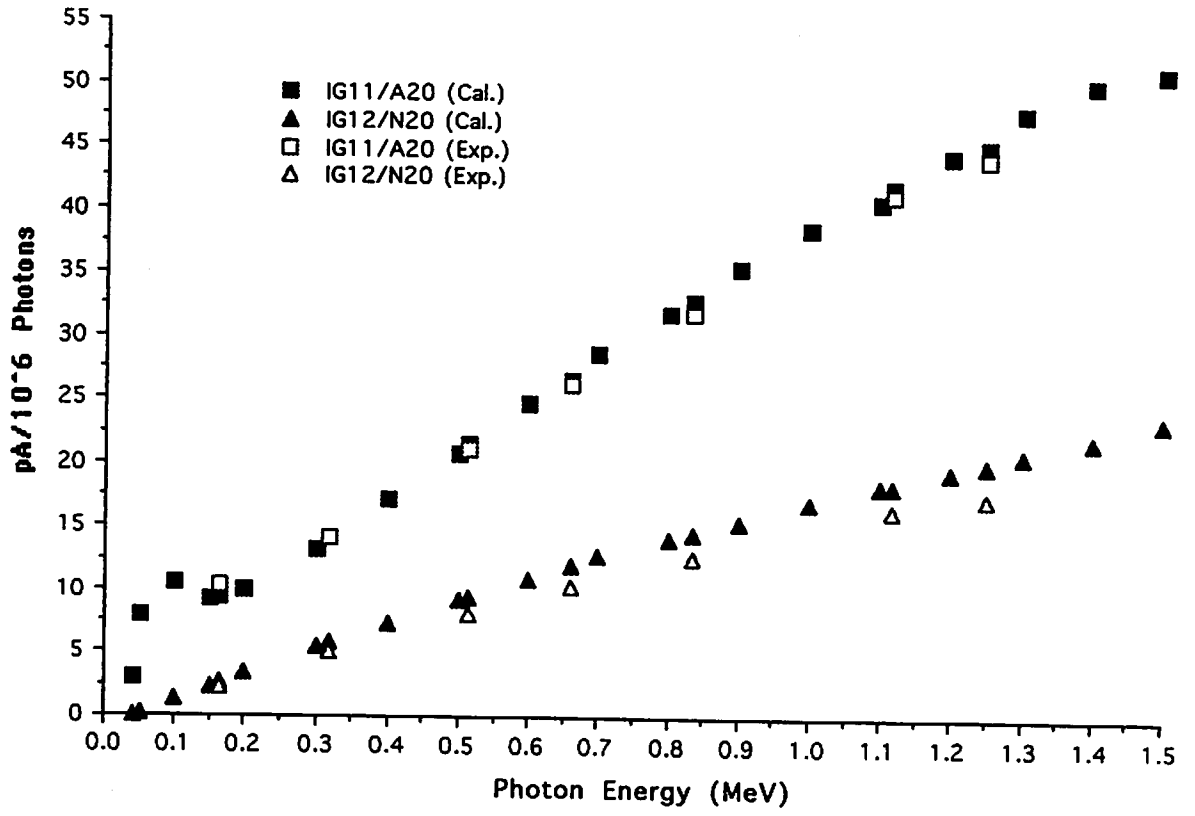

Fig.5 Response function of ionization chambers (filled with 2 MPa argon or nitogen)

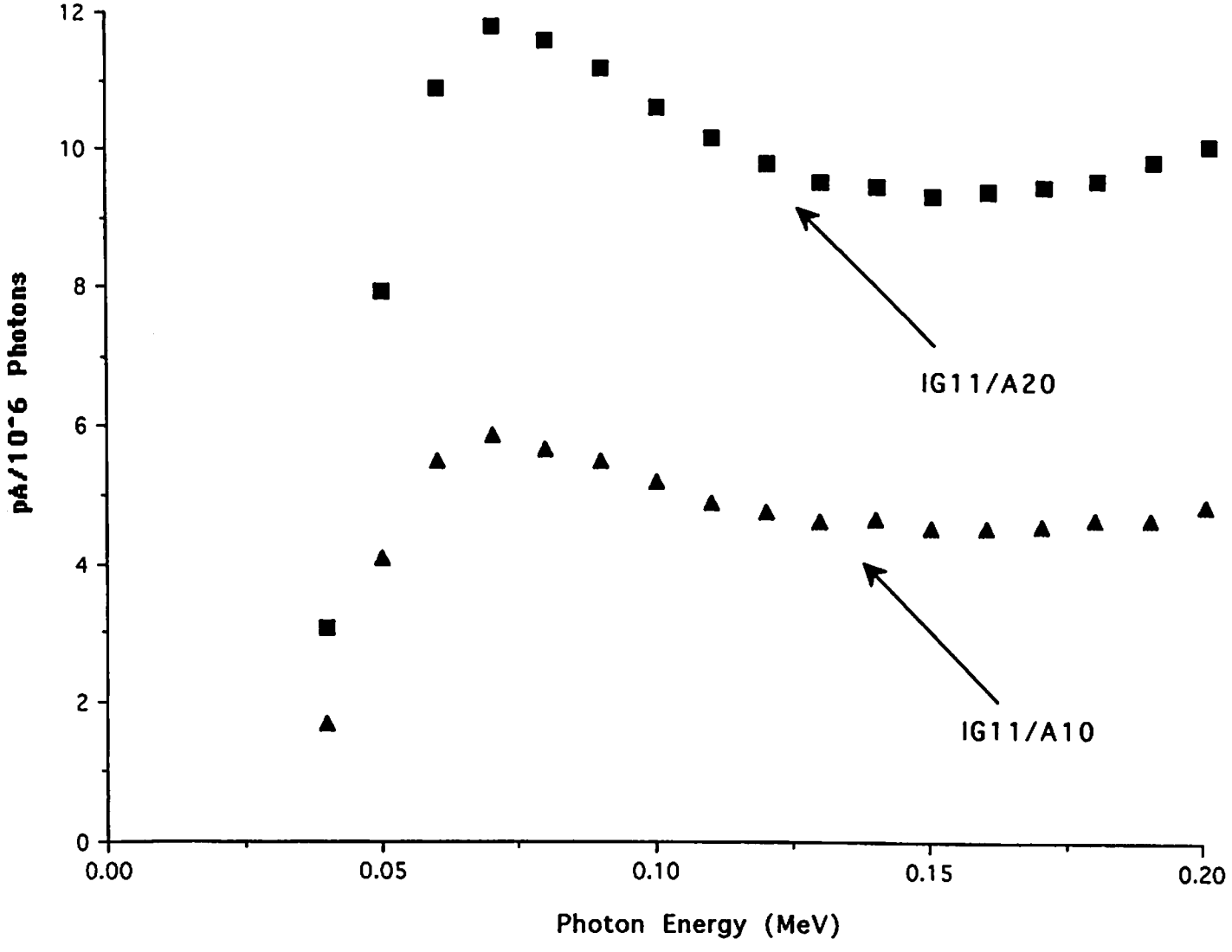

Fig.6 Response function of ionization chambers in the lower energy region (filled with 1 MPa or 2 MPa argon)

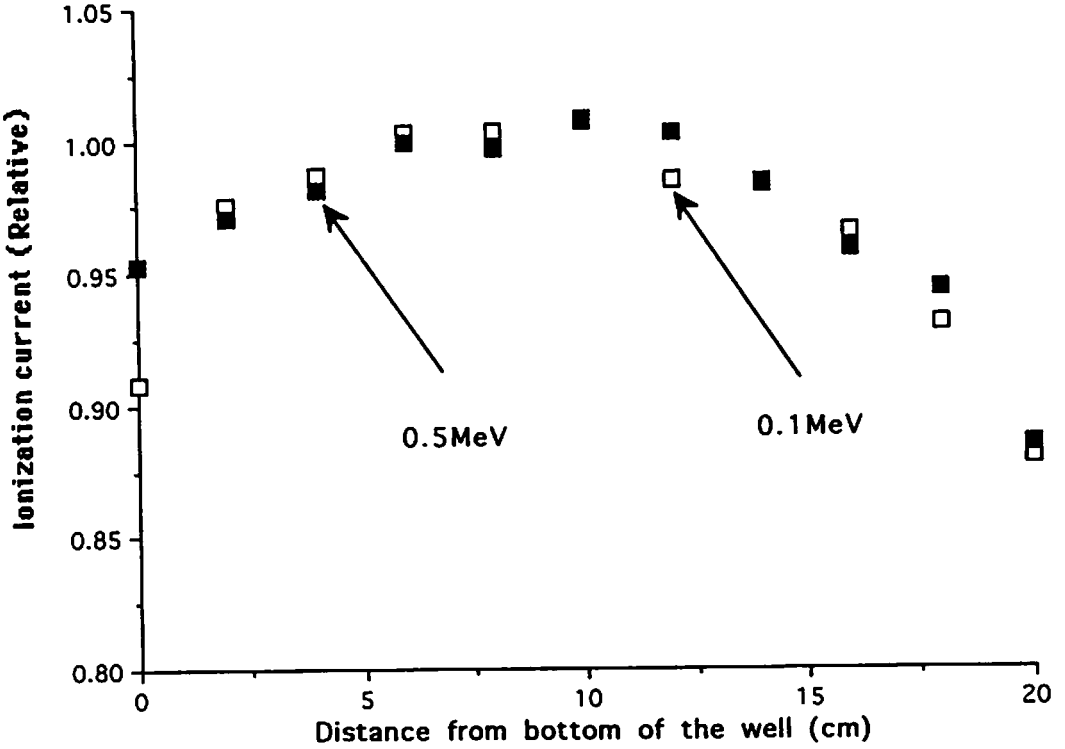

Fig.7 Change of the ionization current due to axial displacement of the source position

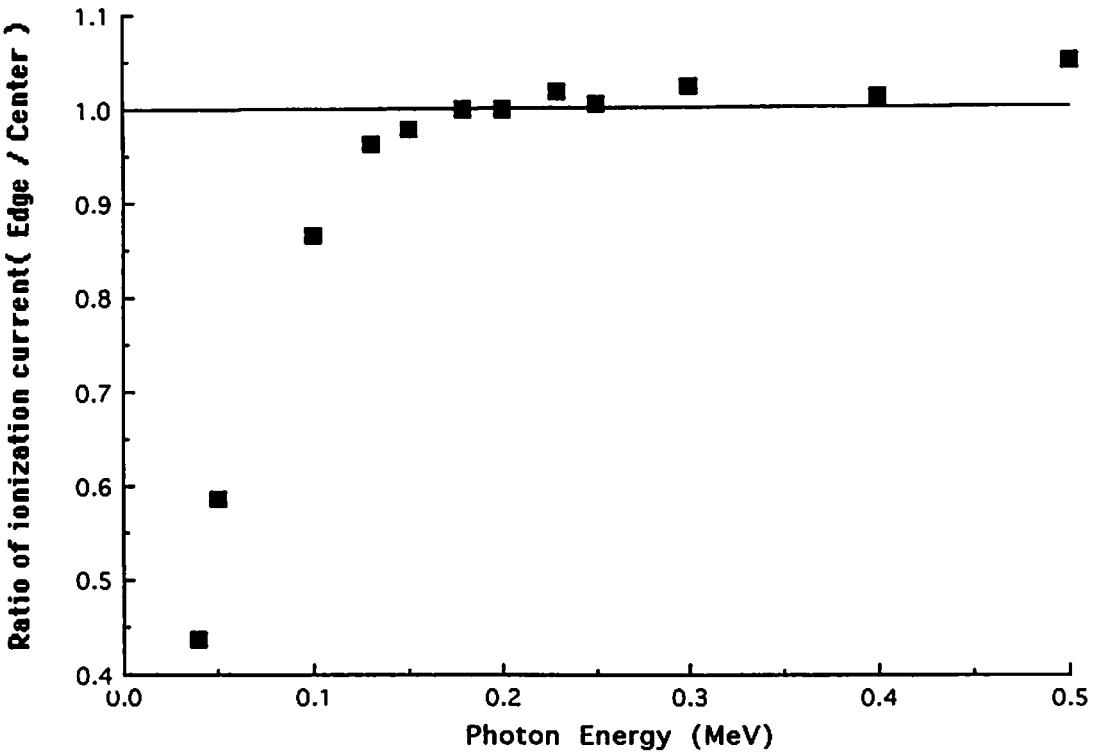

Fig.8 Change of the ionization current due to radial displacement of the source position

RESPONSE FUNCTIONS OF A GE DETECTOR TO COMPTON BACKSCATTERED PHOTONS CALCULATED BY EGS4/PRESTA CODE

K. KUDO, N. TAKEDA, A. FUKUDA, T. NOGUCHI, H. OHGAKI, T. YAMAZAKI

Quantum Radiation Division, Electrotechnical Laboratory
1-1-4 Umezono, Tsukuba-shi, Ibaraki 305, Japan

and

T. SUGITA

Science System Laboratory
1342-6 Sumiyoshi, Tomobe-cho, Ibaraki 309-17, Japan

Abstract

The EGS4/PRESTA Monte Carlo code has been used to calculate response functions of a pure Ge detector to quasi-monoenergetic photons up to 10 MeV, which are produced by Compton backscattering of laser light with high energy electrons circulating in a storage ring of TERAS at the Electortechnical Laboratory (ETL). For the precise calculation, we took into account a detail configuration of the whole system in the EGS4 code, that is, a volume source of photons produced in a laser collision region with relativistic electrons, three lead collimators to define the energy spread of photons and a coaxial Ge detector with all physical processes necessary for accurate calculations at the electron energies from 350 MeV to 530 MeV. The calculated response functions showed relatively good agreement in shape with experimental response functions at some photon energies, however some difference tendency was seen in energy resolution at other energies. Both the integrated responses above 1.5 MeV showed the fairly good agreement with the maximum difference of 4 % at all energies of photons from 3.4 MeV to 10 MeV, after fitting the calculated result to the experimental pulse height distribution.

1. Introduction

For the precise measurement of γ-ray dose in the standard field of thermal neutrons at ETL, we have developed a new type of ^{3}He-filtered GM counter which consists of a commercially available GM counter surrounded by a ^{3}He gas filter to suppress the contribution of secondary γ-rays produced by thermal neutron captures in the GM counter itself [1]. For the calibration of γdetectors at the ETL standard fields of exposure dose, conventional γ-ray sources of ^{241}Am, ^{137}Cs and ^{60}Co etc. are available together with lower energy X-ray sources. However, high-energy photon fields have not been established for the calibration purpose above 2 MeV.

High energy photons produced by Compton backscattering of laser light on relativistic electrons in a storage ring provide one of the possibilities as a high-energy source for detector calibration [2]. Therefore, it is more desirable to investigate the basic characteristics of the photon field concerning the energy distribution of quasi-monoenergetic photons and the secondary photons produced in the lead collimators and in the ambient surroundings of experimental arrangement.

The recent released electron photon shower code EGS4 [3] has been proved reliably to calculate the response functions of NaI, Ge and NE213 detectors for photon energies up to 15 MeV [1, 4-6]. Therefore, in this paper, the EGS4/PRESTA Monte Carlo code has been used to calculate both the energy distribution in an irradiation field and the response function of a pure Ge detector to quasi-monoenergetic photons in the energy range from 3.4 MeV to 10 MeV. The results are compared with the pulse height spectra measured at the ETL facility.

2. Monte Carlo Simulations with the EGS4 Code

The EGS4 (Electron Gamma Shower Version 4) is a general code for the Monte Carlo simulation of the coupled transport of photons, electrons and positrons in three dimensional geometry for energies above 10 keV for electrons and positrons and above 1 keV for photons up to several TeV. The PRESTA (Parameter Reduced Electron-Step Transport Algorithm) routine was developed to minimize the dependence of the results on the step lengths in the electron transport simulation [7]. We therefore adopted the EGS4 code with the PRESTA routine to calculate the energy distribution of photons and the distribution of energy deposition in a 155 cm^3 coaxial type Ge detector (Type:IGC3519 manufactured by PRINCETON GAMMA-TECH, INC.).

The geometry routines were written according to the models shown in Fig.1 by taking into account a detail configuration of the whole system, that is, a volume source of photons produced in a laser collision region with relativistic electrons, three lead collimators to define the energy spread of photons and the coaxial Ge detector with all physical processes

necessary for accurate calculations in the electron energy region from 350 MeV to 530 MeV. The 527 nm coherent lights generated by an average power 20 W Nd-YLF laser were guided to the vacuum chamber located at the straight portion between two bending magnets and collided head-on with high energy electrons. The backscattered photon energy and the corresponding emission angle to the backward direction were randomly generated by following a kinematic formula for the Compton scattering [8], as an input data for the EGS4/PRESTA calculation. The electron beam divergence and the energy spread were ignored in the calculation. The volume source of photons was assumed to be a rectangular of 0.7mm x 0.5 mm x 1800 mm. In order to shorten the computing time, the maximum solid angle cone to the backward emission was selected to be a little larger than the first collimator diameter. Here, the solid angle was subtended by the surface of the lead collimator positioned at 750 cm apart from the center of the source. The coaxial type Ge detector was positioned at 920 cm from the center of the source shielded by the third lead collimator. The model of the Ge detector is shown in Fig.2. The detail dimension of the detector was assumed by the factory information. The high energy photons were incident along the axis of the cylindrical Ge detector.

3. Results and Discussion

The typical photon energy distribution is shown in Fig.3 under the calculating conditions of the electron energy of 530 MeV and the 5 mm diameter of the first lead collimator. The dotted curve shows the energy spectrum at the front surface of the Ge detector. In the energy region above 9 MeV, an unsymmetric quasi-monoenergetic peak can be seen with the maximum energy of 9.95 MeV with the energy spread of 7.5 % (FWHM). The secondary photon component occupied in the lower energy region below 2 MeV including the annihilation γ-rays at 0.511 MeV. The ratio of the secondary photons to the integrated counts was about 4.4 % in this case. From the results at several photon energies from 3.39 MeV to 9.95 MeV, the energy spread and the secondary photon ratio ranged from 3.0 % to 7.5 % and from 2.6 % to 4.4 %, respectively. The solid line in Fig. 3 shows the energy distribution at the end of the rectangular source emitted to the backward direction. The energy spread is obviously larger than that of the beam passing through the lead collimator. With the comparison of these curves, it is clear that the lead collimator plays important role to sharpen the energy spread. However, the photon yield decreases with the decrease of the size of the collimator. The optimum size of the lead collimator should be chosen for each calibration purpose considering both the photon yield and the energy spread.

Figs. 4-7 show comparisons in shape of measured spectra of pulse height and EGS4 calculations for the Ge detector at 3.39 MeV, 4.37 MeV, 8.85 MeV and 9.95 MeV of

quasi-monoenergetic photons. At all energies, they show a good agreement in shape after fitting the calculated result to the experimental spectrum. At 3.39 MeV as shown in Fig.4, there seems to be a discrepancy of the energy resolution at the full energy peak, the single and double escape peak region. In the case of the higher energies at 8.85 MeV and 9.95 MeV as shown in Figs.6 and 7 respectively, the full energy peaks do not appear clearly. It seems to be natural that an incident high energy photon produces a secondary high energy electron in the small limited place along the cylindrical axis in the front part of the Ge detector and for that reason the direct penetration probability becomes larger through the central electrode cavity (about 1 cm diameter and 4.3 cm length) with the increase of photon energy. This problem would be solved by using a larger volume detector or by arranging the Ge detector vertically to the direction of incident high energy photons so as to suppress the leakage of secondary electrons.

References

[1] K. Kudo, N. Takeda and A. Fukuda, IEEE Trans. Nucl. Sci., **43** (1996)1851.

[2] H. Ohgaki, S. Sugiyama, T. Yamazaki, T. Mikado, M. Chiwaki, K. Yamada, R. Suzuki, T. Noguchi and T. Tomimasu, IEEE Trans. Nucl. Sci., **38** (1991)386.

[3] W. R. Nelson, H. Hirayama and D. W. O. Roger, SLAC-Report-265 (1985).

[4] B. A. Faddegon, L. Van der Zwan, D. W. O. Rogers and C. K. Ross, Nucl. Instr. and Meth., **A301**(1991) 138.

[5] D. W. O. Rogers, Nucl. Instr. and Meth., **199**(1982) 531.

[6] L. Bueermann, S. Ding, S. Guldbakke, H. Klein, T. Novotny and M. Tichy, Nucl. Instr. and Meth., **A332**(1993)483.

[7] A. F. Bielajew and D. W. O. Rogers, Nucl. Instr. and Meth., **B18**(1987)165.

[8] J. J. Murray and P. R. Klein, SLAC-TN-67-19 (1967).

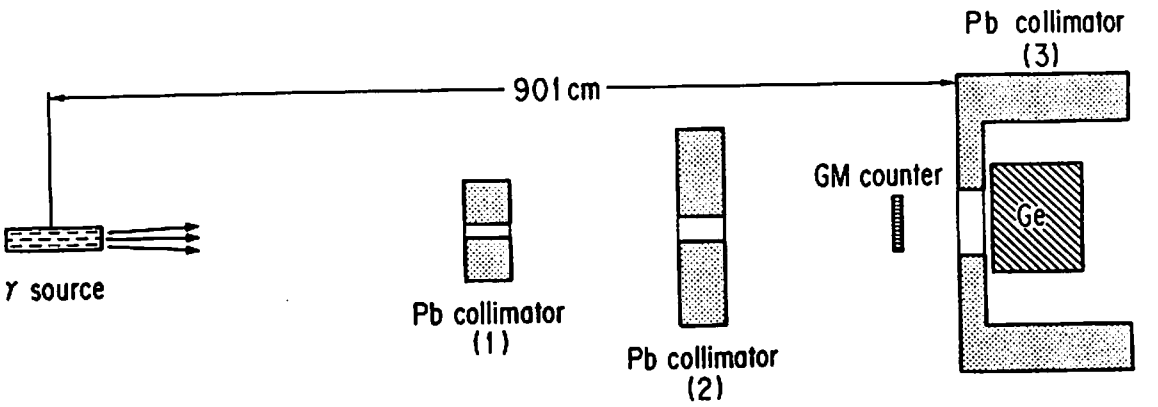

Fig.1 EGS4/PRESTA calculation model for the facility of laser-induced Compton backscattered photons

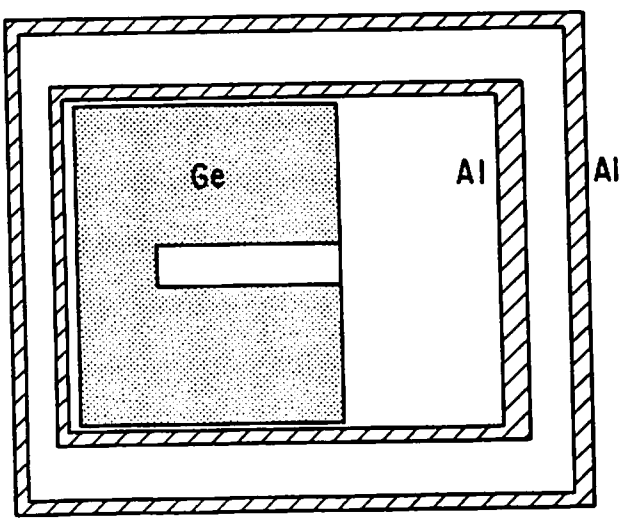

Fig.2 EGS4/PRESTA calculation model for a Ge detector

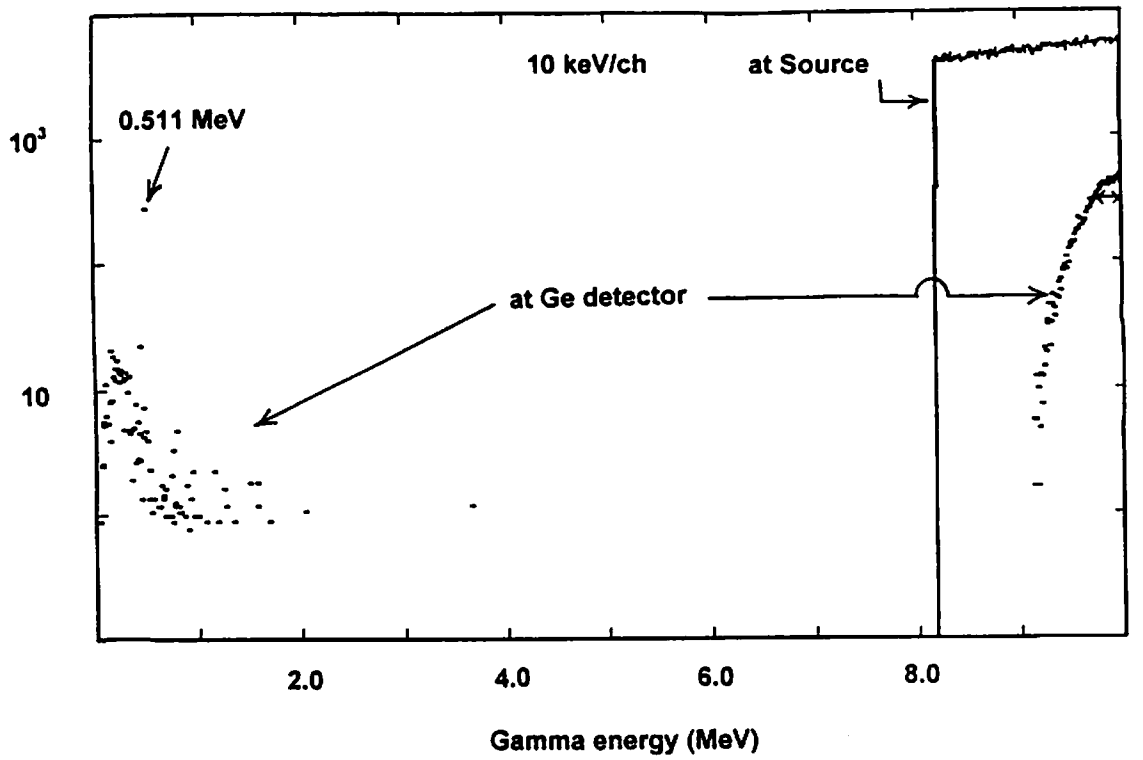

Fig.3 Photon energy distributions at the surface of a Ge detector (dotted curve) and at the end of the rectangular source (solid line) at the electron energy of 530 MeV

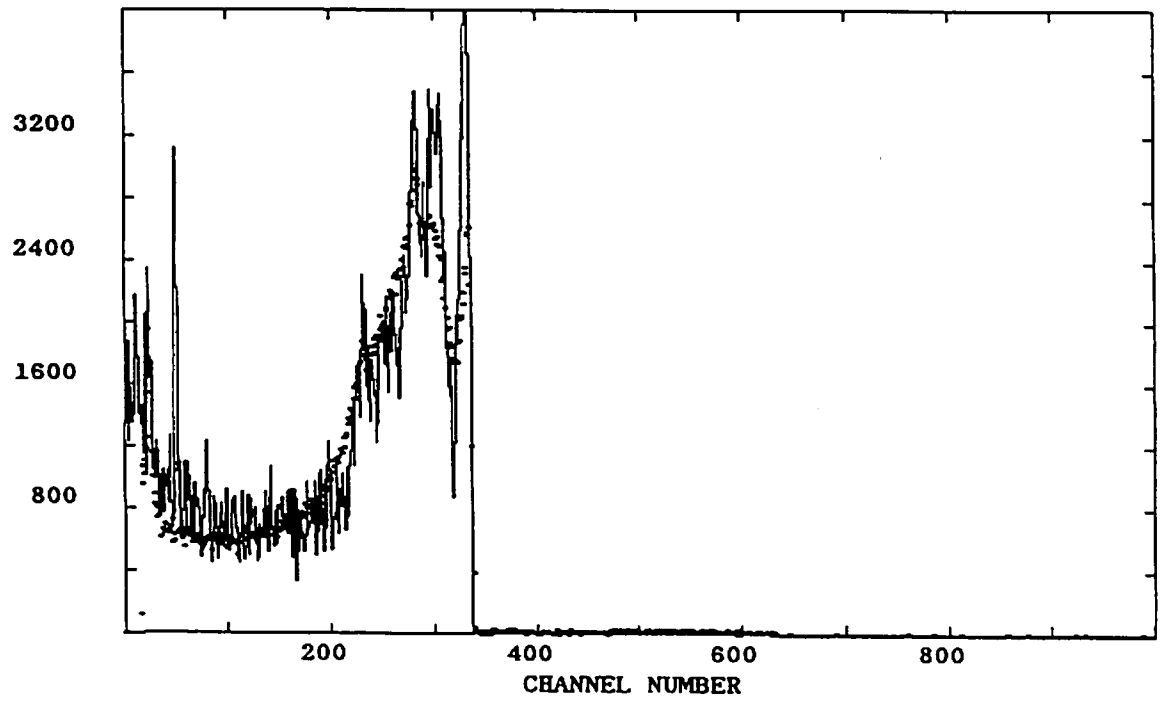

Fig.4 Comparison of measured and calculated pulse height spectra for a Ge detector to 3.39 MeV quasi-monoenergetic photons

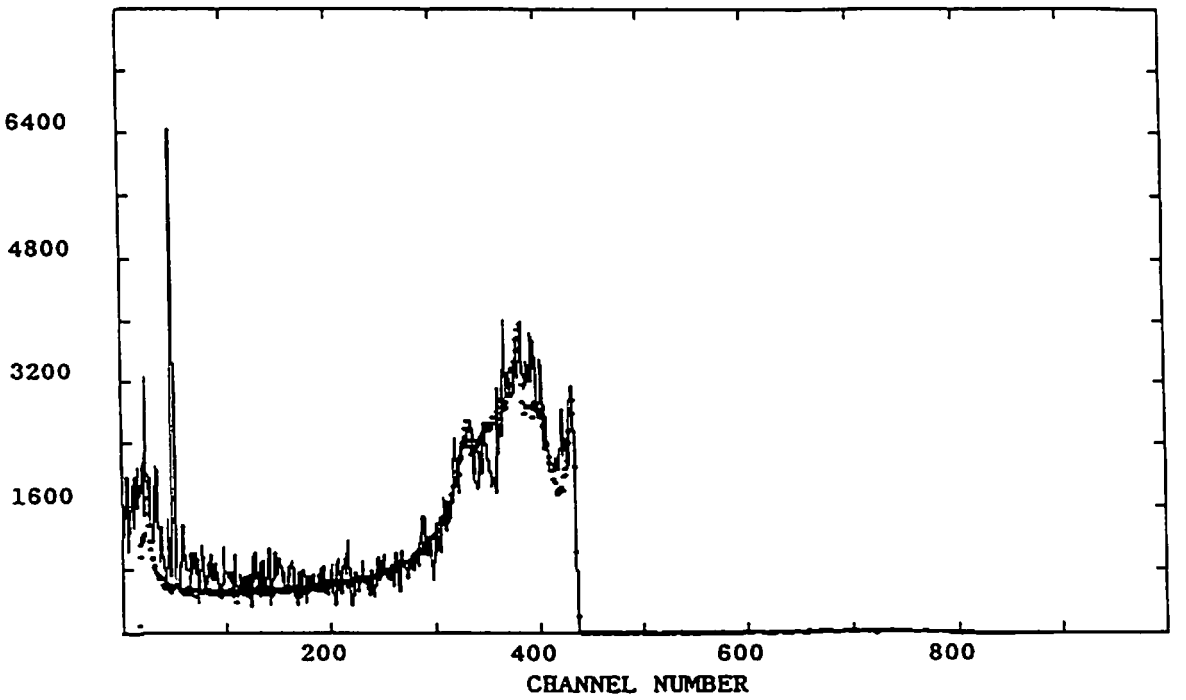

Fig.5 Comparison of measured and calculated pulse height spectra for a Ge detector to 4.37 MeV quasi-monoenergetic photons

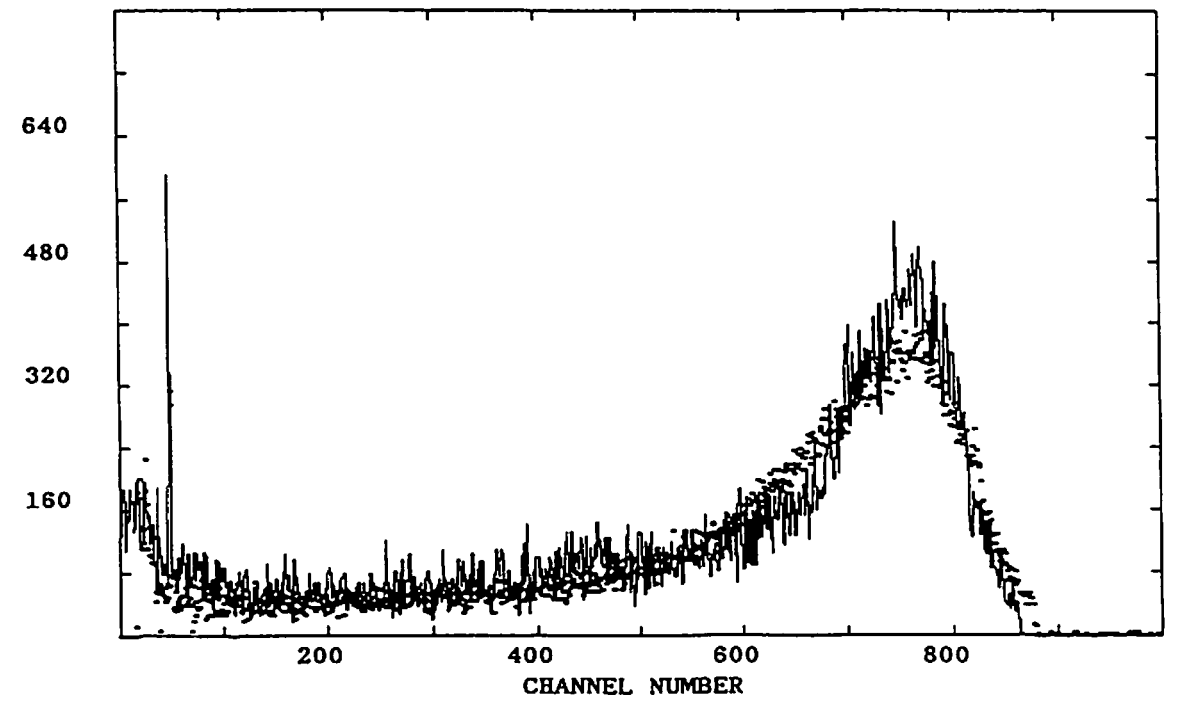

Fig.6 Comparison of measured and calculated pulse height spectra for a Ge detector to 8.85 MeV quasi-monoenergetic photons

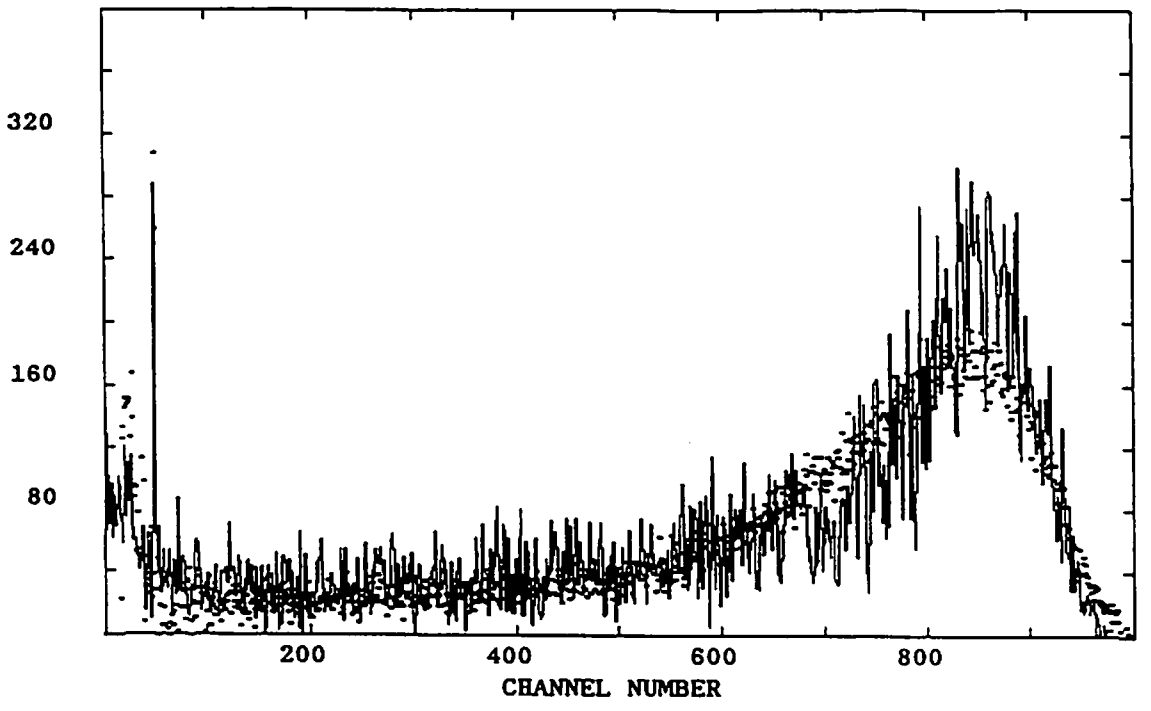

Fig.7 Comparison of measured and calculated pulse height spectra for a Ge detector to 9.95 MeV quasi-monoenergetic photons

APPLICATION OF EGS4 MONTE CARLO CODE TO DESIGN OF COMPTON SUPPRESSION SYSTEM

A. NUNOKO, H. SHINTANI, M. YAMADA and R. MURAKAMI

Nuclear Engineering Ltd.
1-3-7, Tosabori Nishi-ku, Osaka 550, JAPAN

R. TANIGUCHI and T. ASANO

Research Institute for Advanced Science and Technology,
Osaka Prefecture University
1-2, Gakuencho, Sakai-shi,Osaka 593, JAPAN

Abstract

We have been developing a new system for continuous measurement of the concentration of ^{131}I which exists in primary coolant at a nuclear power plant. As the experimental and simulated values showed good agreement a for the unique device with Compton suppression system , the effectiveness of EGS4[1] code for spectrum analysis with use of such device has been proven. As a result, we have decided to use EGS4 Monte Carlo simulation code to the design development of this system.

1. Introduction

At present, ^{131}I in primary water is chemically separated from other elements for measurement of its concentration. As it takes much time and labor, there has been strong demand to develop an automated system for monitoring iodine activity in the primary coolant. Thus, the on-line monitoring system for trace of ^{131}I photo-peak is under development. γ-ray spectrum analysis for RCS piping only with use of Ge detector will be significantly disturbed by the high level counts of Compton continuum region, so that it is difficult to measure the small photo-peak which exists in the Compton continuum region. For the photo-peak measurement in such a case, Compton suppression method is employed.

However, when developing a design of the measurement system for trace of nuclides in RCS piping where other intensive nuclides exist, the conventional design method will not result in satisfactory on-line monitoring system.

Therefore, we have investigated an applicability of EGS4 code to new design of the system which employs the Compton suppression system, by comparing between experimental and simulated values.

2. Experimental device

A Compton suppression system of Research Institute for Advanced Science and Technology, Osaka Prefecture University was used for measurement.

Figure 1 shows the structure of the detector element of the system which was used for the experiment. Ge detector of ϕ 52.8 mm $\times$ 52.7 mm was used as the core detector, while BGO crystal of 50 mm front depth and 55 mm side depth was used as a guard detector ((A) in the figure 1). BGO crystal consists of 8 sub-crystals, each of which photomultiplier is connected with. BGO crystals divided into 2 pieces were also used as a back catcher detector ((B) in the figure 1).

A collimator of ϕ 20 mm $\times$ 150 mm was installed in front of BGO incident window. Experiment was carried out with use of a standard ^{137}Cs point source.

3. Optimization of history numbers

As EGS4 is analog Monte Carlo code, the computational accuracy depends on the number of histories. As the history number gets larger, the more accurate result with less Monte Carlo errors can be obtained, though computing time is increased. Therefore, we have investigated to obtain a minimum number of histories, while maintaining the computing accuracy.

Figure 2 shows the statistical dispersion for a certain value of ^{131}I photo-peak. The result was obtained through computation by varying only the seed value of random numbers (IXXST) at the specific number of histories. The vertical line indicates the relative value taking 107 as 1. At 104 of histories, there is dispersion of about $\pm$ 4 % . The dispersion was decreased to about $\pm$ 1 % at 105 histories. Therefore, it was shown that 105 histories were enough for simulation of the photo-peak.

Figure 3 shows the statistical dispersion for a certain value at the Compton continuum region. The figure indicates a larger dispersion compared with figure 2. Therefore, as much as 106 histories are required for the simulation instead of 105 for the photo-peak.

4. Results

Figure 4 shows a simplified model for simulating the computation of responses by the Compton suppression system with use of EGS4. For simulation, 662 keV photon was used as incident source.

This system utilizes anticoincidence measurement method. To simulate the measure-

ment method, we have prepared the user code such that the logic will trace the cascade of photon inside the substance not allowing counting when energy is deposited both the Ge detector and BGO detector. The simulated value was normalized with the experimental value at 662 keV photo-peak and then both values were relatively compared at the Compton region.

Figure 5 indicates the simulated value obtained with simplified model and experimental value. The experimental value shows the spectrum measured for 3000 seconds with use of 137Cs standard point source. The experimental value and simulated value were normalized at the photo-peak.

Comparing both values, the simulation value obtained with EGS4 was about 0.03 in the energy range of 500 to 600 keV and about 0.07, of 300 to 400 keV in normalizing the experimental value as 1. For the simplified model, simulated continuous spectrum due to Compton scattering largely deviates from the experimental value, and thus it is shown that responses are not well simulated.

This is because the interaction between scattering γ-ray and the guard detector is not well simulated. It was shown that the calculation by the simplified model did not represent the structural feature around the Ge detector.

Therefore, a detailed model was constructed so that the environment of EGS4 becomes similar to the detector. For the detailed model, considerations were given to the Ge detector casing, Be window, clearance between detectors, crystal electrode and dead layer.

Figure 6 indicates the simulated value obtained with the detailed model and experimental value. By comparison with their obtained with the simplified model, the simulated value showed significant improvement; the value obtained with EGS4 is about 1.2 in the energy range of 500 to 600 keV and about 1.7, of 300 to 400 keV. The result showed that EGS4 was applicable to the evaluation of scattering photon performed by the Compton suppression system, modeling in detail an important region of the computation model.

5. Conclusion

It was shown that EGS4 code was applicable to the spectrum analysis with use of the Compton suppression system. Therefore, it is planing to make use of this computational code for a design of the on-line monitoring system for trace of ^{131}I which exists in RCS piping at a nuclear power plant.

References

[1] W. R. Nelson, H. Hirayama and D. W. O. Rogers, *The EGS4 Code System*, SLAC-Report-265,1985.

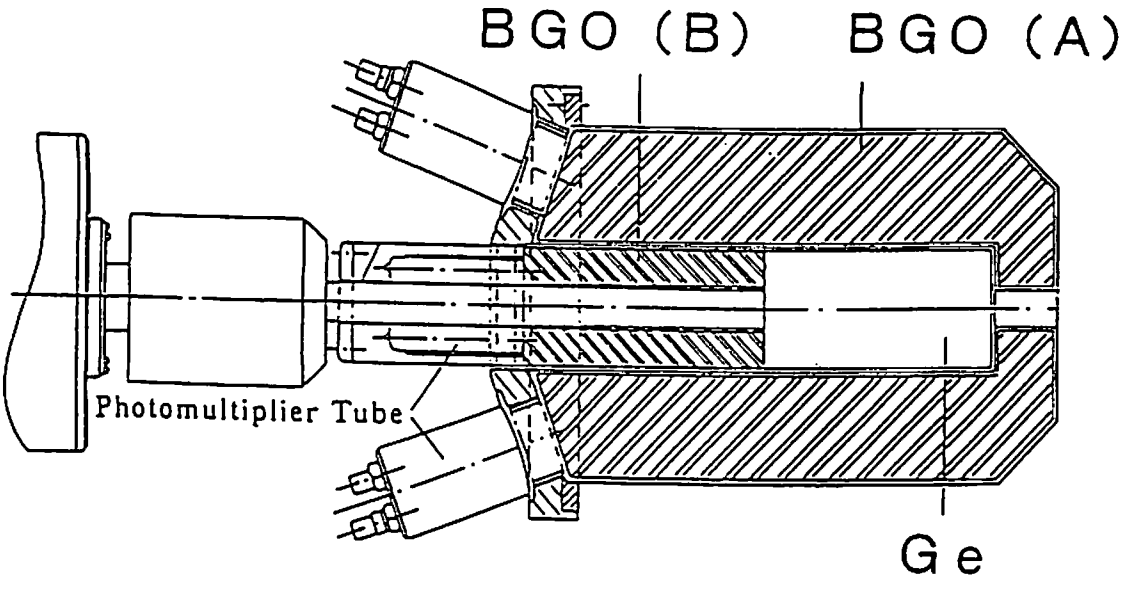

Fig.1 Cross-Sectional View of Detector of Compton Suppression System

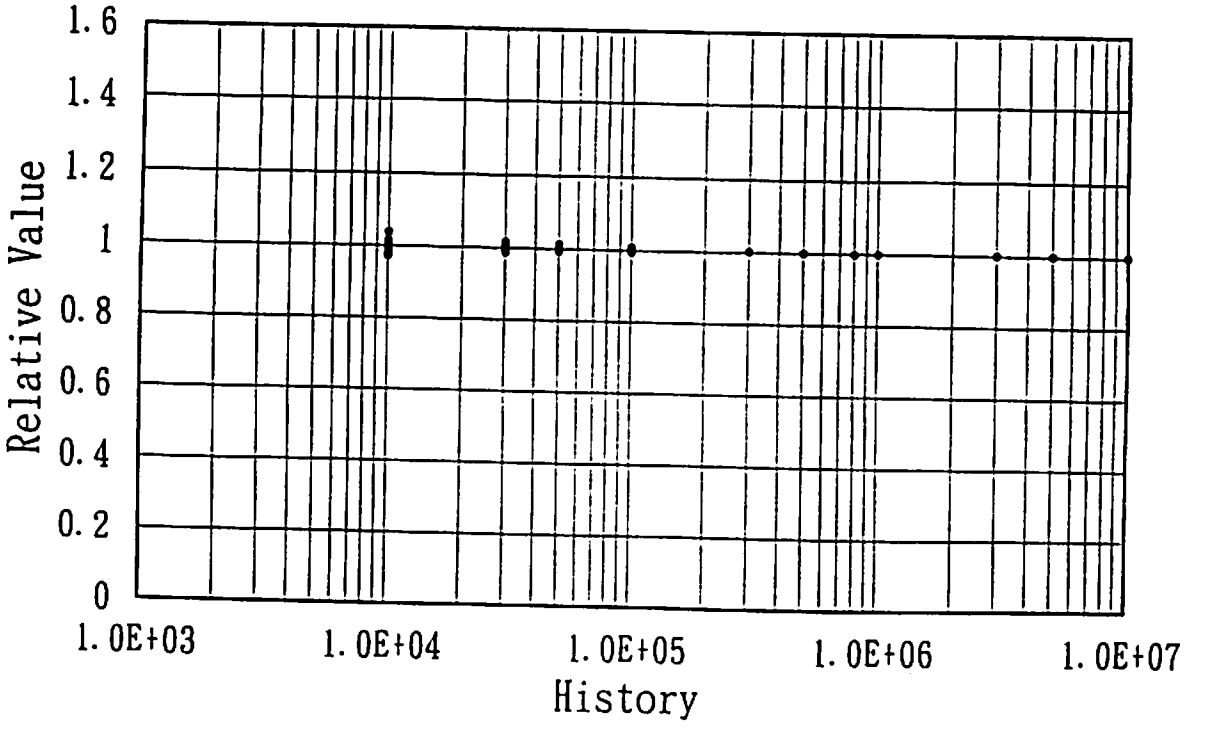

Fig.2 The Optimum Number of Histories (Photo-Peak)

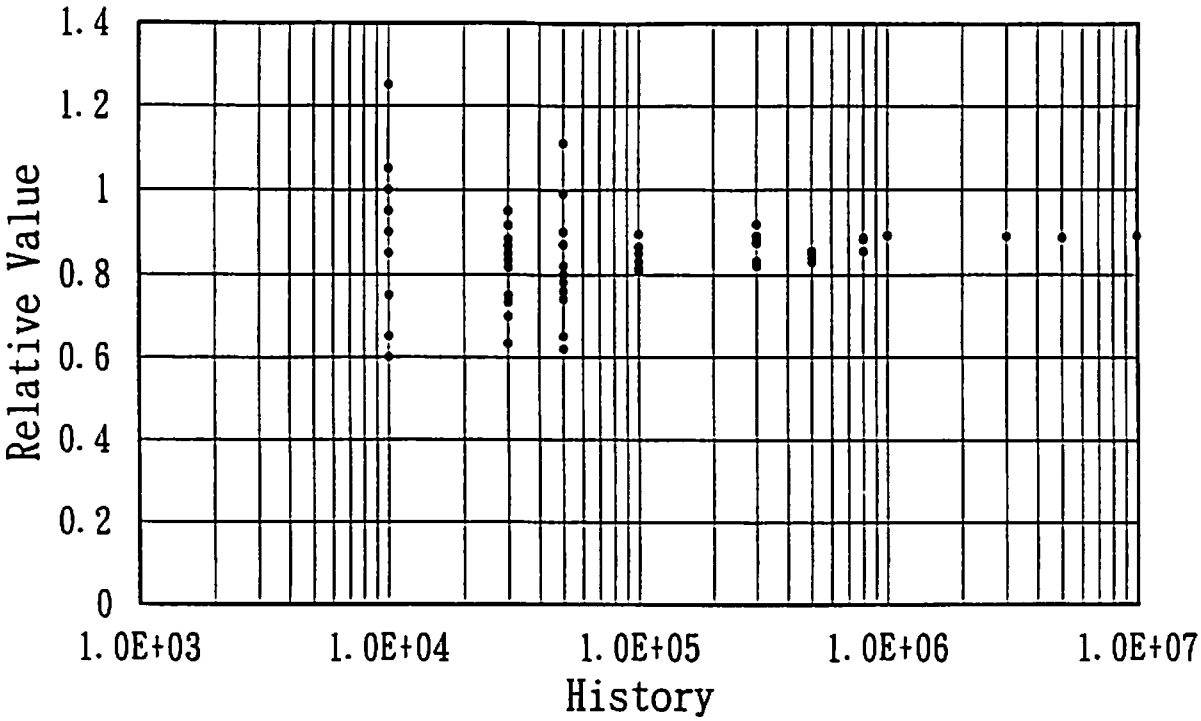

Fig.3 The Optimum Number of Histories (Compton Region)

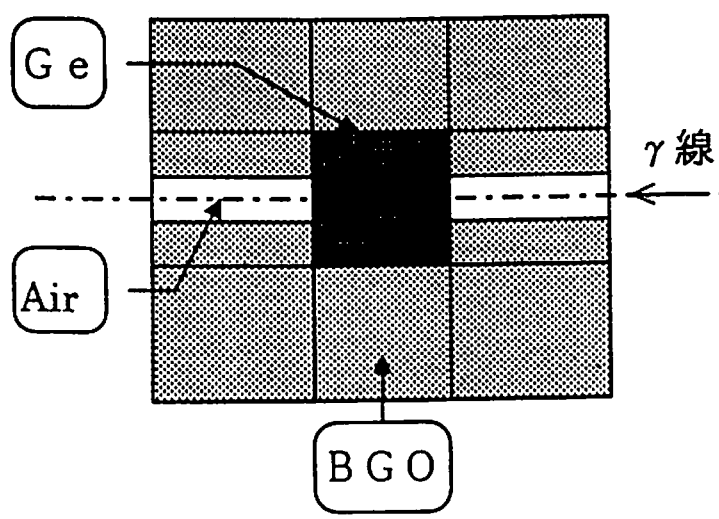

Fig.4 Compton Suppression System Simple Model

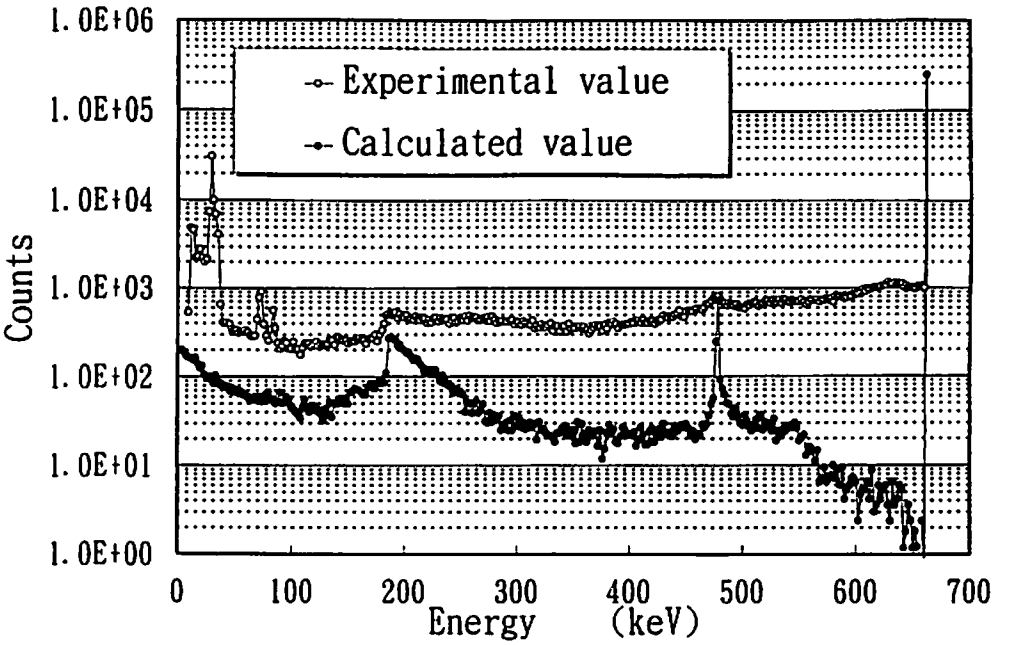

Fig.5 Comparison for Compton Region of Compton Suppression System Simple Model

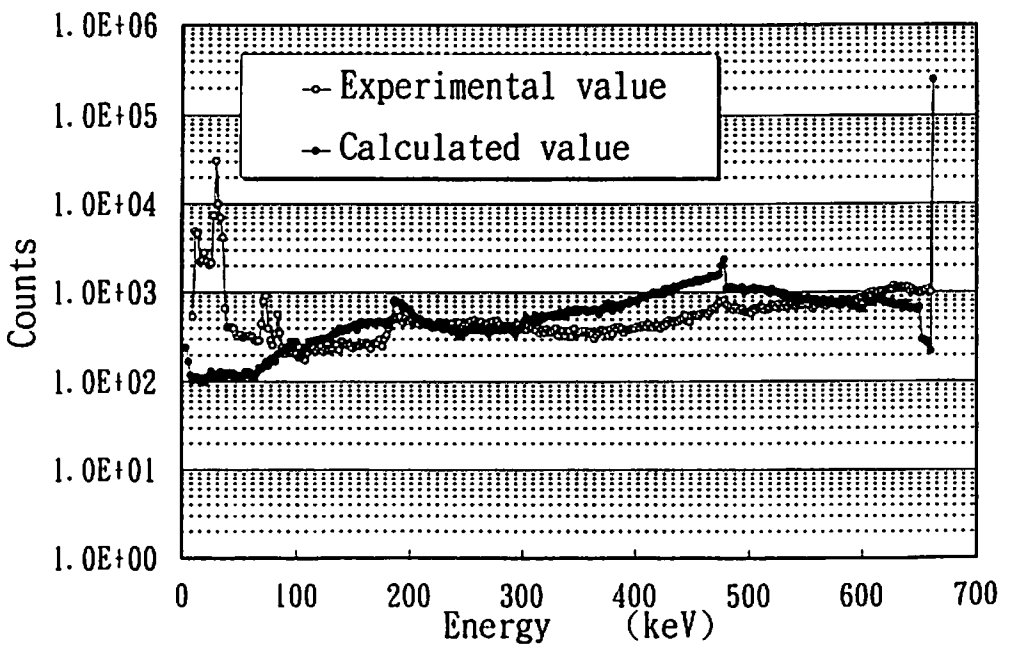

Fig.6 Comparison for Compton Region of Compton Suppression System Detailed Model

CALCULATION OF CdTe SEMICONDUCTOR DETECTOR RESPONSE

H. NISHIZAWA, K. IKEGAMI, K. TAKASHIMA and T. USAMI

Mitsubishi Electric Corporation
8-1-1, Tsukaguchi-Honmachi, Amagasaki, Hyogo 661, Japan

T. YAMAMOTO

Radioisotope Research Center, Osaka University
2-4, Yamadaoka, Suita, Osaka 565, Japan

Abstract

Calculations of the detector response normally assume that the energy absorption of the sensor part is proportional to the output pulse height. However, the response of a semiconductor detector whose charge carrier mobility is as small as that of CdTe can not be simulated because the output pulse height is not proportional to the absorbed energy of the sensor part. In the EGS4 calculation, the response of the CdTe semiconductor detector can be simulated by multiplying the value of the absorbed energy by the weight function, which takes into account the mean free path of the charge carriers and the interaction position. The calculated results agree well with the results of the experiment and indicated that the simulation model is valid.

1. Introduction

Cadmium Telluride (CdTe) semiconductor detectors are very suitable for use at room temperature without liquid nitrogen because of its sufficient band gap energy (1.47eV). In addition, their atomic numbers are so large (48 and 52) that their photon detection efficiency is better than that of Si or Ge. Recently CdTe crystals have become readily available because of improvements in the crystal growth method[1] and hence the CdTe detectors will be used well. However, the CdTe detector has disadvantages in that the mobility of charge carriers in CdTe is much smaller than in Si and Ge. This means that the drifting charge carriers are easily trapped in the CdTe crystal. If the drifting charge carriers can not reach the collecting electrodes, the output pulse height will be smaller than that in the case of perfect charge collection. Therefore it is difficult for CdTe detector to

obtain the correct spectra in the high energy regions and hence various methods are tried to improve the energy spectra. For example, we have suggested a multi-layered structure of CdTe elements to increase the sensitivity[2].

When the detector response is simulated, it is normally assumed that the energy absorption of the sensor part will be proportional to the output pulse height. The output pulse height is proportional to the collected charge in actuality, and it is necessary to convert the absorbed energy to the collected charge in order to simulate the detector response. However, the collected charge is not proportional to the absorbed energy in the CdTe detector because of its small carrier mobility. Therefore the detector response of the CdTe detector can not be simulated by only calculating the energy absorption, since the output pulse height is not proportional to the absorbed energy of the sensor. In this paper, the response of the CdTe detector is calculated by taking into account the hole trapping phenomena.

2. Simulation Method

2.1 CdTe detector

For the planar type detector, the collected charge Q(t) on the electrode is proportional to the sum of the drifting distance of the electron and that of the hole as follows,[3]

$$Q(t) = \frac{q_0}{d}[\text{drifting distance of electron} + \text{drifting distance of hole}] \qquad (1)$$

where d is the thickness of the detector, and t is the time from the creation of the charge carriers q_0 through photon interaction. Figure 1 shows the pulse shape Q(t) in relation to the interaction position. For example, at interaction position 1, the collecting time of the holes is shorter than that of the electrons since the position is very close to the cathode. On the other hand, at interaction position 3, the collecting time of the holes is much longer than that of the electrons since the position is very far from the cathode. The rise time of pulse is dependent on the interaction position because the drifting velocity of the charge carrier, which is proportional to its mobility, differs greatly between the electron and the hole in the case of the CdTe detector. Also, some holes drifting in the CdTe detector are trapped in the trapping center because of the insufficient purity of the crystal. If the hole trapping phenomena occurs, the output pulse height becomes small as shown in Fig.2. This is because the final drifting distance of the hole is shorter than when no trapping phenomena occurs.

When the incident photon energy is less than a few hundred keV, the CdTe detector has good energy resolution and high efficiency at the full energy peak because photon interaction occurs so near to the detector surface that there is little hole trapping. The typical energy spectrum of ^{241}Am in a CdTe detector is shown in Fig.3-1. In this figure, the

photo peak at 59.5keV can be seen clearly. When the incident photon energy is over a few hundred keV and photon interaction occurs at random positions in the detector, the charge collection efficiency becomes low because of the hole trapping phenomena. Therefore the efficiency at the full energy peak becomes much worse, and it is very difficult to distinguish the full energy peak above 1 MeV. The typical energy spectrum of ^{137}Cs in a CdTe detector is shown in Fig.3-2. The count rate at the full energy peak at 662keV is very low, the tail part appears below 662keV peak, and the shape of the Compton continuum is not correct. Therefore correct spectroscopy with CdTe semiconductor detectors is very difficult in the high energy region above a few hundred keV.

2.2 Hole trapping phenomena

The mean free path λ of charge carriers, that is, electrons and holes, in semiconductor detectors is estimated as

$$\lambda = \mu\tau F \tag{2}$$

where μ, τ and F are the mobility, the mean lifetime and the electric field respectively. As an example, the typical value of mobility-lifetime product $\mu\tau$ for a hole is $5 \times 10^{-5} cm^2/V$. When the electric field F is 500 V/cm, the mean free path λ of holes in the CdTe detector can be estimated to be 0.25 mm. Because the thickness of the typical CdTe detector is 1 or 2 mm, the thickness of the detector is longer than the mean free path of holes and most holes drifting in the CdTe detector are trapped and can not reach the collecting electrode. The output pulse height is proportional to the collected charge on the electrodes and the collected charge depends on the sum of the drifting distances of the electron and hole. Figure 4 shows the average collected charge dependent on the interaction position, where q_0, x and d are the amount of created charge, the distance from the collection electrode and the detector thickness, respectively. When the distance from the interaction position to the collected electrode is longer than λ, the collected charge decreases because of the charge carrier trapping, especially hole trapping, in the CdTe detector. In this simulation, the distance from the interaction position to the carrier trapping position is assumed to be λ, although in actuality the drifting distance of the carrier has a distribution.

The response function of the CdTe detector was predicted with a simulation using the Monte-Carlo calculation code, EGS4 (Electron Gamma Shower Version 4)[4]. It is standard practice to calculate the amount of energy absorption in the detector when the detector response is simulated. If the charge carriers drifting in the semiconductor detector are trapped and can not reach the collecting electrode, the output pulse height will be dependent on the sum of the drifting distance of the charge carriers. In this simulation the charge carrier trapping in the CdTe detector must be considered as follows.

In the case of the planar type detector, the collected charge $Q(t)$ on the electrode is

presented as in equation (1). In Fig. 5, the charge carriers are created at the interaction position and the distance from this point to the cathode is indicated by x.

If the mean free path of electron and hole are λ_e and λ_h respectively, there are four cases of the average collected charge $Q(x)$, and $Q(x)$ becomes a function of x.

[1] In the case where $\lambda_e > d$ and $\lambda_h > d$,

$$Q(x) = q_0 \tag{3}$$

[2] In the case where $\lambda_e > d$ and $\lambda_h < d$,

$$Q(X) = q_0 \left[\frac{d-x}{d} + \frac{\lambda_h}{d}\right] \tag{4}$$

[3] In the case where $\lambda_e < d$ and $\lambda_h > d$,

$$Q(X) = q_0 \left[\frac{\lambda_e}{d} + \frac{x}{d}\right] \tag{5}$$

[4] In the case where $\lambda_e < d$ and $\lambda_h < d$,

$$Q(X) = q_0 \left[\frac{\lambda_e}{d} + \frac{\lambda_h}{d}\right] \tag{6}$$

The energy deposition in the CdTe detector calculated by EGS4 is multiplied by the weight functions, which are defined in the brackets of equations (3) to (6). Therefore, except for case [1], the energy multiplied by the weight function is less than the energy when the charge carrier trapping is not considered. In this way, the hole trapping phenomena can be allowed for by multiplying the value of the energy deposition by the weight function which is an improvement on the energy deposition calculation in the subroutine AUSGAB. The detector response can be simulated by taking into account the charge carrier trapping in the CdTe detector with this simple method.[5]

The calculation carried out according to this method were compared with the results of the experiment. The shape of the CdTe detector was that of a 2x2x2mm^3 cube. In the EGS4 calculation, incident g-rays cross the cathode surface vertically and evenly as shown in Fig. 6 and the particles which have once gone out of the element are not taken into account. The energy of incident g-rays was 662keV (^{137}Cs), 1.17MeV and 1.33MeV (^{60}Co). The cut off energy of the electron and the photon are 10keV and 1keV, respectively.

3. Experiment

A block diagram of the experiment is shown in Fig. 7. The shape of the CdTe element which was located in the aluminum housing case was also that of a 2x2x2mm^3 cube as shown in Fig. 6. ^{137}Cs and ^{60}Co check sources were used and the distance between the detector and the source was kept long enough so that the γ-rays were parallel and the

dose rate errors at the detector were small. The bias voltage of 100V was applied and the shaping time constant of the amplifier was 2 μsec. The pulse height distribution of the CdTe detector was measured with the multi-channel-analyzer.

4. Results and Discussion

The calculated results for ^{137}Cs and ^{60}Co are compared with the results of the experiment by normalizing the number of incident γ-ray to the detector in the case of the calculation and the experiment as shown in Fig. 8-1 and 8-2, respectively. In Fig. 8-1, the tail part appeared at the energy region below the 662keV peak and the count rate of the low energy region of the Compton continuum became high in the experiment. In Fig. 8-2, the full energy peaks at 1.17 and 1.33MeV were difficult to distinguish and the shapes of the spectra agreed well with the results of the experiment. These results indicate that the simulation model was valid.

If the shapes of the spectra are observed in more detail, the results of the calculations and the experiment are slightly different. It is suspected that this is because the drifting distances of the charge carriers in this calculation are fixed in spite of the fact that the drifting distances have a distribution in actuality.

5. Conclusion

The response of a semiconductor detector with a charge carrier mobility as small as CdTe can be simulated by means of a simple model that takes into account the mean free path of charge carriers and interaction positions. The calculated results, for example, that the tail part appeared at the energy region below the peak, agree well with the the results of the experiment and indicate that the simulation model is valid. We will make an enhanced model that can take into account carrier behavior more exactly in order to simulate the detector response with high precision.

References

[1] Y. Iwase, R. Ohno, et. al., Mat. Res. Soc. Symp. Proc. **Vol.302**, 225-230 (1993).

[2] K. Ikegami, H. Nishizawa, et. al., Radiation Protection Dosimetry, Nuclear Technology Publishing, **Vol.66**, Nos.1-4, pp.455-458 (1996).

[3] G. F. Knoll, Radiation Detection and Measurement Second Edition, The Nikkan Kougyou Simbun Ltd. pp.430-434 (1991). [in Japanese]

[4] W. R. Nelson, H. Hirayama and D. W. O. Rogers, The EGS4 Code System, SLAC-265 (1985).

[5] H. Nishizawa, K. Ikegami, et. al., KEK Proceeding 96-4, Radiation Detectors and Their Uses, 230-239 (1996).

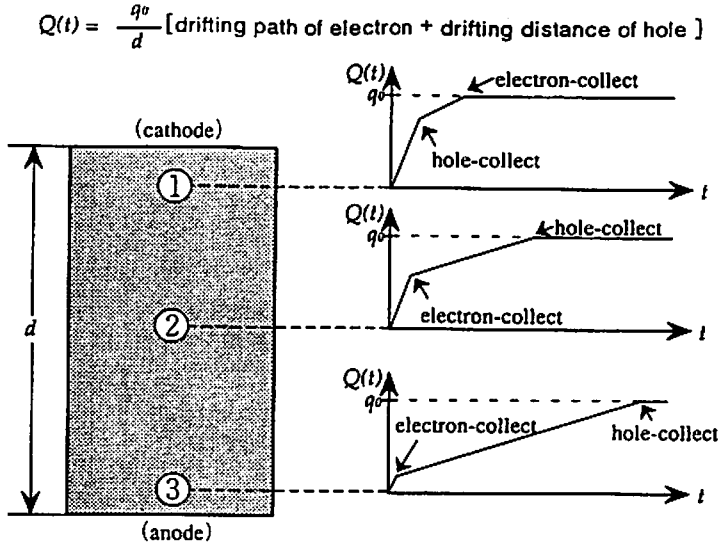

Fig.1 Pulse shape in relation to the interaction position (planar type detector).

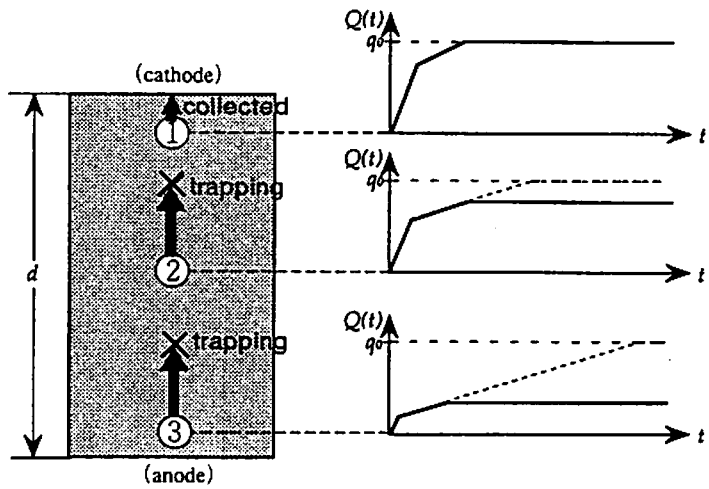

Fig.2 Pulse height defects caused by the hole trapping phenomena.

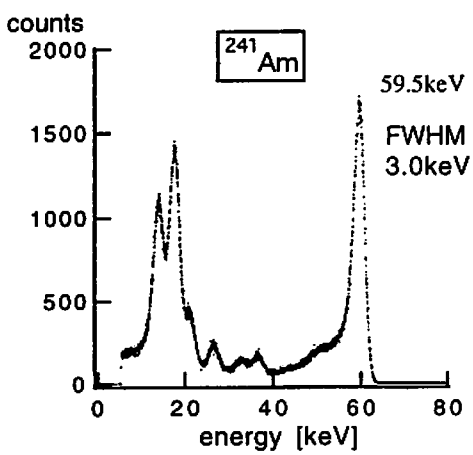

Fig.3-1 Typical CdTe spectrum (^{241}Am).

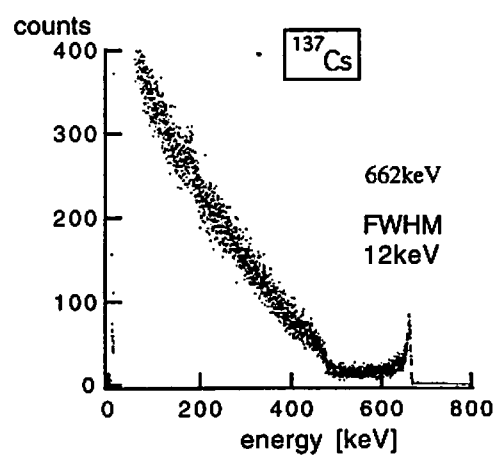

Fig.3-2 Typical CdTe spectrum (^{137}Cs).

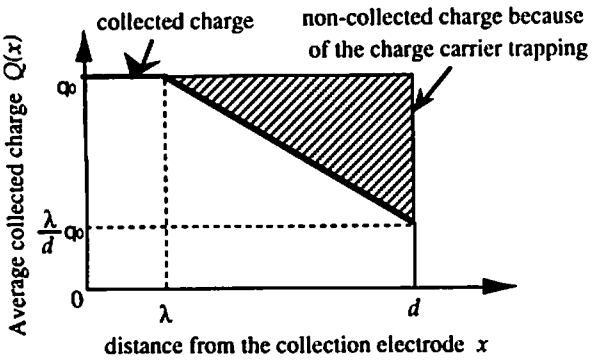

Fig.4 Average collected charge in relation to the interaction position.

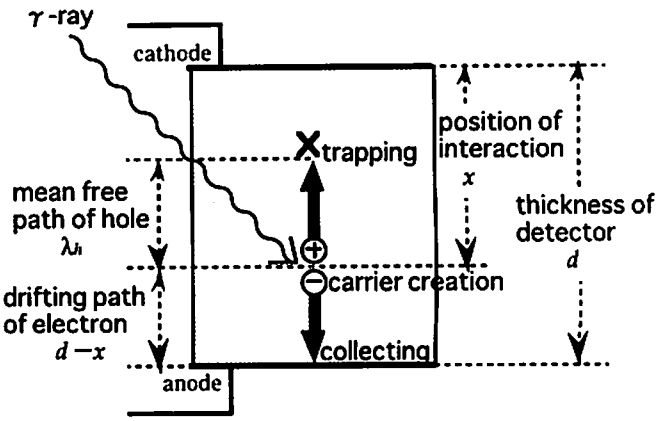

Fig.5 Hole trapping phenomena in the CdTe detector.

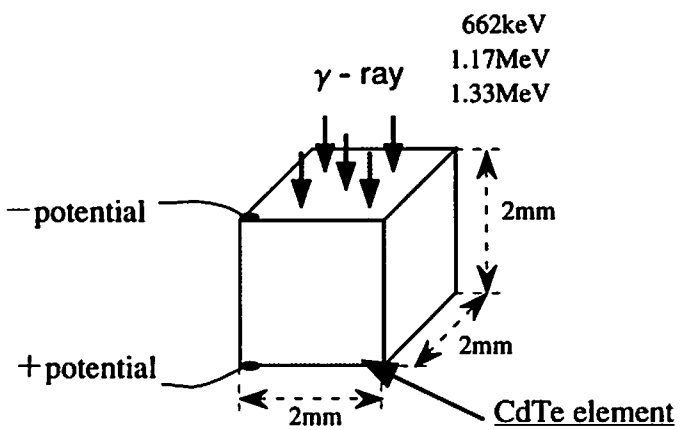

Fig.6 Model for calculations related to the CdTe detector.

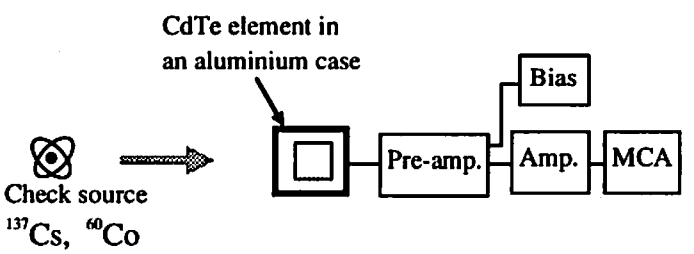

Fig.7 Block diagram of the experiment.

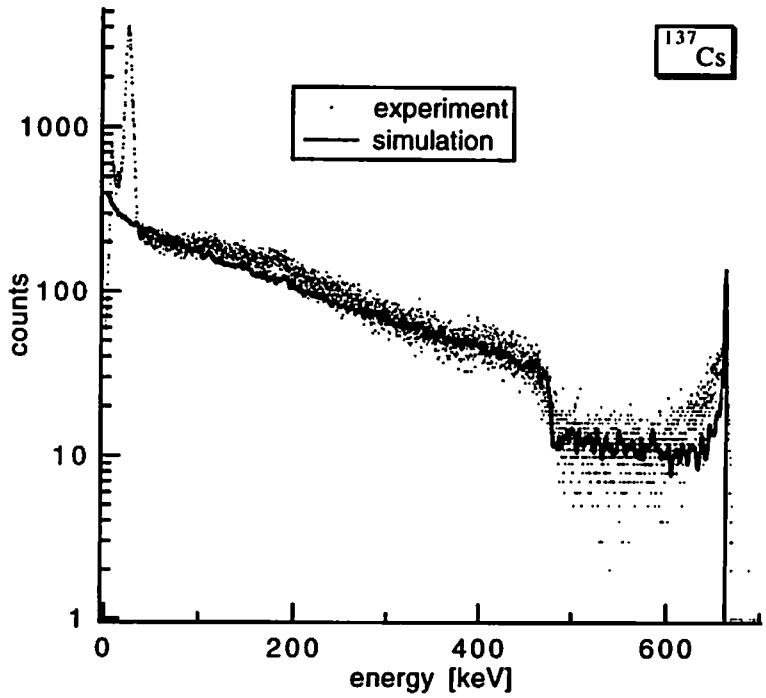

Fig.8-1 Results of the simulation compared with the results of the experiment (^{137}Cs).

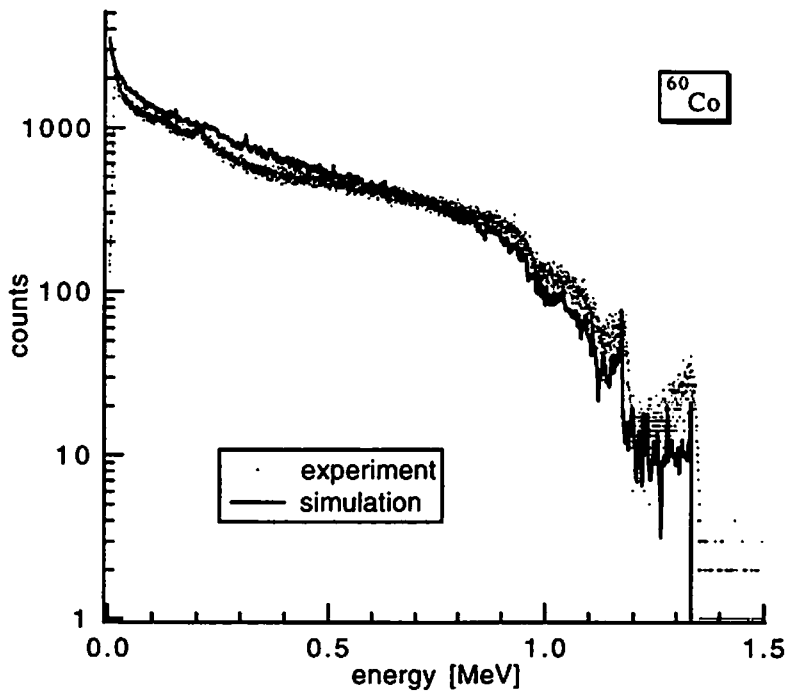

Fig.8-2 Results of the simulation compared with the results of the experiment (^{60}Co).

CALCULATIONS OF WALL EFFECT IN PROPORTIONAL COUNTER FOR ABSOLUTE RADIOACTIVITY MEASUREMENTS OF GASEOUS RADIOISOTOPES

Y. WU and C. MORI

School of Engineering, Nagoya University
Nagoya 464-01, Japan

1. Introduction

For absolute radioactivity measurement of gaseous samples, two new methods, known as "diffusion-in a long proportional counter method" and "position-sensitive proportional counter method"[1,3], were developed to eliminate the end effect[1,2] of proportional counter and a high precision of the measurement were obtained. However the wall effect also affects the measurement in addition to the end effect. It is because that for the sample gas near the wall of proportional counter some beta-rays lose little energy in the counting gas and dissipate most of the energy in the wall of the counter, so that their pulse heights become very small. On the other hand, in order to eliminate electronic noise, pulse discrimination level must be set in this system. Thus, if the pulse height is below the pulse discrimination level, the pulse will not be counted, which is called wall effect.

Wall effect can be measured with pressure extrapolation method[3]. But, this measurement needs an energy calibration source which emits very low monoenergetic radiation, for example ^{37}Ar emitting 220eV L-Auger electrons. This kind of source is not easy to obtain in general, so that it is important to evaluate wall effect by calculation. Thus, EGS4 code is employed to calculate wall effect in this paper and the calculated results are compared with experimental results. The limits of EGS4 code for the evaluation of wall effect by the calculation are also discussed.

2. Experimental apparatus and calculation method

The apparatus of proportional counter system is shown in Fig.1. It is a cylinder shape counter with 1m in length, 4cm in internal diameter and 0.5cm in wall thickness. Pulse discrimination level is set at 220eV in this system using 37Ar L Auger electrons .

Wall effect is calculated with EGS4 code as follows: First is to model the proportional

counter. The sample gas is uniformly mixed up with counting gas. Then, under the energy spectrum of beta-rays emitted from the sample gas, the position, direction and energy of each beta-ray can be decide by random number. Second is to follow the tracks of beta-rays and to calculate the energy loss in the counting gas. If the energy loss of a beta-ray in the gas is below the pulse discrimination level, the beta-ray can not be counted. In this way the lost counts due to wall effect can be evaluated.

3. Results and discussions

In the calculation of wall effect it is important to calculate energy loss within a thin gas layer near the wall of counter. Figure 2 shows the spectra of energy loss within a plane layer of P-10 counting gas with 3mm thickness where 1000 beta-rays with monoenergy(1MeV) are vertically incident on. Most of the beta-rays lost without counting due to the wall effect are those emitted in the area within 3mm from the wall of counter. The energy loss in this gas layer is mostly continuous energy loss, and the effects of scattering and discrete events yielding delta-rays are very little in the calculation. But, with raising the values of the lowest cutoff energies AE and AP[1], the calculated values of continuous energy loss became large.

In order to confirm the validity of the calculated results of energy loss in the gas layer, the specific energy loss in a very thin gas layer with a thickness of 0.1mm is calculated as shown in Fig.3. When AE and AP is large, the calculated results of energy loss became large and for beta-rays with lower energy the difference between calculated results and the results of a reference paper[4] evidently become large. For an imaginative spectrum of evenly distributed incident energy, wall effects are calculated in each energy and are shown in Fig.4. When incident energy is below ECUT and PCUT[2], wall effect can not be well calculated. For this sake, in the calculation of wall effect it is better to set AE and ECUT at a lower value.

Because EGS4 code is not so suited for the calculation when energy is lower than 20keV as shown in Fig.3, the count loss by wall effect for low energy is evaluated. For beta-ray spectrum of ^{41}Ar, the count loss by wall effect is calculated at each energy with 41Ar sample gas and P-10 counting gas at 0.5×10^5 Pa when AE=511.2keV and AP=0.2keV as shown in Fig.5. The rate of count loss given by those beta-rays with energy below 20keV is only 0.4 %. Thus, for ^{41}Ar the effect of calculation error given by low energy can be neglected.

[1]AE is the lowest cutoff energy of secondary electrons created in an inelastic collision and AP is the lowest cutoff energy of bremsstrahlung photons created in a discrete event.

[2]ECUT is the total electron energy below which all energy is considered to be deposited locally and the particle history is terminated. PCUT is the photon energy below which all energy is considered to be deposited locally and the particle history is terminated.

Because the count loss by wall effect decrease with increasing pressure of counting gas, for the same sample gas the relative count rate decrease with reciprocal pressure. Figure 6 shows this variance of relative count rate with counting gas. As shown in Fig.6, calculated results of wall effect of 41Ar agreed well with experimental results when AE=511.2keV and AP=0.2keV. When AE and AP is set at a larger value, calculated results of count loss become smaller than the experimental results.

Because the beta-rays lost by wall effect leave very short track in counting gas, even changing ESTEPE[3] by large degree, it brings little effect to the calculated results of wall effect as shown in Fig.7. For 14C, count loss by wall effect is calculated at each energy and shown in Fig.8. Because the energy of beta-rays emitted from ^{14}C is low, the rate of count loss given by those beta-rays with energy below 20keV is 12%. The calculated results and experimental results of wall effect are shown in Fig.9. error bar for calculated results in Fig.9 means the rate of count loss given by those beta-rays with energy under 20keV. EGS4 code can be used to ^{14}C for calculation of wall effect. For those samples which emit beta-rays with lower energy than ^{14}C, EGS4 code becomes rather difficult to be applied.

4. Conclusions

Count loss by wall effect was calculated with EGS4 code. Calculated results agreed well with experimental results measured with pressure extrapolation method. In this calculation AE, AP and ECUT, PCUT are better to be set at lower values. Because EGS4 code is not so suited for very low energy of beta-ray, for those samples which emit beta-rays with lower energy than 14C, EGS4 is unsuited to be used for calculation of wall effect.

References

[1] Y. Wu, C. Mori, A. Uritani, K. Yanagida, H. Miyahara, T. Aoyama and M. Yoshida, Nucl. Instrum. Meth. **A343**, (1994) 539.

[2] W. B. Mann, H. H. Seliger, W. F. Marlow and R. W. Medlock, Rev. Sci. Instr., **31**, (1960) 690.

[3] M. Yoshida, T. Yamamoto, Y. Wu, T. Aratani, A. Uritani and C. Mori, Nucl. Instrum. Meth. **A330**, (1993) 158.

[4] L. Pages, E. Bertel, H. Joffre, and L. Sklavenitis, Atomic Data Tables 4, (1972)1.

[3]ESTEPE is a fixed fractional energy loss per step.

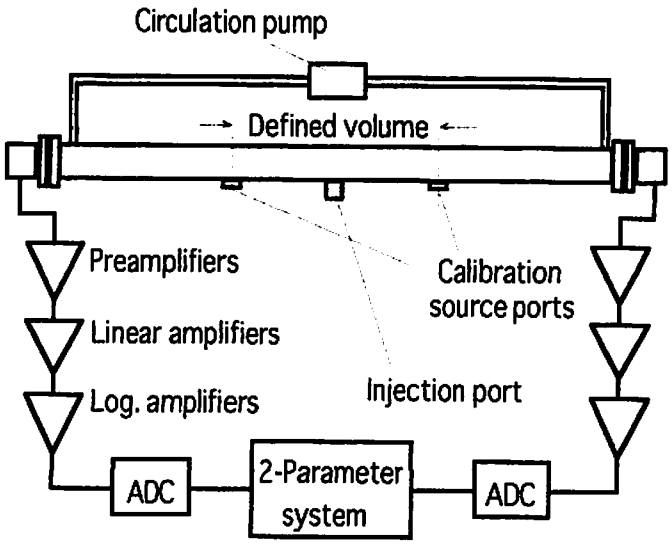

Fig.1 Position-sesitive proportional counter and block diagram of the associated electronics including logarithmic amplifiers.

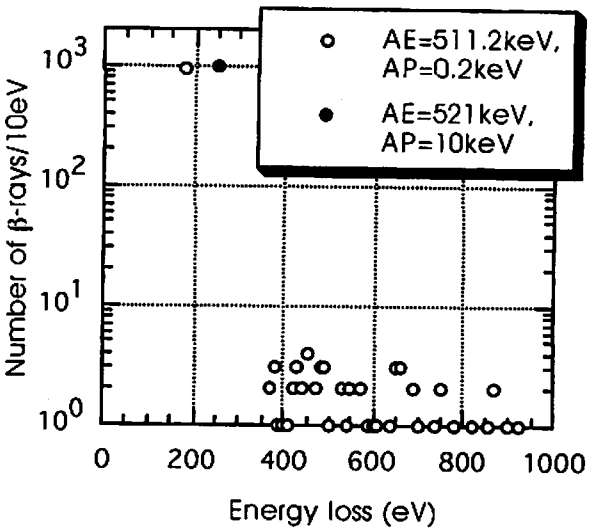

Fig.2 Spectra of energy loss in a plane layer of P-10 gas with 3mm thickness at 0.5x10^5 Pa, where 1000 beta-rays with monoenegy (1MeV) are vertically incident on

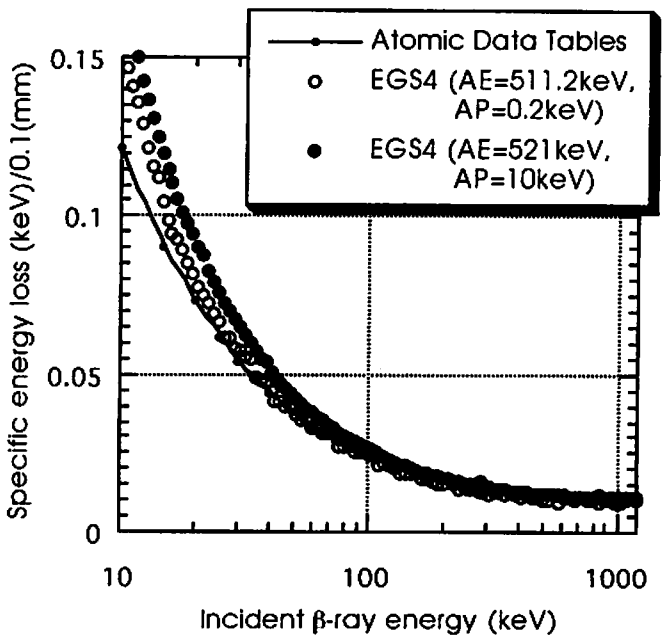

Fig.3 Specific energy loss in an Ar gas plane layer with 0.1mm thickness at 0.5x10^5 Pa

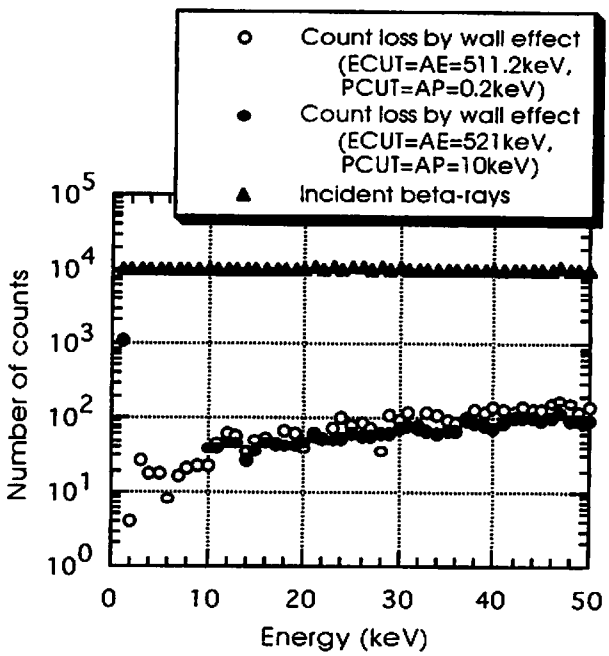

Fig.4 Count loss by wall effect with P-10 gas at 0.5X10^5 Pa

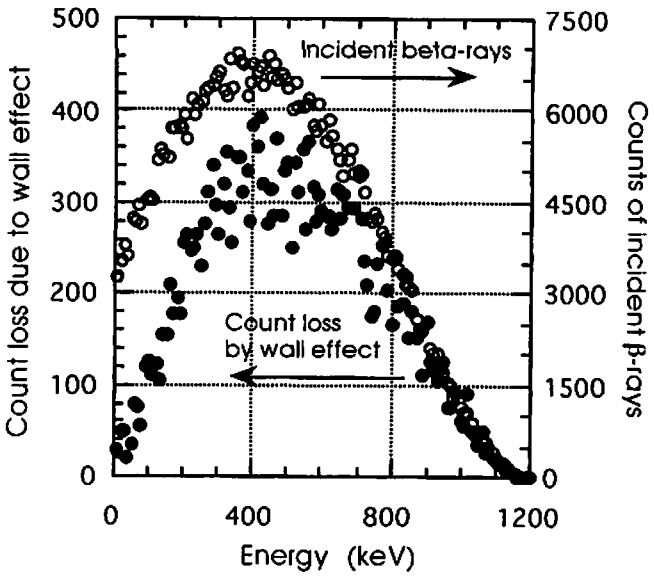

Fig.5 Count loss by wall effect calculated with ^{41}Ar sample gas and P-10 counting gas at $0.5X10^5$ Pa when AE=511.2kev and AP=0.2keV

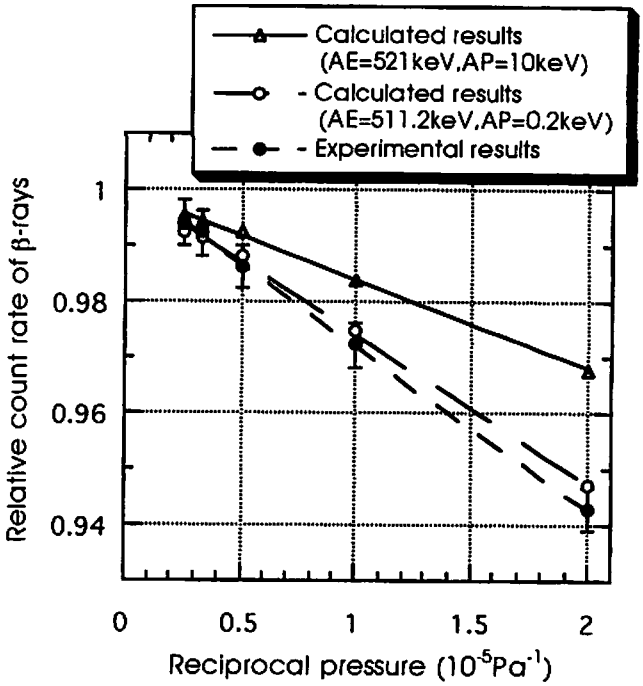

Fig.6 Relative count rate for ^{41}Ar vs. reciprocal of P-10 counting gas pressure for different AE, AP values

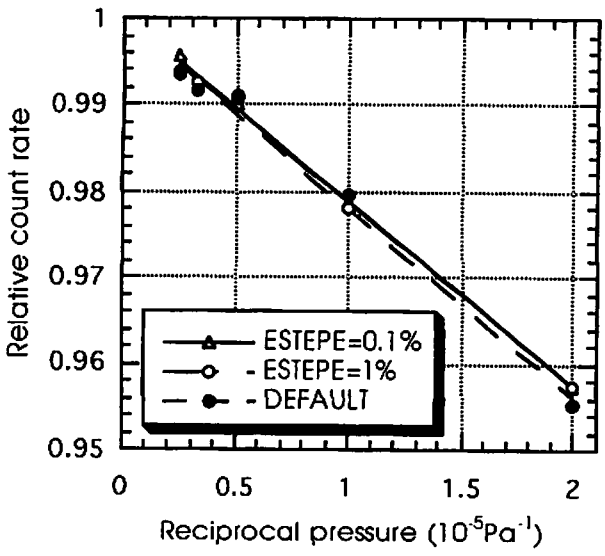

Fig.7 Effect of different ESTEPE values for calculation of wall effect

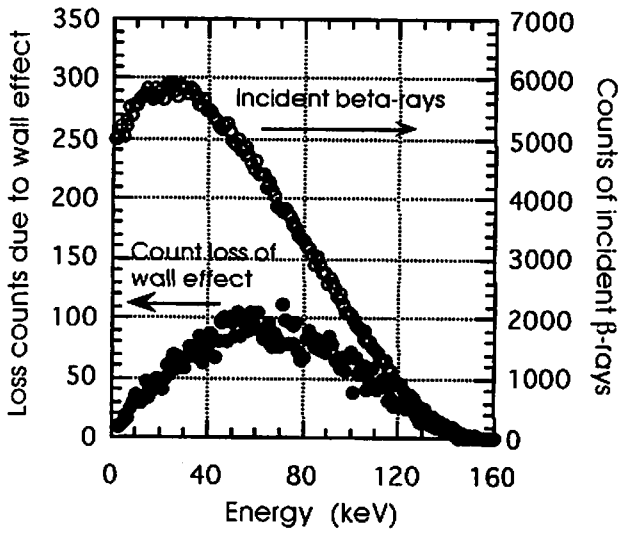

Fig.8 Count loss by wall effect calculated with ^{14}C sample gas and CH_4 counting gas at $0.5X10^5$ Pa when AE=511.2kev and AP=0.2keV

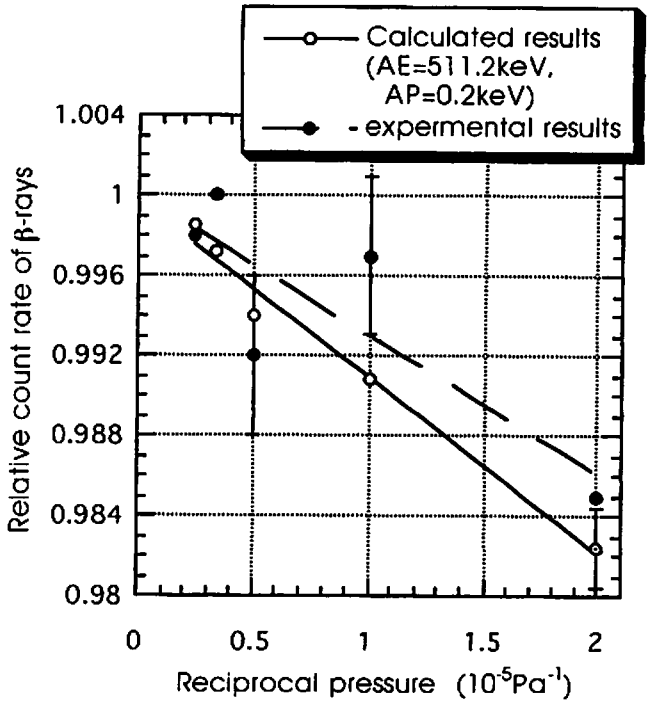

Fig.9 Relative count rate for ^{14}C vs. peciprocal of CH_4 counting gas pressure

ESTIMATION OF S/N RATIOS FOR DOUBLE BETA DECAY EXPERIMENTS WITH DCBA

S. KITAMURA

Tokyo Metoropolitan College of Allied Medical Sciences
Tokyo 116, Japan

N. ISHIHARA, T. OBAMA, S. TAKEDA, and Y. YAMADA

National Laboratory for High Energy Physics
1-1 Oho, Tsukuba-shi, Ibaraki 305 Japan

Abstract

A magnetic tracking detector called DCBA (Drift Chamber Beta-ray Analyzer) is proposed for double deta decay experiments. It will be able to measure the half lives of two-neutrino double beta decay ($2\nu\beta\beta$) and neutrinoless double beta decay ($0\nu\beta\beta$) of ^{150}Nd. The measurable half-life limit of $0\nu\beta\beta$ with DCBA is 4×10^{24}yr with enriched ^{150}Nd, which lower the effective mass limit of Majorana neutrino down to 0.5 - 0.1 eV, depending on the nuclear matrix element. Possible backgrounds caused by γ rays hitting source plates are studied using the EGS4 code and other Monte Carlo codes. In the measurement of $0\nu\beta\beta$ decays, it is important to suppress γ rays of energy between 4-6 MeV in order to reduce backgrounds. The estimation procedure of S/N (signal to background noise) ratios is described.

1. Introduction

The interest in neutrino physics is recently increasing because physics beyond the Standard Model of particle physics can be probed through neurtino experiments. Among them, possibilities of neutrinoless double beta decay include investigation of the neutrino mass, of the parameter space of SUSY models, of right-handed W boson, compositness, leptoquarks, Majorons... [1][2].

Possible Feynman graphs for double beta decays of two-neutrino mode ($2\nu\beta\beta$) and neutrinoless mode ($0\nu\beta\beta$) are shown in Figs.1(a) and 1(b), respectively. The $2\nu\beta\beta$ decay is predicted by the Standard Model. On the other hand, the $0\nu\beta\beta$ decay violates lepton number conservation, and is therefore forbidden in the Standard Model. However $0\nu\beta\beta$ decay is allowed if at least one neutrino is a massive Majorana particle[2][3][4]. Recent experimental results related solar neutrino[5], atmospheric neutrino[6] and neutrino oscillation[7] imply massive neutrino instead of massless neutrino. Present situation of the neutrino mass limit obtained by $0\nu\beta\beta$ decay experiments is shown in Fig.2 together with expectation for the near future until the year 2000[1]. The $0\nu\beta\beta$ decay experiments carried out so far using a calorimeter with ^{76}Ge have set the upper limit of the effective neutrino mass parameter $< m_\nu >$ as 0.65 eV from the half-life lower limit of 5.6×10^{24} yr[8]. A breakthrough into the region of sub-eV requires experiments with both a large source mass and very low background.

A tracking detector DCBA (Drift Chamber Beta-ray Analyzer) is newly proposed to measure momenta of electrons from double beta decay of ^{150}Nd in a magnetic field[9]. The DCBA detector, which is based on the experience of the VENUS vertex detector at TRISTAN[10], is designed to contain a large amount of source material and to determine a vertex point of double beta decay precisely by three-dimensional track reconstruction. The DCBA detector is described in Section 2. The analysis method of simulated data for backgrounds is in Section 3 together with the obtained results. Section 4 is the summary of the present work and of items for further analyses to be performed to obtain quantitative information of the backgrounds.

2. DCBA detector

Construction of the DCBA detector is divided into two stages, that is, DCBA-I and DCBA-II. Conceptual drawings of DCBA-I and DCBA-II are presented in Fig.3[9]. The DCBA-I comprises a drift-chamber module, nuclear source plates of natural Nd (an abundance of ^{150}Nd is 5.6%), a solenoidal magnet and plastic scintillation veto-counters against the cosmic ray backgrounds. The configuration of wires and the source plates in the drift-chamber module are shown in Fig.4.

Thickness of the source plate is 35 mg/cm^2 (about 50 μm) over tha total area of 4800 cm^2, which corresponds to the total source weight of 168g. The measurable half-life limit by DCBA-I after one year measurement is estimated to be 3×10^{21} yr. Since this value is longer than the theoretical values of $2\nu\beta\beta$ decay half-life of ^{150}Nd, it is possible to determine the matrix element of this decay from this experiment[9].

The DCBA-II detector, which follows DCBA-I, consists of 60 modules with source

plates of Nd_2O_3 enriched to about 90% ^{150}Nd, a large aperture solenoidal magnet of 3m diameter × 5m length and scintillation veto-counter as shown in Fig.3(b). Thickness of the source plate is 50 mg/cm^2. The source contains 4.5×10^{25} of ^{150}Nd in total. DCBA-II will reach a half-life limit up to 4×10^{24} yr after one year measurement under the condition of detection efficiency of 0.7, background rate of 0.1 keV^{-1}·yr^{-1} and energy resolution of 200 keV (FWHM), which corresponds to a limit on the effective neutrino mass to 0.1 - 0.5 eV, depending on nuclear matrix element[11][12]. The half-life limit attainable to measure by the DCBA-II detector is also indicated in Fig.2.

For a purpose of R&D for the DCBA detector, a prototype of 1/4 module of the detector is now under construction. A photo of this prototype is shown in Fig.5, where wires are strung partially. Data taking will start next year.

3. Monte Carlo simulation for background

3.1 Two-electron events

The double beta transition of ^{150}Nd to ^{150}Sm releases the total kinetic energy (Q value) of 3.367 MeV. A typical event of $0\nu\beta\beta$ decay in the DCBA detector generated by computer simulation is shown in Fig.6, where two electrons are emitted back to back [9]. One can see that two electrons are well recognized through signals of the detector. Spectral shapes of kinetic energy sum of the two electrons from $0\nu\beta\beta$ and $2\nu\beta\beta$ decay modes expected theoretically are shown in Fig.7 in arbitrary units. A sharp peak appears at the position of Q-value for $0\nu\beta\beta$ mode, while a broad structure below the Q-value is of $2\nu\beta\beta$ mode. Therefore events of $0\nu\beta\beta$ decay are identified by the accumulation of data at the position of Q-value in the distribution of the energy sum. We limit our discussion to the $0\nu\beta\beta$ decay of ^{150}Nd and its backgrounds at present.

Possible backgrounds disturbing the signals of $0\nu\beta\beta$ decay are events with two electron emitted from the source plate, which may be caused by γ rays hitting the source plate. Processes for the backgrounds taken into account in the present analysis are

1. two consecutive Compton scatterings by an incident γ ray (1C2C) as shown in Fig.8(a),
2. a Compton scattering followed by a Møller scattering (1C2M) as shown in Fig.8(b),
3. a pair production reaction followed by a Møller scattering (1P2M) as shown in Fig.8(c).

In order to understand event rates and energy dependence of the above three processes, a simulation program CMPsim (simulation of Compton scattering, Møller scattering and Pair creation) was coded based on formulae in ref.[13]. For electrons and positrons which

traverse the source plate, energy loss and multiple scattering in it are simulated in CMPsim using the Bethe-Bloch formula and the empirical formula for $< \theta^2 >$ of Gaussian form proposed by *Lynch* and *Dahl* [14], respectively.

Possible sources of γ rays are cosmic rays and radioactive contamination in materials with which the detector is constructed. For a study of the backgrounds due to these γ rays, the above three processes are simulated using the CMPsim codes below the γ ray energy of 10 MeV, where γ rays are assumed to hit the source plates isotropically. Fig.9 shows a number of two-electron events with both kinetic energies higher than 1 MeV as a function of incident γ ray energy, in which a hundred million of γ rays hit the source plate at each energy point. The lower limit of 1 MeV electron kinetic energy is imposed to use electrons well measured experimentally and well defined kinematically in the simulation code. In the case of $0\nu\beta\beta$ decay of ^{150}Nd, it is estimated using CMPsim that about 50% of the decay events will be lost by imposing the lower limit of 1 MeV.

Different behaviors of the above three processes with respect to energy of γ rays are seen in Fig.9. Number of two-electron events simulated using EGS4 [15] under the same condition as the case of CMPsim are also presented in Fig.9. They are in agreement generously. The minor difference between the results of CMPsim and EGS4 might be caused by any processes which are not taken into account, and/or by the simplified code calculating directions of e^+e^- emission in the reaction $\gamma \rightarrow e^+e^-$ in CMPsim.

3.2 S/N ($0\nu\beta\beta$ signal to background noise) ratio

The behavior of two electrons coming from $0\nu\beta\beta$ decays of ^{150}Nd which occur uniformly in the source plate is simulated by the EGS4 code. Fig.10(a) shows distributions of kinetic energy sum of the two electrons thus obtained, where both electrons of the used event have kinetic energies higher than 1 MeV. One can see that the accumulated events at the position of the Q value are followed by a tail due to energy loss of electrons in the source plates.

In order to compare the spectra of two electrons of $0\nu\beta\beta$ decays with those of the backgrounds, two-electron events coming from the backgrounds due to γ rays hitting the source plates have been simulated by the EGS4 code. Fig.10(b) shows the distributions of kinetic energy sum of the two electrons of the backgrounds for different energies of γ rays (dashed lines; 3MeV, solid lines; 4 MeV, dot-dashed lines; 6 MeV and dotted line; 8 MeV), where a hundred million of γ rays hit the source plates at each energy and electrons of kinetic energy higher than 1 MeV are used. One can see from this figure that γ rays of the energy between 4 and 6 MeV significantly contribute to accumulate the two electron background events at the position of the Q-value. Therefore it is important to suppress the γ rays of these energies in order to improve S/N ratio.

The DCBA-II detector will reach a half-life limit up to 4×10^{24} yr after one year measurement if a detection efficiency of 0.7, a background rate of 0.1 $\mathrm{keV}^{-1} \cdot \mathrm{yr}^{-1}$ and an energy resolution of 200 keV are achieved[9]. Assuming that sum energies of the two electrons of $0\nu\beta\beta$ decays distribute mostly in the interval 2.8-3.4 MeV as shown in Fig.10(a), the background rate of 0.1 $\mathrm{keV}^{-1} \cdot \mathrm{yr}^{-1}$ corresponds to 60 background events per year in this interval. Number of γ rays of the energy between 4 and 6 MeV, which produces the 60 background events in the interval of 2.8-3.4 MeV, is about 5 millions, therefore γ rays of this energy range should be suppressed to below this value in order to improve the measurable half-life limit of 4×10^{24}yr. This number is valid within 10% in variation of the source-plate thickness between 35 and 50 mg/cm^2 if the numbers of nuclei in the source plates are same in total.

Energies and intensities of γ rays from radioactive contaminations in materials of the prototype detector were estimated from the data measured by a Ge detector at Radiation Safety Control Center at KEK. Among the 30 kinds of materials measured, estimation from Al, G10 and environment (BGD) are listed in Table 1. Absolute intensity of γ from other materials are negligibly small. One can see from this Table that γ rays from the contaminations do not contribute to two-electron background events at the present condition.

3.3 Background in other $0\nu\beta\beta$ sources

It is theoretically predicted that some nuclei may decay through the $0\nu\beta\beta$ mode, and those of high Q value (for example higher than 2.5 MeV) are ^{48}Ca, ^{82}Se, ^{96}Zr, ^{100}Mo, ^{116}Cd and ^{130}Te in addition to ^{150}Nd. Since nuclei of high Q value are preferable experimentally, any source of the above nuclei may be usable as well as ^{150}Nd by simply replacing the source plates. Number of the two-electron background events simulated by the EGS4 code for the above nuclei are shown in Fig.11 as a function of γ ray energy. In this simulation, the source-plate thickness of each nucleus is adjusted so as to contain the same number of nuclei per cm^2 as the case of ^{150}Nd, and a number of γ rays hitting the source plate is one hundred million for each energy. One can see from Fig.11 that the number of backgrounds increases with increase of atomic number.

4. Summary

We can summarize the present study of the backgrounds disturbing $0\nu\beta\beta$ decay signals as follows.

1. Main contribution to the backgrounds is two-electron events caused by the processes of two consecutive Compton scatterings, a Compton scattering followed by a Møller

scattering and a pair production reaction followed by a Møller scattering.

2. Energy dependence of the number of two-electron events due to the above-mentioned processes is studied by using the EGS4 code and the CMPsim code, and the results of both codes are generouly in agreement.

3. Backgrounds of the two-electron events caused by γ rays of 4 to 6 MeV strongly disturb the distributions of energy sum of $0\nu\beta\beta$ decay signals, therefore these γ rays should be suppressed to below 5 millions to keep or to improve the measurable half-life limit of 4×10^{24} yr.

4. γ rays emitted from radioactive contaminations in the materials composing the prototype detector do not contribute to the background.

5. Number of background events increase with increase of atomic number of the source nuclei.

Next steps we have to study are as follows.

1. A number of background events due to cosmic rays, paying attention to high energy γ rays, should be eastimated.

2. Since electron kinetic energy in the present analysis is limited to the region above 1 MeV, it should be extended down to , for example, 500 keV. The electrons below 1 MeV are important to study the background disturbing the data of $2\nu\beta\beta$ decay signals, and the application code PRESTA in EGS4 make it possible to get information about the behavior of low energy electrons in materials.

3. It is important to study data obtained by the prototype detector, which is under construction now, in comparison with the results of simulation.

Acknowledgment

We wish to thank Prof. H. Hirayama of KEK for his help with the measurement of γ rays from the detector component materials using a Ge detector.

References

[1] H. V. Klapdor-Kleingrothaus, Proceedings of the Internetional Workshop on *Double-Beta Decay and Related Topics*, edited by H. V. Klapdor-Kleingrothaus and S. Stoica, (World Scientific, Singapore,1996, p.3), Trento, Italy, 1995.

[2] F. Boehm and P. Vogel, *Physics of Massive Neutrinos*, Cambridge Univ. Press. 2nd ed, 1992.

[3] M. Doi, T. Kotani and E. Takasugi, Prog. Theor. Phys. Suppl. **83**(1988)1.

[4] T. Tomoda, Rep. Prog. Phys. **54**(1991)53.

[5] K. S. Hirata et al., Phys. Rev. **D44** (1991)2241.

[6] K. S. Hirata et al., Physics Letters **B280** (1992)146.

[7] C. Athanassopoulos et al., LA-UR-95-1238 (1995).

[8] A. Balysh et al. HEIDELBERG-MOSCOW Collaboration, Physics Letters **B356** (1995)450.

[9] N. Ishihara, T. Ohama and Y. Yamada, Nucl. Instrum. Methods Phys. Res., Sect.A**373**(1996)325.

[10] Y. Yamada et al., Nucl. Instrum. Methods Phys. Res., Sect.A**370**(1993)64.

[11] A. Staudt, K. Muto and H. V. Klapdor-Kleingrothaus, Europhys. Lett. **13**(1990)31.

[12] J. G. Hirsch, O. Castanos and P. O. Hess, Nucl. Phys. A**582**(1995)124.

[13] W. Heitler: *Quantum Theory of Radiation*, (Oxford, 1954, Japanese translator K.Sawada, Yoshioka-Shoten, 1957)

[14] W. R. Leo, *Techniques for Nuclear and Particle Physics Experiments*, (Springer-Verlag, 1994).

[15] W. R. Nelson, H. Hirayama and D. W. O. Roger, The EGS4 code system, SLAC-265 (1985).

Table 1

γ rays from the detector component materials

Energy (keV)	Al	G10	BGD	Total	γ-source
	($\times 10^6$ counts/year)				
511	6.05	0.29	0.40	6.74	e^+ annihilation
583	—	1.06	0.08	1.14	^{208}Tl
609	4.35	1.32	0.08	5.75	^{214}Bi
844	18.14	—	0.05	18.19	^{27}Mg / ^{56}Mn
911	—	1.21	0.03	1.24	^{228}Ac
1120	—	0.28	0.01	0.29	^{214}Bi
1463	2.65	0.58	0.14	3.37	^{40}K
1772	6.80	1.01	0.01	7.82	^{214}Bi
2645	—	—	0.09	0.09	^{208}Tl

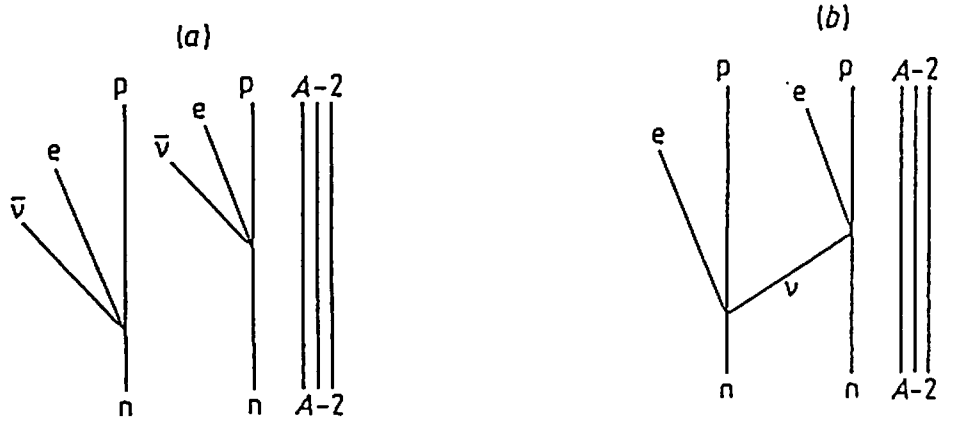

Fig. 1. Two-nucleon mechanism for (a) two-neutrino and (b) neutrinoless $\beta\beta$ decay[3].

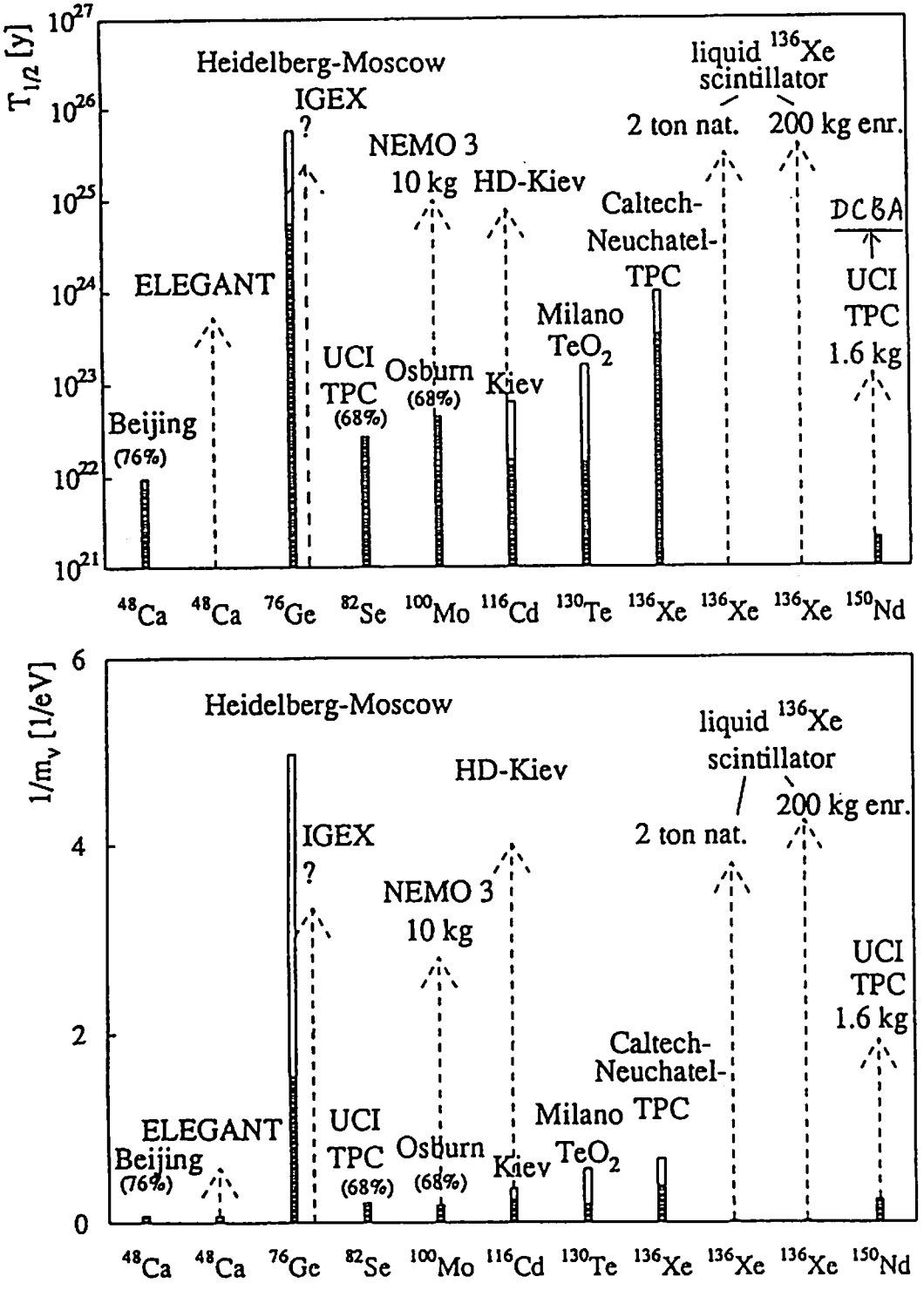

Fig. 2. Present situation, 1995, and expectation for the near future until the year 2000, of the most promising $\beta\beta$ experiments[1] together with the expectation of the DCBA-II detector.

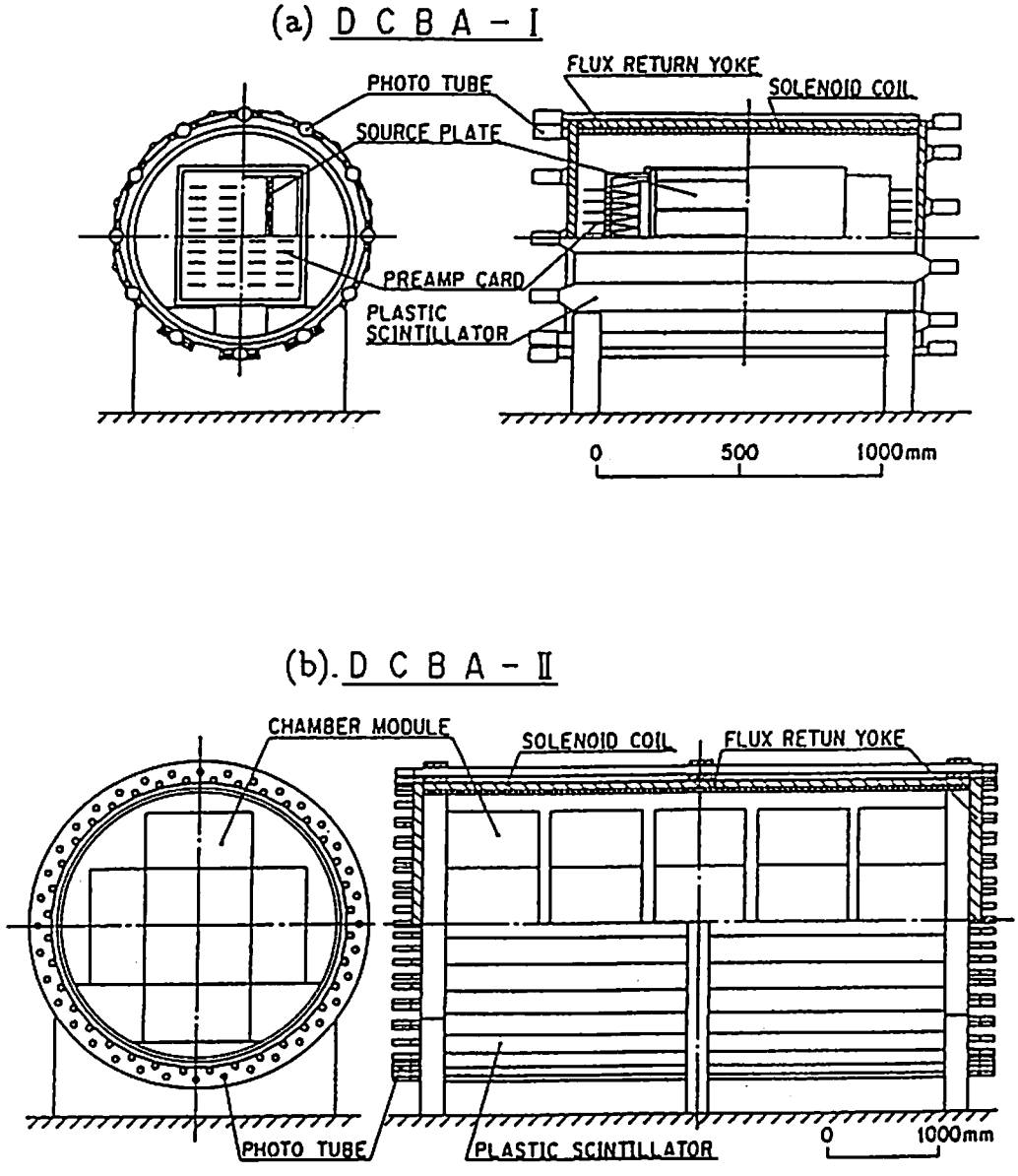

Fig. 3. Conceptual drawings of (a) DCBA-I and (b) DCBA-II[9].

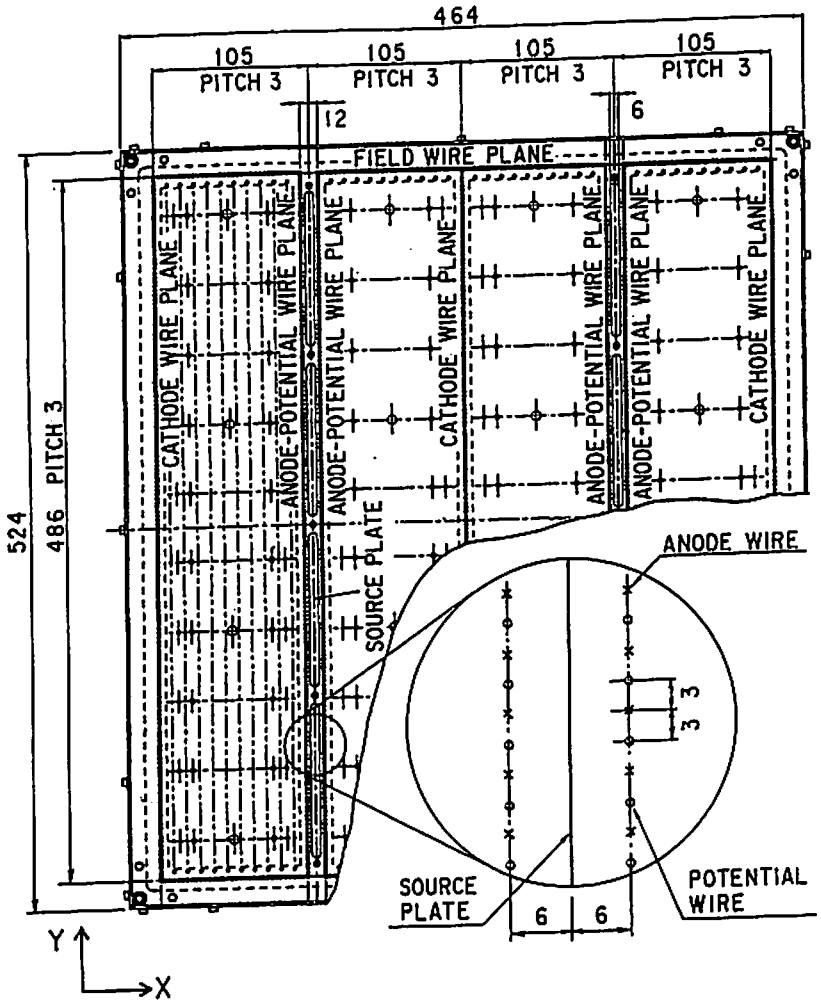

Fig. 4. Configuration of the wires and the source plates for a chamber module of DCBA[9]. Scale unit in the drawing is in mm.

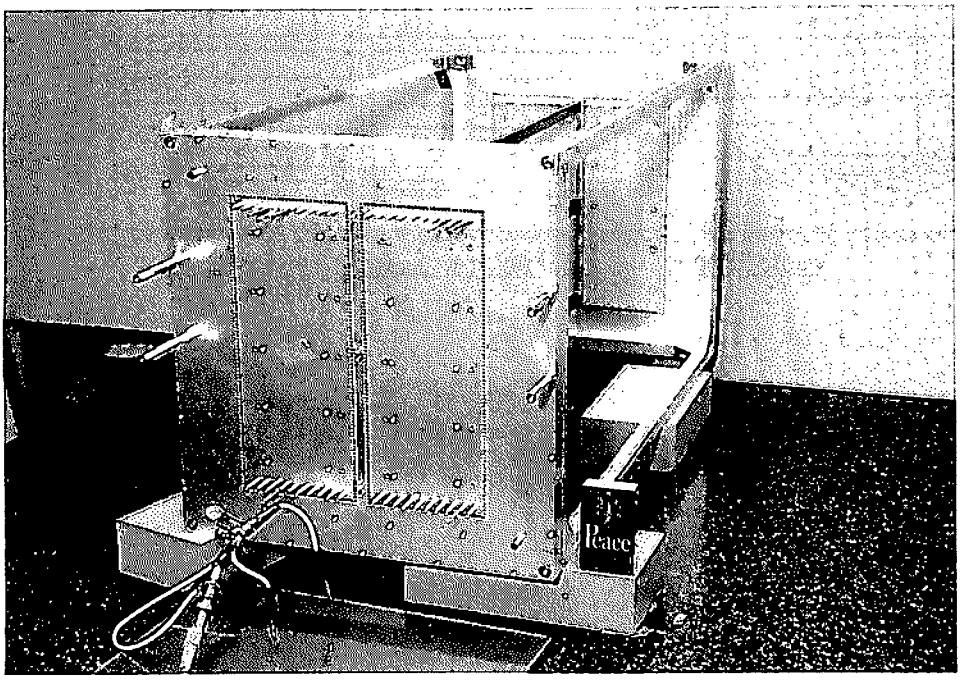

Fig. 5. A photo of the prototype of the DCBA detector (1/4 module).

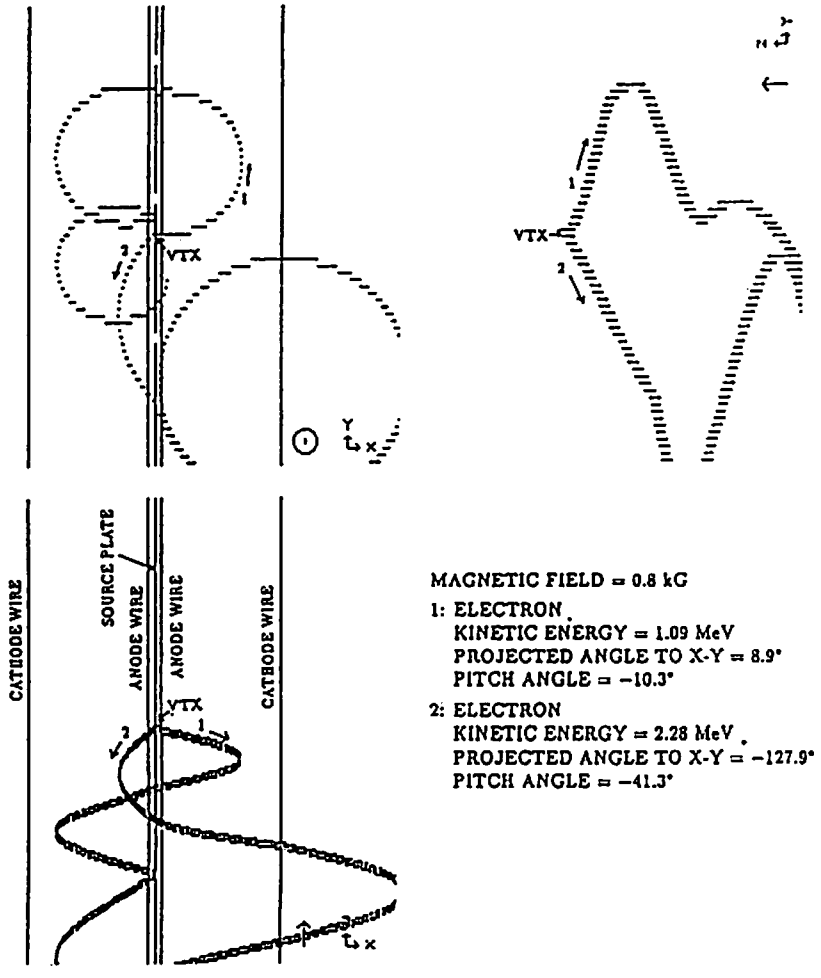

Fig. 6. An example of the simulated $0\nu\beta\beta$ event emitted back to back at DCBA [9].

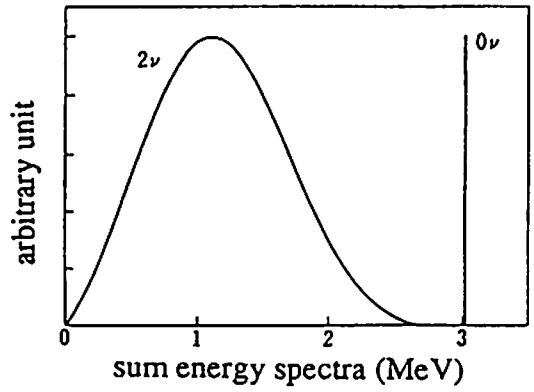

Fig. 7. Sum energy spectra for the $0\nu\beta\beta$ and $2\nu\beta\beta$ decay modes with arbitrary unit on the vertical axis.

Fig. 8. Processes of background events emitting two electrons, (a) two consecutive Compton scattering(1C2C), (b) a Compton scattering followed by a Møller scattering(1C2M), (c) a pair creation reaction followed by a Møller scattering(1P2M).

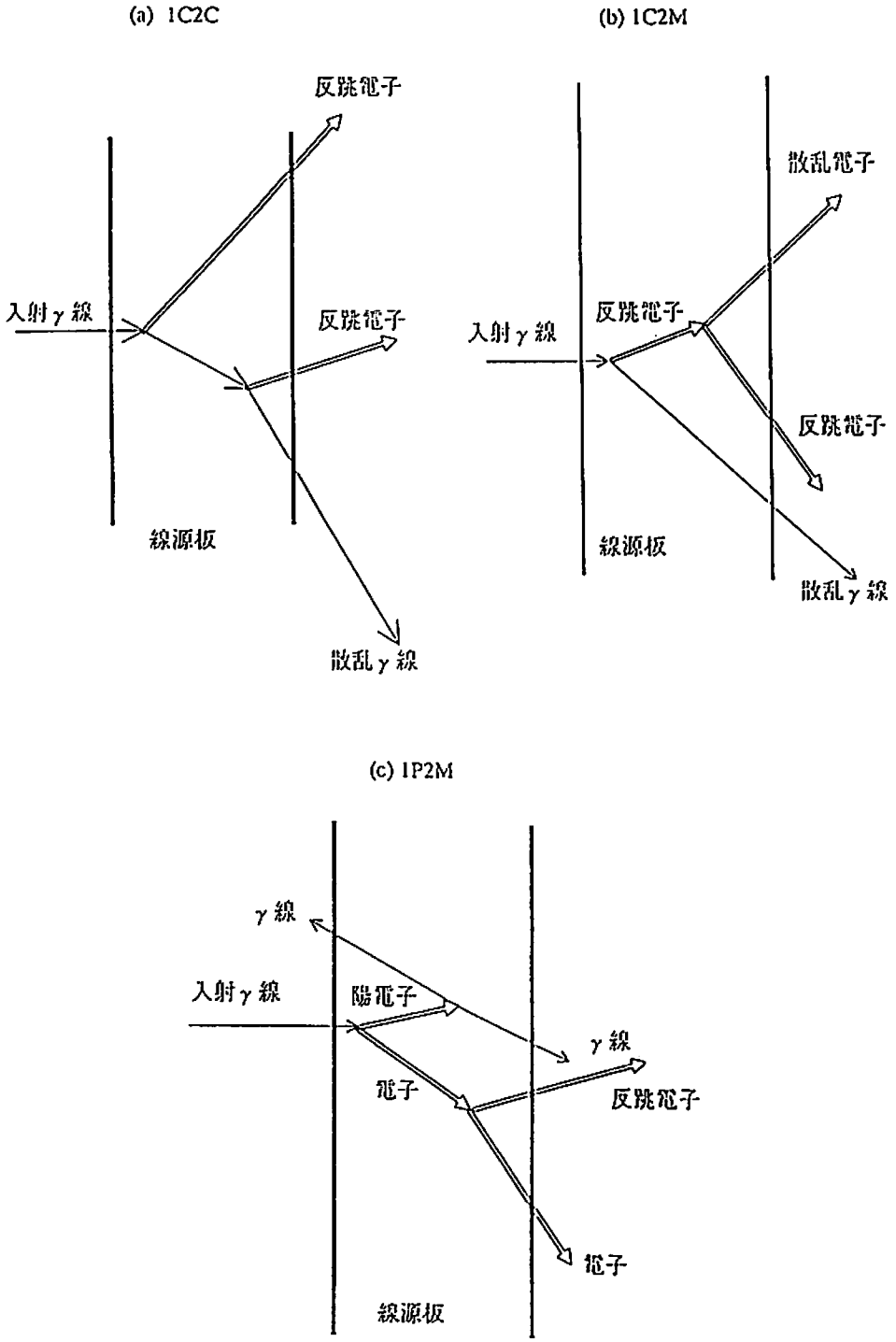

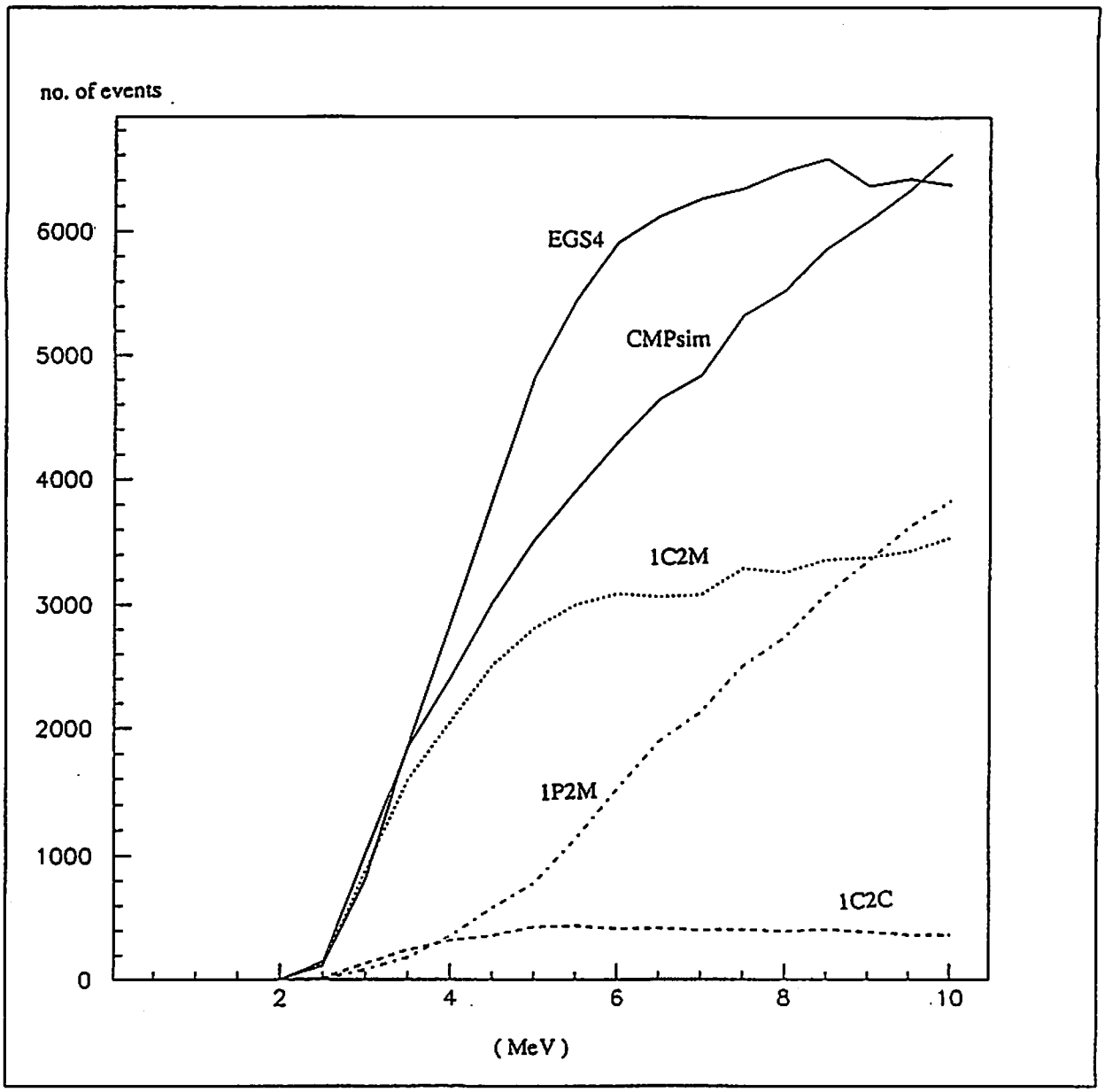

Fig. 9. Number of background events emitting two electrons (kinetic energy>1 MeV) as a function of incident γ energy. 1C2C, 1C2M and 1P2M indicated in this figure correspond to those in Fig.8, and CMPsim is the sum of those processes. EGS4 is the number of background events obtained by the EGS4 simulation. Number of incident γ rays is one hundred million at each energy.

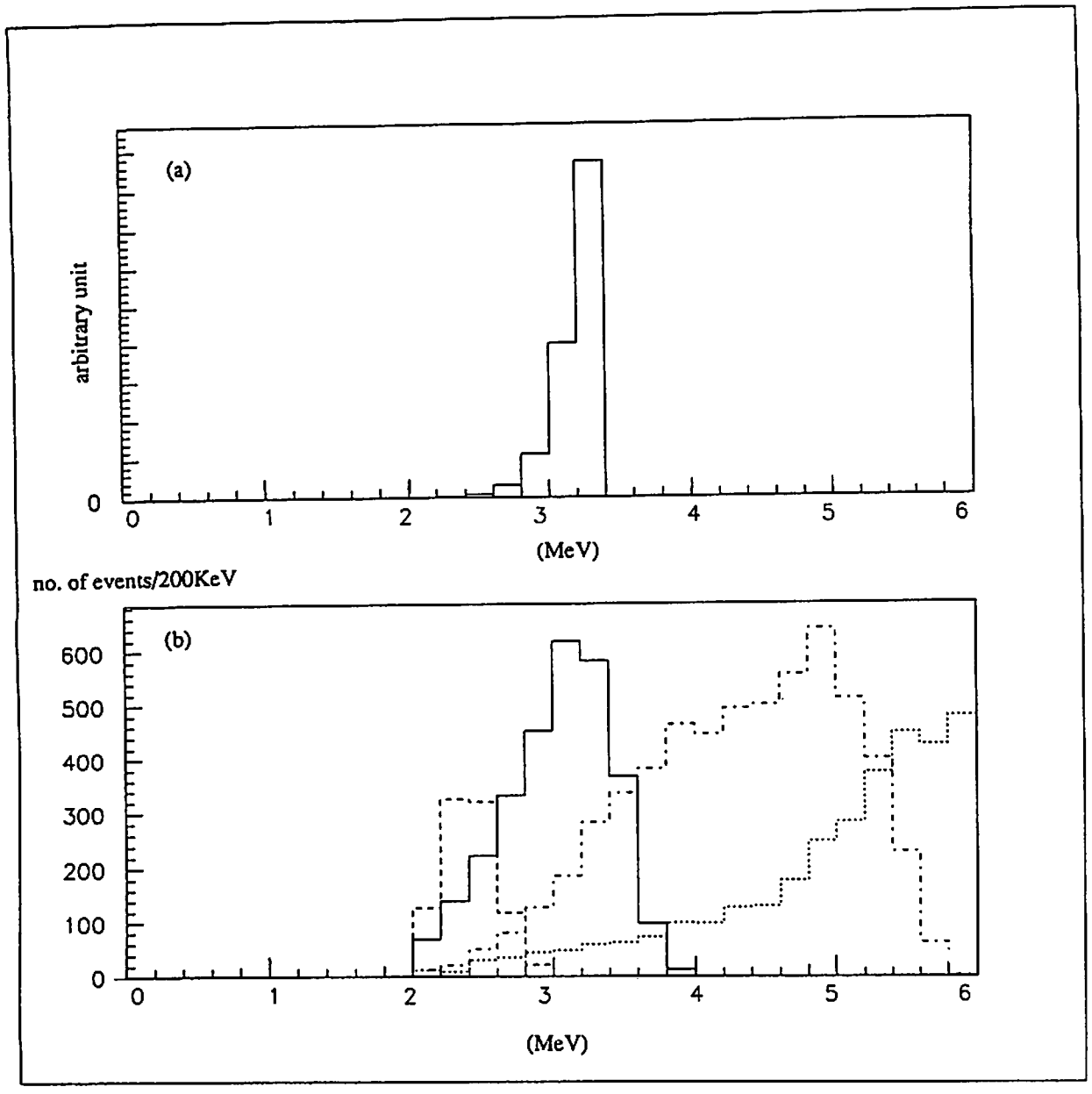

Fig. 10. (a) Sum energy spectrum of $0\nu\beta\beta$ decay from ^{150}Nd (Q value is 3.367 MeV) with arbitrary unit on the vertical axis. (b) Sum energy spectra of the two-electron background events for the energy of incident γ rays of 3 MeV (dashed lines), 4 MeV (solid lines), 6 MeV (dot-dashed lines), and 8 MeV (dotted line). Number of γ rays is one hundred million for each energy. Distributions of both (a) and (b) are obtained by EGS4, where the lower limit of 1 MeV electron kinetic energy is imposed.

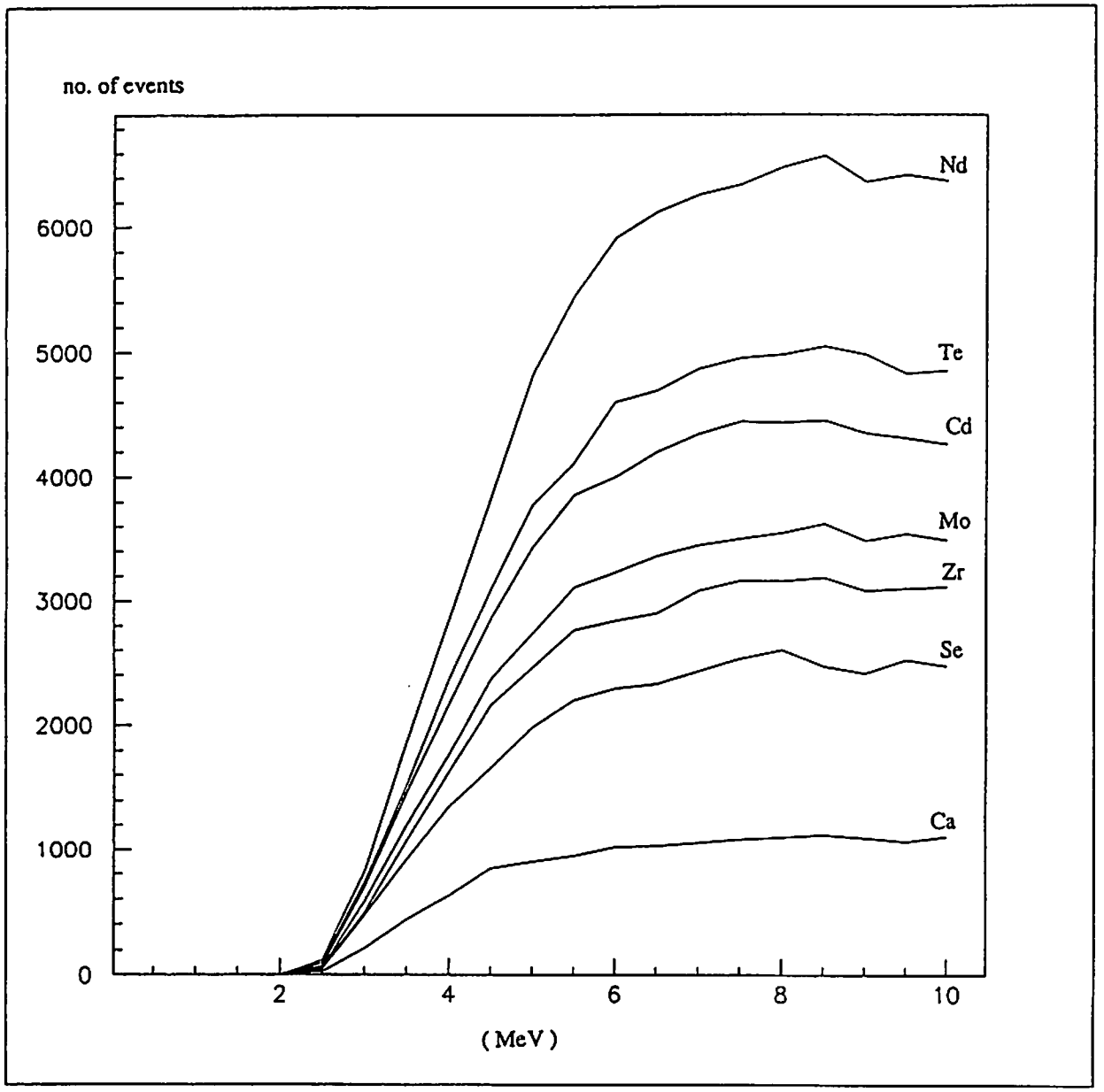

Fig. 11. Number of background events emittimg two electrons (kinetic energy > 1 MeV) for other nuclei as a function of incident γ energy obtained by the EGS simulation under the same condition as in Fig.9.

SIMULATION STUDY OF X-RAY POLARIMETRY USING THE PHOTO EFFECT IN THE MICROSTRIP GAS CHAMBER

Y. NISHI, S. AOKI, A. OCHI, AND T. TANIMORI

Department of Physics, Tokyo Institute of Technology, Tokyo 152 Japan

Abstract

We have developed a two-dimensional MicroStrip Gas Chamber(MSGC) with a 5cm × 5cm detection area. Using this MSGC, we succeeded to measure the X-ray polarization in the range of 6keV ∼ 14keV. Using EGS4 we have simulated the performance of the MSGC as a X-ray imaging polarimeter for the development of the specialized MSGC as an imaging polarimeter. In this article, we report on the result of a simulation and the comparison with actual polarization measurement.

1. Introduction

We have developed a two-dimensional MicroStrip Gas Chamber(MSGC) with a 5cm × 5cm detection area based on Multi-Chip Module(MCM) technology[1]. It has a very thin substrate of $20\mu m$ thickness, 254 anode, and 255 back strip both with $200\mu m$ pitches. MSGC provides excellent position resolution and many other capabilities. Fine position resolution of the MSGC allows us to measure the track of photoelectrons emitted from gas, which provides us an information about the electric vector $\vec{E}$ of the incident X-ray. Our research for MSGC is being carried out mainly in order to use it as a real-time X-ray imaging detector in the SPring-8 synchrotron radiation facility in Japan[2]. Using this MSGC, we succeeded to measure the X-ray polarization in the range of 6keV ∼ 14keV[3]. In addition, we have simulated the performance of the MSGC as X-ray imaging polarimeter for the development of the specialized MSGC as an imaging polarimeter, by which the parameters of the MSGC, such as a pitch of anode and backstrips, or the selection of a gas, will be optimized for the measurement of the X-ray polarization. In this article, we report on the result of a simulation and the comparison with actual polarization measurement.

2. Detection of X-ray polarization by two dimensional MSGC

The MSGC has a detection area of 5cm × 5cm. As shown in Fig.2, $10\mu m$ wide anodes and $100\mu m$ wide cathodes are formed on the polyimide substrate with $200\mu m$ pitch. Between the ceramic base and polyimide substrate, there are back strips with a $200\mu m$ pitch orthogonal to the anodes. All electrodes are made of gold with a thickness of $1\mu m$. To define the drift field, the drift plane was placed at $3mm$ above the substrate. All anodes and back strips is connected to the read out electronics. Then there are more than 500 outputs. The read-out system consists of pre-amplifier cards, discriminator boards, multi-hit CAMAC TDCs(Time to Digital Converters,LeCroy 2277), and a Unix workstation for data acquisition from the CAMAC system. By using the timing of pulse, accidental or electrical noises were perfectly removed.

Incident X-rays are absorbed by photoelectric effect in the gas of the MSGC (Ar 80% C_2H_6 20%). Differential cross section of scatter angle of the photoelectrons is as follows[4],

$$d\sigma = r_0^2 \frac{Z^5}{137^4} \left(\frac{\mu}{k}\right)^{\frac{7}{2}} \frac{4\sqrt{2}\sin^2\theta\cos^2\phi}{(1-\beta\cos\theta)^4} d\Omega \tag{1}$$

(where θ is a polar angle and ϕ is an azimuth which is measured from the direction the electric field vector $\vec{E}$).

This formula shows that photoelectrons prefer to emanate along the electric field vector $\vec{E}$. The range of the photoelectron in Ar gas(1 atm) is approximately 1mm for 8keV X-rays. This is enough length for photoelectrons to run beyond several strips of the MSGC, where the numbers of the hit anode and backstrips corresponds to the projection of the polarization vector on the both directions of the anode and the cathode respectively. When X-rays are linearly polarized, there appears an asymmetry between the numbers of hit anodes and hit backstrips. For the measurement of the polarization, the modulation factor M is defined as,

$$M = \frac{A-B}{A+B} \tag{2}$$

where A(B) is the number of events such as the hit number of anodes(back strips) is larger than backstrips(anodes).

In this measurement, the polarized X-rays were generated using perpendicular Thomson scattering X-rays from the plastic plate which was irradiated by the X-ray generator. The MSGC was rotated against the Electric field vector $\vec{E}$ of incident X-rays. The measured modulation factors are shown in Fig.3 as a function of incident X-ray energy which was measured from the pulse height of the cathode, where θ means the angle between the direction of anode strips and electric field $\vec{E}$ of incident X-rays.

Thus we successfully measured the X-ray polarization in the energy range of 6keV ~ 14keV.

This result shows that MSGCs are superior to CCDs[5] as an imaging X-ray polarimeter below 15keV.

3. The simulation

We developed the simulation of polarimetry in the MSGC based on EGS4. In order to simulate low energy X-rays and photoelectrons transport in EGS4, we added some expansion codes - PRESTA, LSCAT, and the code which calculates the angle of photoelectrons according to the equation(7) [6]. Since an Auger electron is regarded as an energy deposit at the point where photoelectric effect occurs in EGS4, we emitted an electron having the same energy as Auger electron isotropically from the hit point. The output data of EGS4 was used as the input data of another code which was developed for the simulation of the response of the MSGC. In this code, the energy deposits were converted into the electron-ion pairs using W value for argon(26eV), and generated secondary electrons were diffused according to the gauss distribution. Since we didn't find accurate value of diffusion constant, we examined the effects of the diffusion constant by changing its value in the typical values, $50\mu m$,$150\mu m$ and $300\mu m$ as mentioned in the next section.

Fig.5 shows the geometry of the electrodes of MSGC used in the simulation, which consists of $200\mu m \times 200\mu m$ pixels. Samples of simulated tracks of photoelectrons and Auger electrons by 8keV X-rays are also shown in this figure. Incident X-rays were completely linearly polarized, and put in the central pixel uniformly. The number of secondary electrons were summed up along the directions of each strip which was defined as a column of pixels. When more than 36 electrons were generated in one strip, the strip was considered to be hit (36 electrons corresponds to the experimental threshold pulse height). Fig.6 shows the simulated modulation factor as function of incident X-rays energy.

4. Comparison of measurement to simulation result

As shown in Fig.3 and Fig.6, our simulation result approximately agrees with the measurement. Fig.6 shows that simulated results by changing diffusion constant, and the uncertainty of the diffusion constant is found to cause little effect for the simulated result. In the two Figs. 3,6, abscissas don't represent the same value. In Fig.3 it means the energy band, while in Fig.6 it means the monochromatic energy of incident X-rays.

5. Conclusions and the Future

Using EGS4, we have simulated the performance of MSGC as a polarimeter with reasonable accuracy, and this simulation well reproduced the measurement. ¿From now we will optimize some parameters of the MSGC, for example gas mixture, strip pitch and

so on, in order to improve the analyzing power of the MSGC as a imaging polarimeter.

Acknowledgment

We would like to thank Prof. Y. Namito of KEK for him help about EGS4. And we also appreciate Prof. F. Makino, T. Takahashi, Dr. Y. Ueda, and Miss K. Okada of ISAS for their kind support during a polarization measurement.

References

[1] T. Tanimori et al. INS-Report 1143 (1996) (accepted for publication in Nucl. Instr. and Meth. A).

[2] SPring-8 Annual Report (1994), SPring-8, Kamigori-cho, Ako-gun, Hyogo 678-12, Japan.

[3] A. Ochi et al. Proc. Int. Conference on Position-Sensitive Detectors, Univ. of Manchester (1996) (to be published in a special edition of Nucl. Instr. and Meth.)

[4] W. Heitler, *The Quantum Theory of Radiation*, Oxford at the Clarendon Press 1954.

[5] K. H. Shmidt et al. Nucl. Instr. and Meth. **A367**, 215(1995).

[6] Y. Namito, S. Ban and H. Hirayama, Japan Atomic Energy Society, H30, Sendai, Sep. 1996(Abstract, in Japanese)

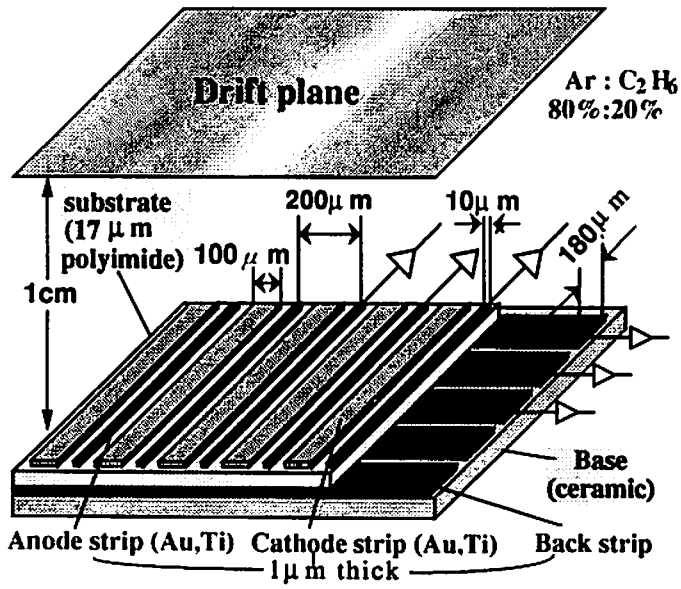

Figure 1: Schematic structure of the two-dimensional MSGC

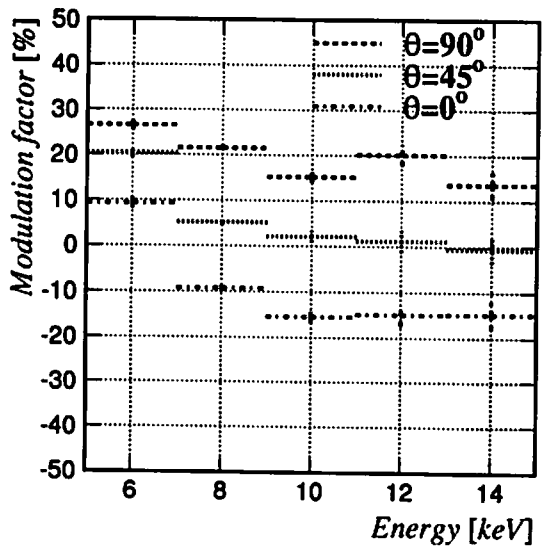

Figure 2: Experimental result of modulation as a function of energy

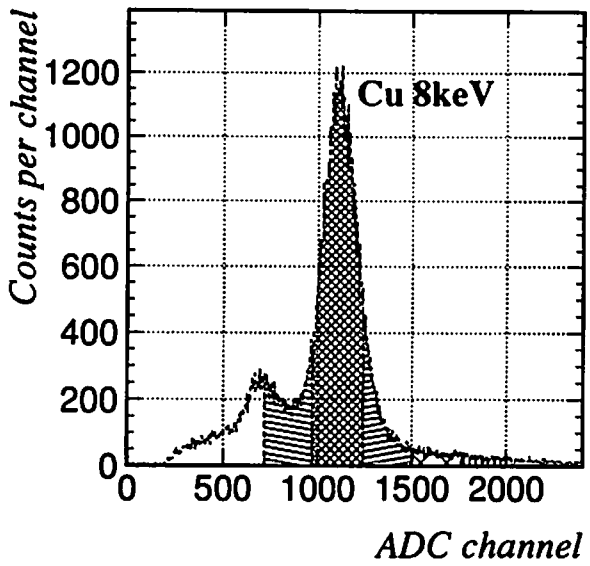

Figure 3: Measured pulse height spectrum of X-ray generator with Cu target

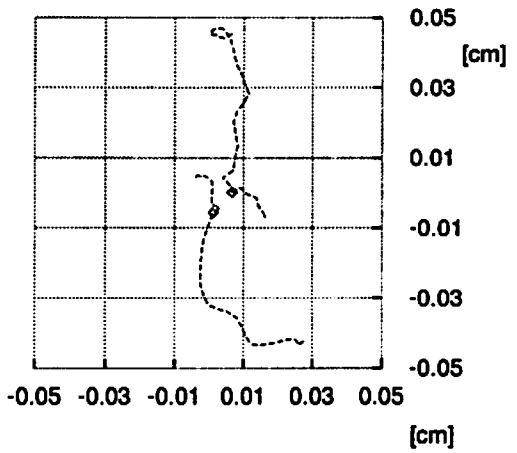

Figure 4: Samples of tracks

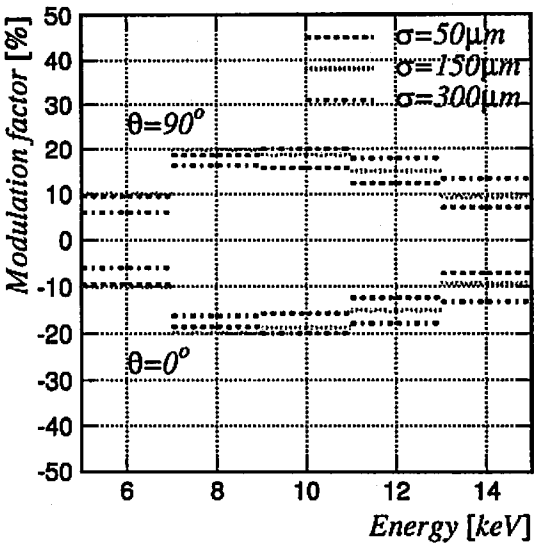

Figure 5: Simulation result of modulation as a function of incident X-ray energy

A DESIGN STUDY OF THE COLLIMATOR SYSTEM FOR THE NEUTRAL BEAM LINE

T. SATO

National Laboratory for High Energy Physics
1-1 Oho, Tsukuba-shi, Ibaraki 305 Japan

1. Introduction

We are now preparing a proposal to search for a rare decay mode $K_L \rightarrow \pi^0\nu\nu$ to the KEK 12GeV Proton Synchrotron. K_L's are produced by bombarding a metal target with a proton beam. They are collected with a collimator system made with heavy metal. Although the charged particles produced at the target are swept out by the magnetic field around the collimator, the neutral particles such as neutrons and gammas are contaminating the K_L beam. Because the amount of these contamnating particles are estimated to be nearly 1000 times of the K_L, we need to study the behavier of these contaminating particles to make the experiment successful.

In this note, we describe the results of the simulation for the gammas coming from the decays of the neutral pions produced at the target by using the EGS4 code.

2. The Collimator System for the Neutral Beam Line

Fig.1 illustrate the schematic view of the collimator system and the experimental detector. The 12GeV proton beam hit the metal target and produced nertral particles are collected through the holes of the collimators and injected into the detector system shown in the figure. As any halo of the neutral beam will produce serious background for the experiment, we need to reduce the beam halo of the neutral beam as much as possible. The main purpose of this study is to simulate the beam profile and the halo distribution by using the EGS4 code and to make sure that the collimator system could reduce the beam halo to the satisfactory level.

Fig.2 shows a schematic drawing of the holes of the collimator system. At z=0, we have a production target made by cupper and its length is 120mm and its radius is 4mm. You can imagine the collimator system by rotating Fig.2 around the z-axis. The collimators are made of heavy metal of which principal element is tungsten. The acceptance half angle of the collimator system is 2mradian. Although most part of the collimator will be made

with brass and only the thickness equivalent to 0.5-1 interaction length will be made with tungsten, we assumed all the collimators are made with tungsten for the EGS4 calculation.

The energy spectrum of the neutral pions produced at the production target is estimated by using Sanford-Wang's formula. Fig.3-a shows the energy distribution of the neutral pions thus produced. Fig.3-b shows the energy distribution of the gammas produced via the decays of the neutral pions. These energy spectrum is obtained by collecting the gammas produced at 6 degree from the incident proton beam.

3. A comparison of the CONE Type and CYLINDER Type of the EGS4

The holes of the collimators have tapers in them. And we should have used CONE type configulations for the simulation by using the EGS4. As we have not used a CONE type configulation in the EGS4 calculation, we tried to compare the CONE type configulation and the CYLINDER type configulation.

Fig.4-a shows an exapmple of a short collimator with a CONE type hole in it. Fig.5-a shows an example of a short collimator with four successive CYLINDERs which make a CONE type hole similar to the collimator shown in Fig.4-a. We exposed these collimators to the gamma beam of which energy was 2000MeV. The Beam size was 2cm x 2cm.

Fig.4-b and c show the energy and x distributions at the exit of the CONE type collimator. Fig.5-b and c show the same distributions at the exit of the CYLINDER type collimator. These distributions are very similar and we concluded to be able to use CONE type configulation in simulating the neutral beam line.

4. The Results of the Simulation

Fig.6 shows the radial(x) distribution of the incident gammas at the target. We generated gammas of which energy distribution was shown in Fig.3-b in front of the target. This could simulate the gammas emitted to the 6 degree direction from the target bombarded by the 12GeV proton beam. The gammas thus generated irradiated the front face of the collimator system shown in Fig.2. Fig.7 show the beam profiles at the exits of the six collimators. We can see the halo at each collimator exits is gradually becoming smaller. The beam shown in Fig.7 consists of not only the gammas but electrons and positrons. In Fig.8 we traced the beam after the collimator system. It can be seen that the halo produced at the last(sixth) collimator spread as the beam travels further.

Fig.9 and Fig.10 show the charge, energy, x and y distributions at the exit of the first collimator and at 5.95m behind the last collimator where the detector front face comes respectively. From the charge distributions in the Figs.9-a and 10-a,. we can see that electrons and positrons in the nertral beam is decreasing dramatically as the beam is passing throgh the collimator system. This means that we don't need a very

strong magnetic field around the collimator system. The energy distributions at the first collimator and at the detector is very similar except for the low energy component is absorbed at the end of the collimator system.

In Fig.10-c and d, we see that the beam halo component is order of five smaller than the main part of the beam. This could be compared with Fig.9-c and d which shows the same distributions at the first collimator, where the ratio of beam halo to the main component is only 1000.

Fig.11-a shows the scatter plot of energy and x of the beam at the detector. It shows that most of the halo component have very small energy compared to the main beam component.

5. Summary

We simulated the behavior of the gamma beam produced from a metal target bombarded by the 12GeV proton beam by using the EGS4 code.

It was made clear that the beam halo at the experimental detector was the order of five smaller compared to the central beam component.

The main part of the beam consists of mainly gammas and the contaminations of electrons and positrons are very small.

The energy of the halo is small(mostly less than 300MeV) compared to the main component of the neutral beam.

These characteristics of the neutral beam allow us to perform a rare decay search experiment by using this type of collimator system.

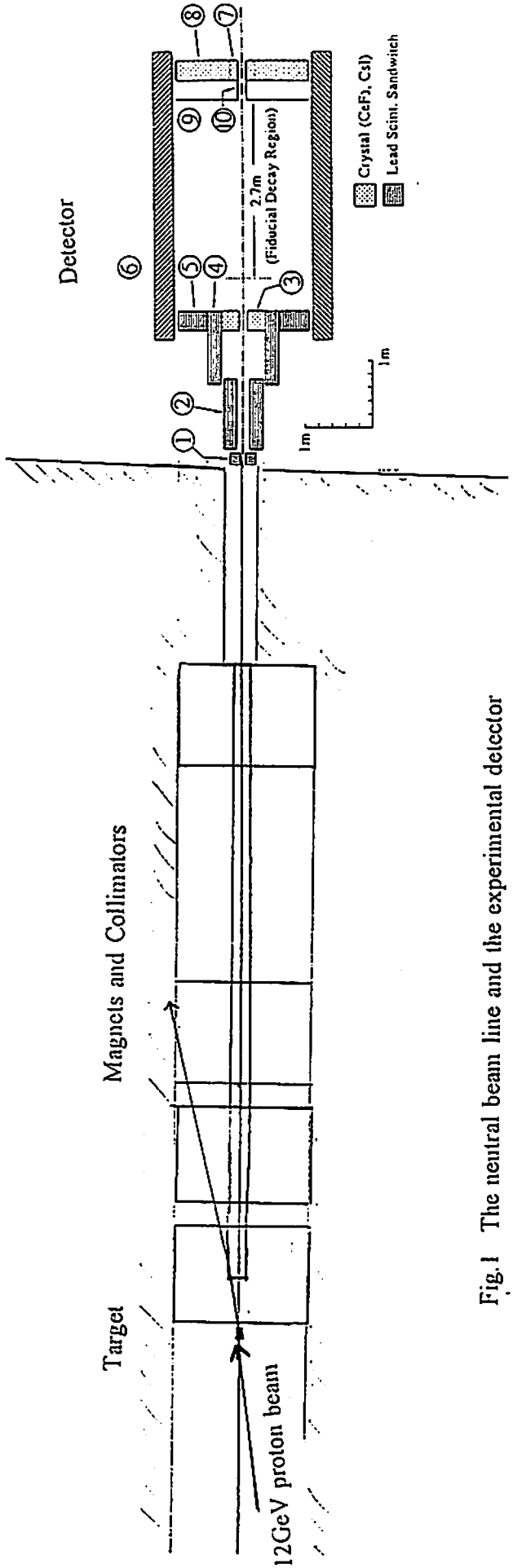

Fig.1 The neutral beam line and the experimental detector

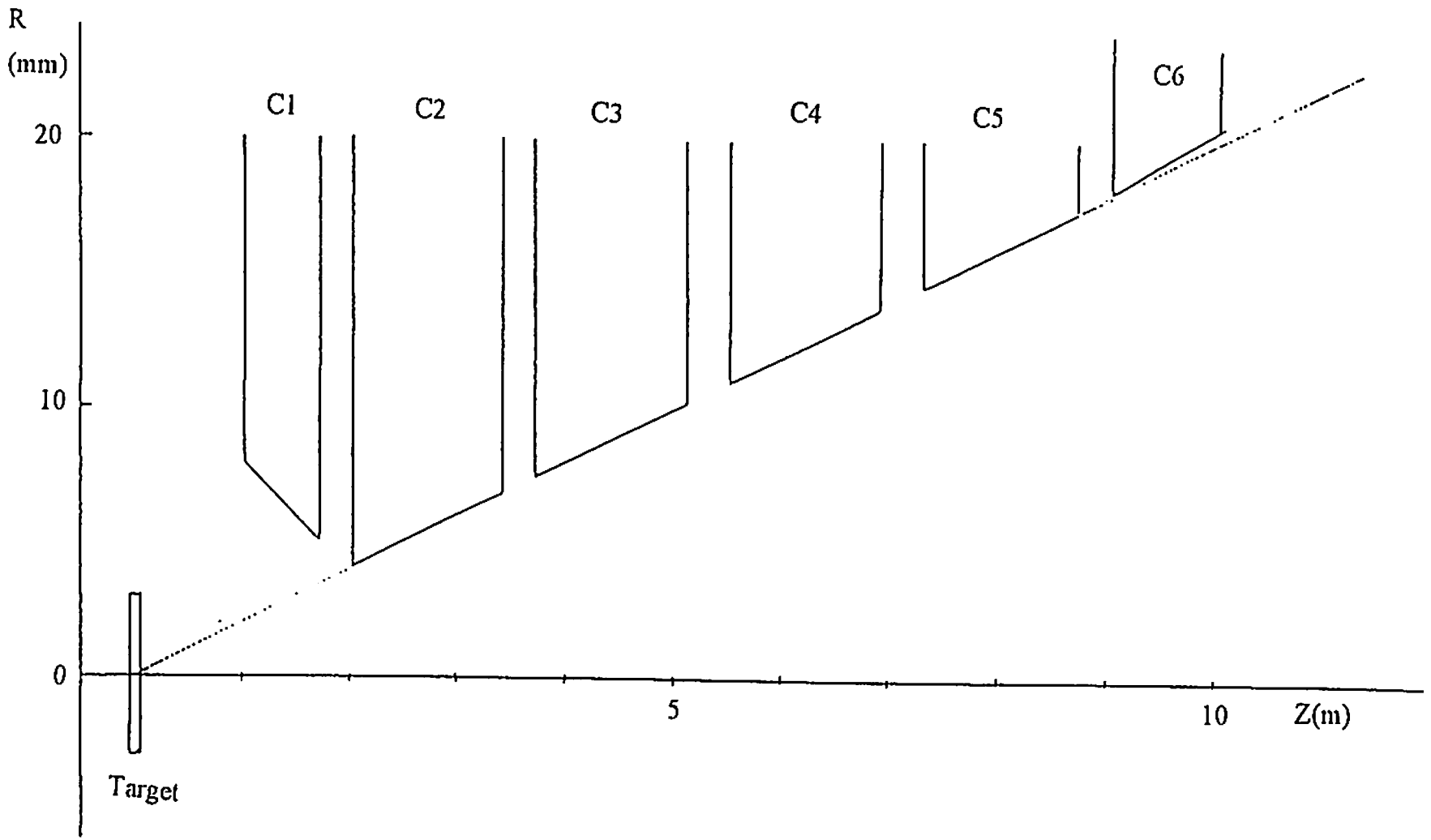

Fig.2 The schematic drawing of the holes of the collimator system together with the neutral beam production target

a) Energy distribution of the neutral pions produced by the 12GeV proton beam.

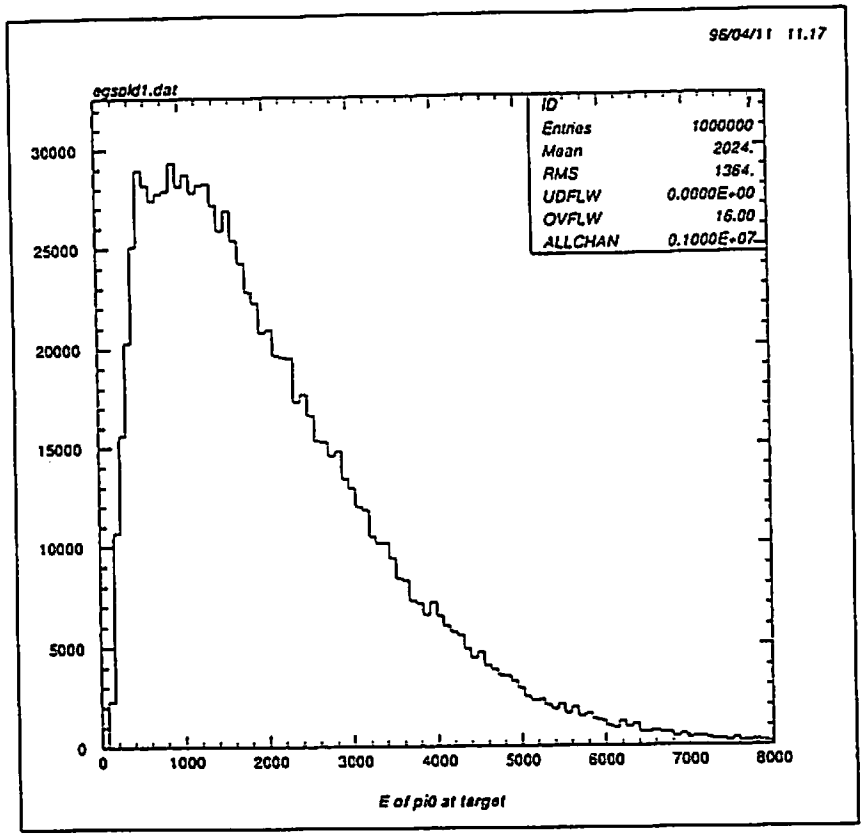

b) Energy distribution of the gammas decayed from the pions.

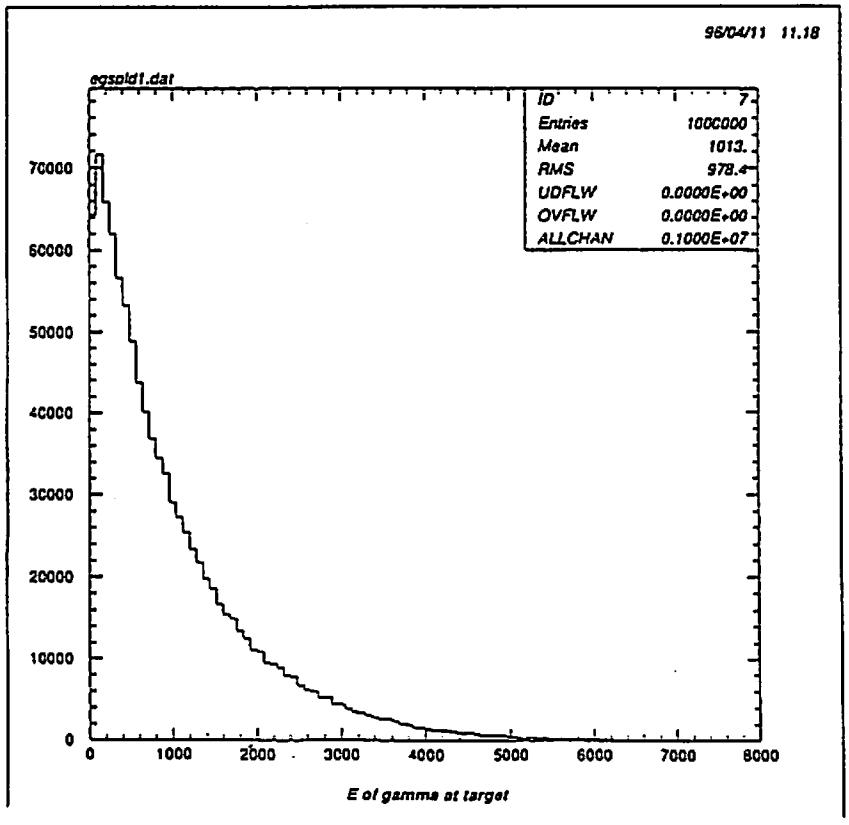

Fig.3 Energy distribution of pions and gammas.

a) The collimator

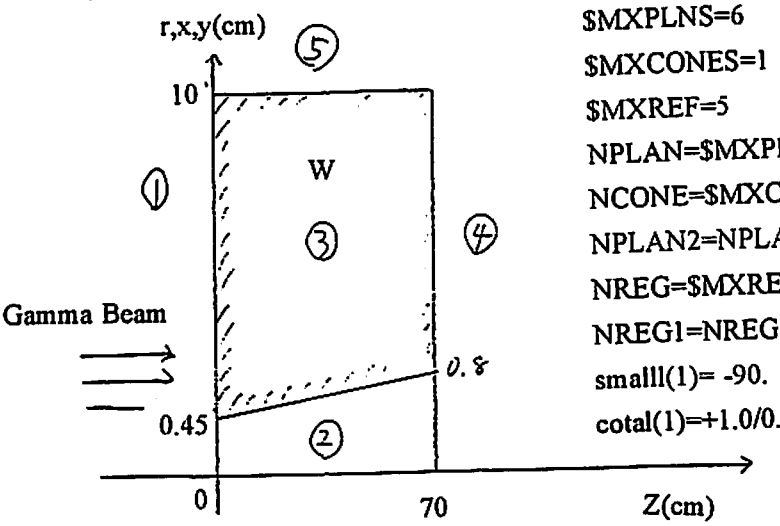

b) Energy distribution at the exit of the collimator

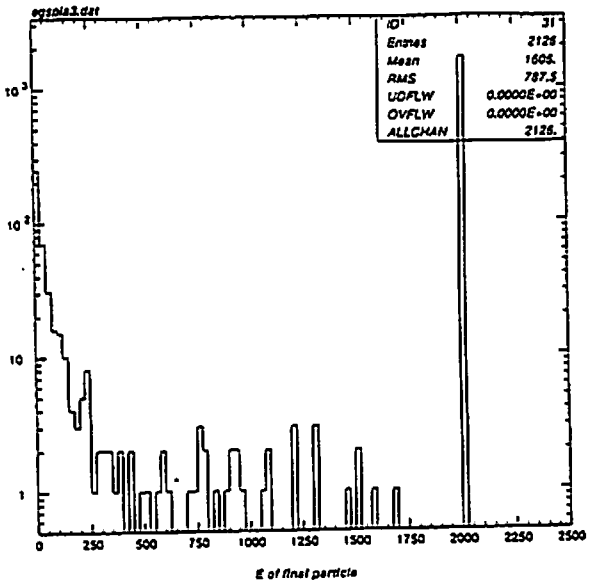

c) radial(x) distribution at the exit of the collimator

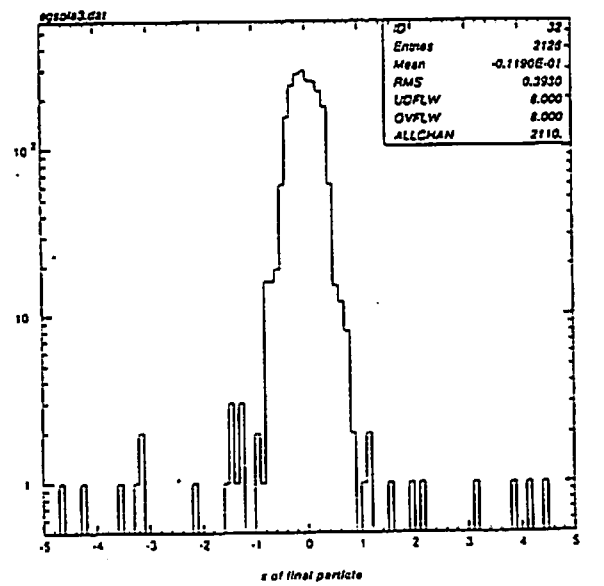

Fig.4 An example of the CONE type collimator.

a) The collimator

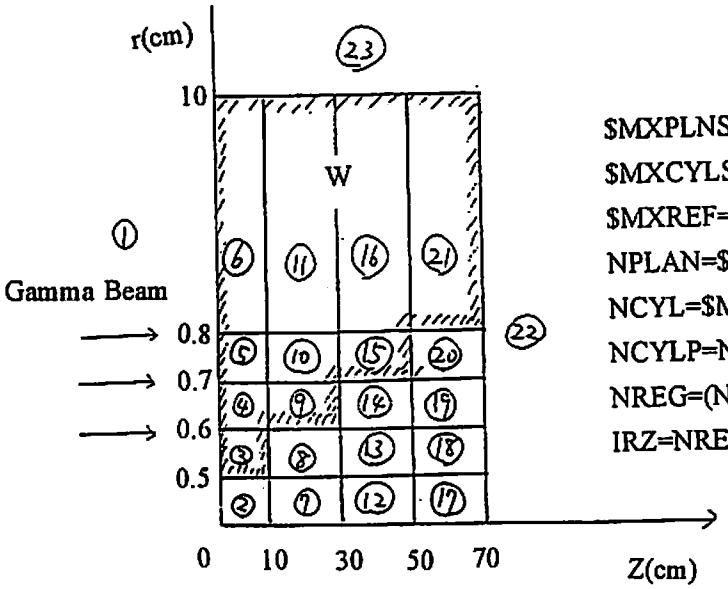

b) Energy distribution at the exit of the collimator

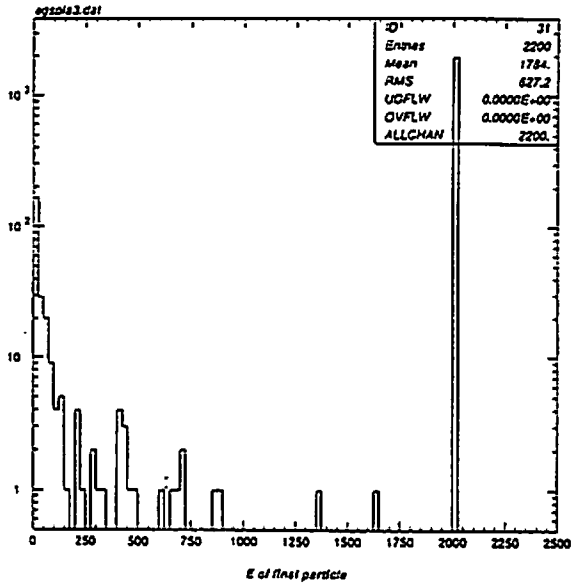

c) radial(x) distribution at the exit of the collimator

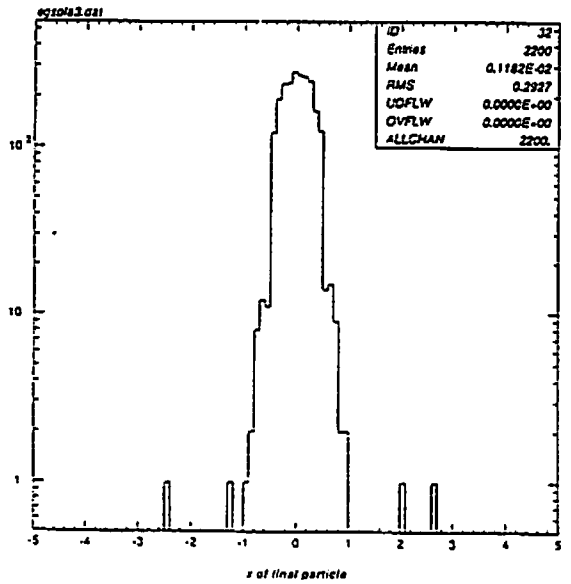

Fig.5 An example of the CYLINDER type collimator.

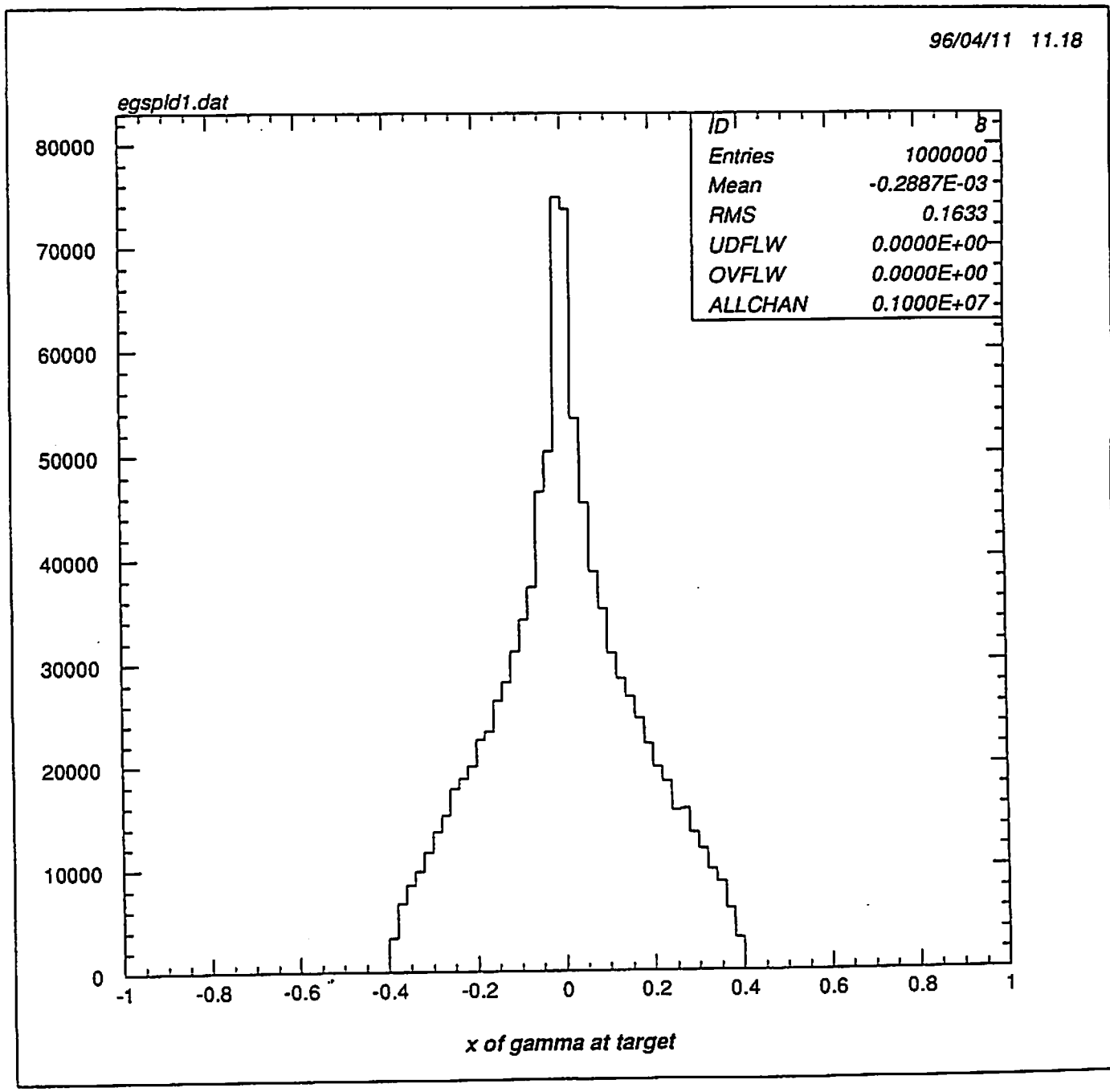

Fig.6 Radial(x) distribution of gammas at the production target.

Fig.7 The beam profiles at each step of the collimator system

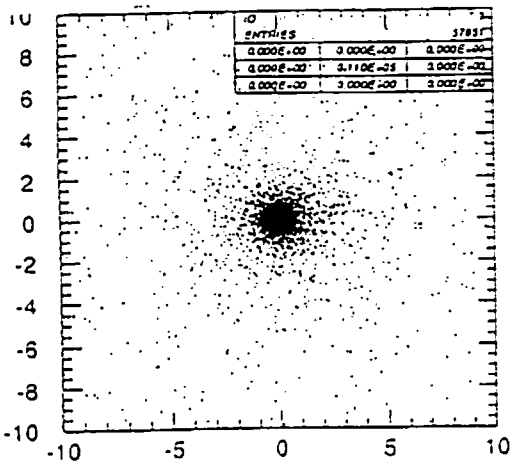

xe vs ye sum

1st Coll.(1.7m)

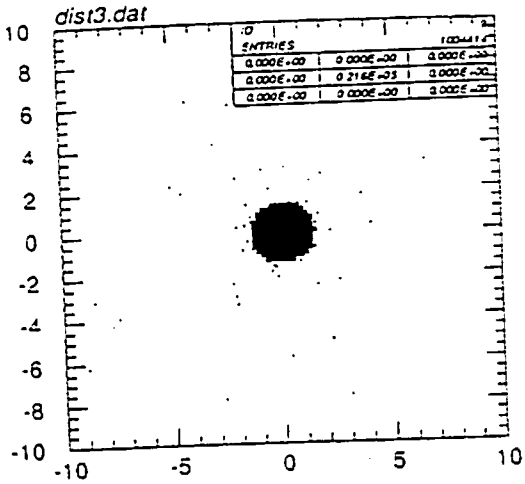

xe vs ye sum

4th Coll(6.9m)

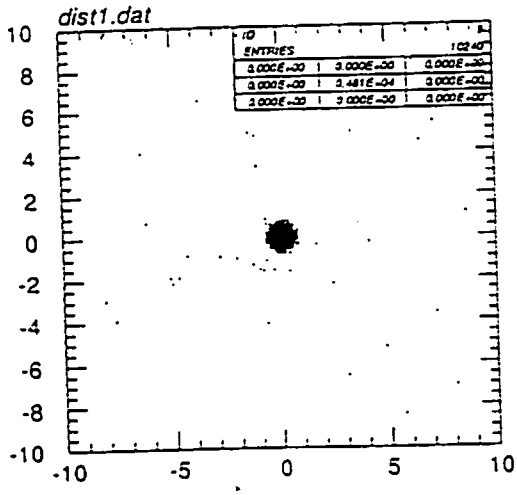

xe vs ye sum

2nd Coll.(3.4m)

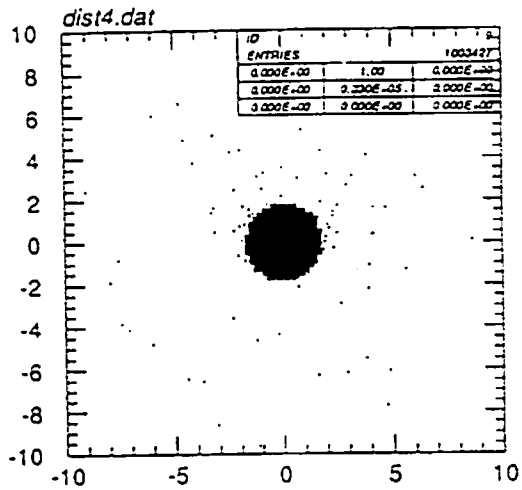

xe vs ye sum

5th Coll.(8.7m)

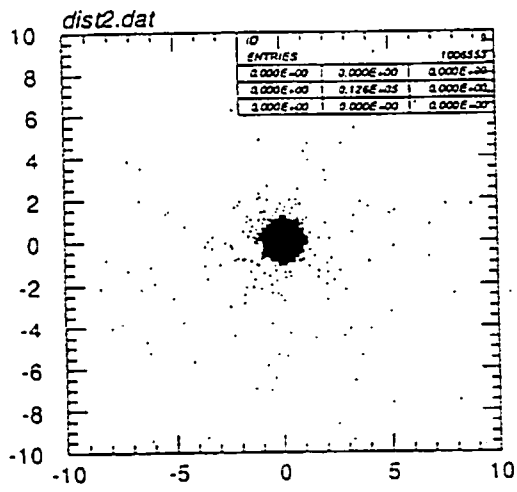

xe vs ye sum

3rd Coll(5.1m)

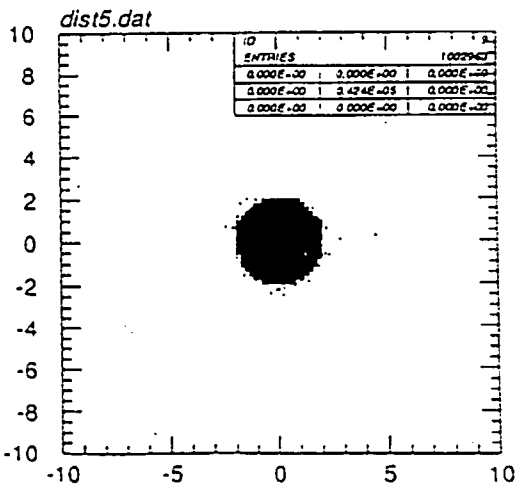

xe vs ye sum

6th Coll.(10m)

Fig.8 The beam profiles behind the collimator system

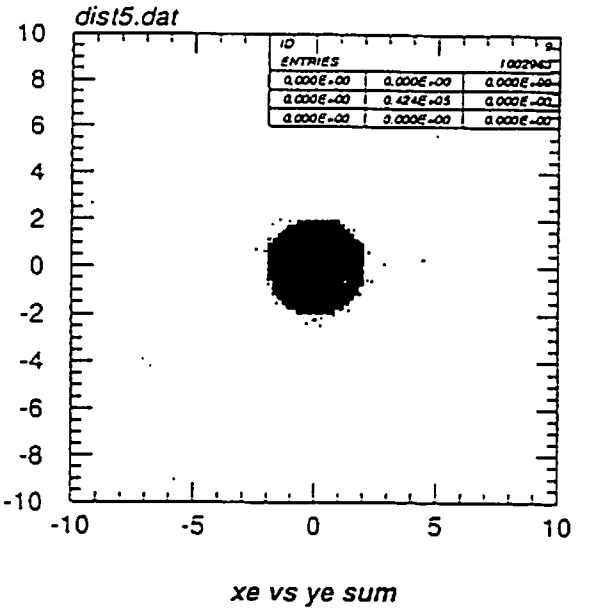

End ot the beam line
(10m from the target)

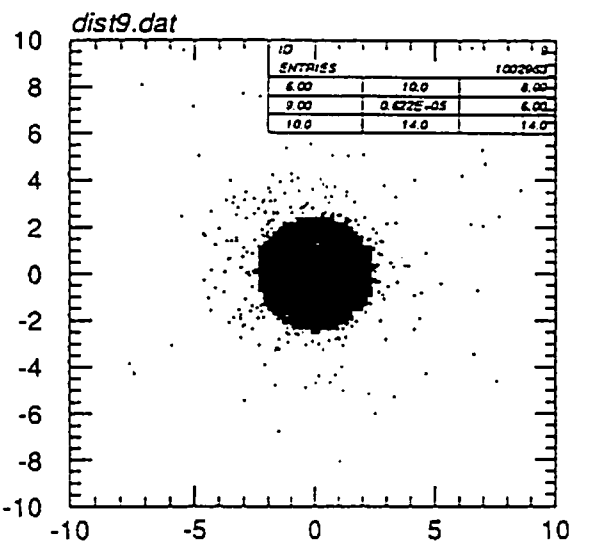

At the pre-detector front face
(12.15m from the target)

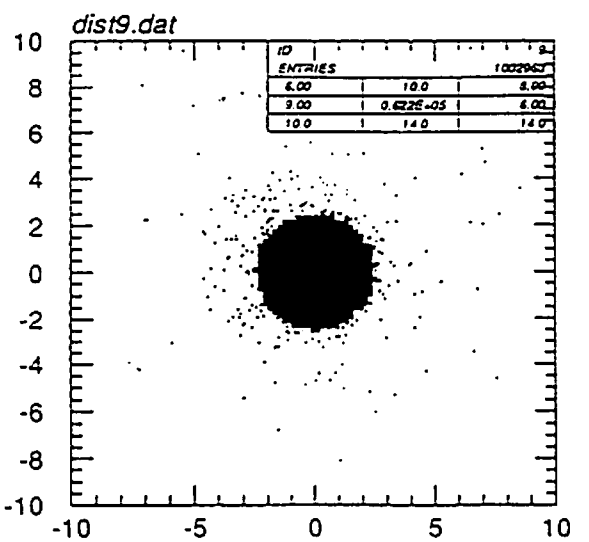

At the detector front face
(15.95m from the target)

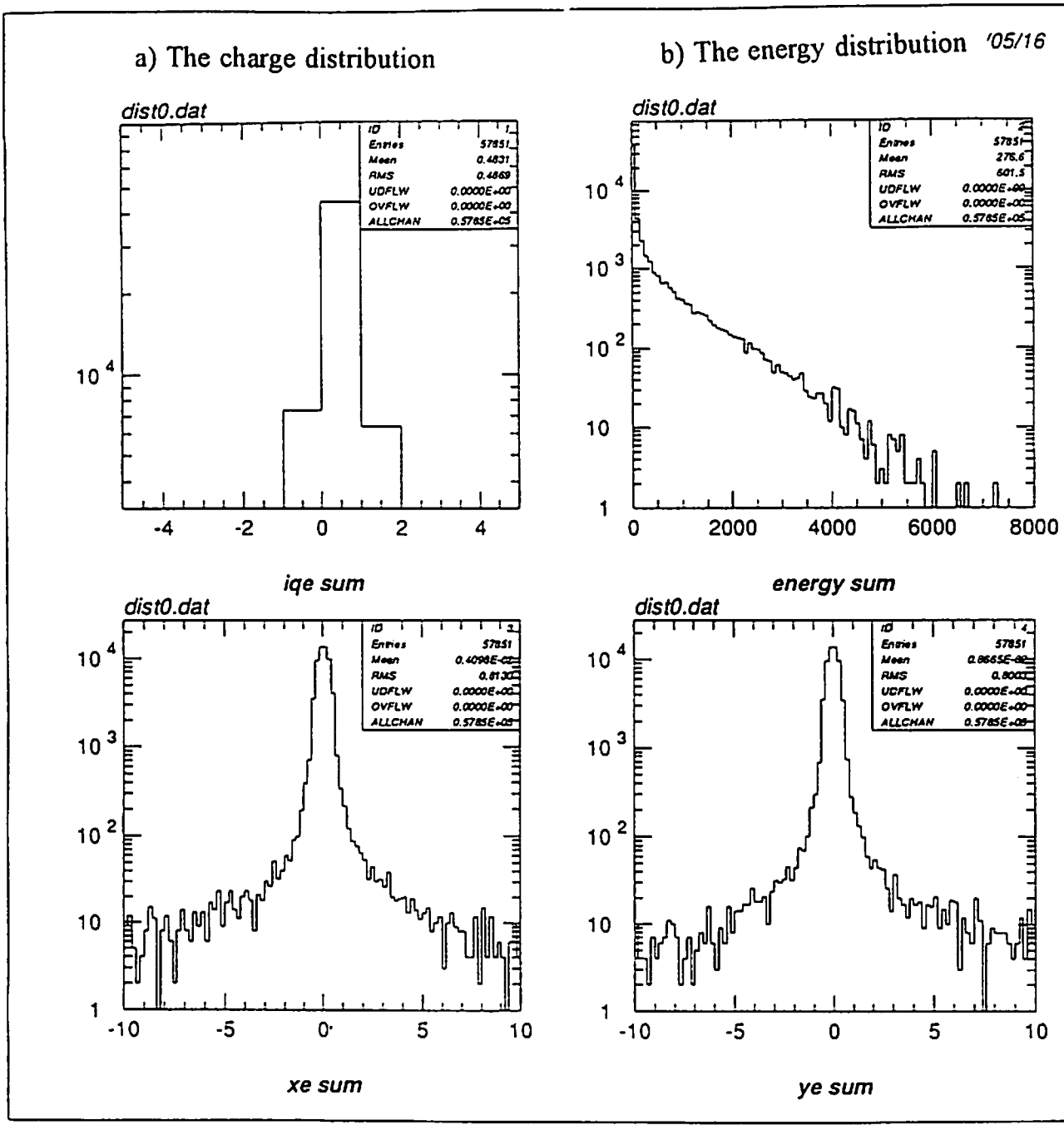

Fig.9 The beam characteristics at the exit of the first collimator.
In (a), -1 is for electrons, 0 is for gammas and +1 is for positrons.

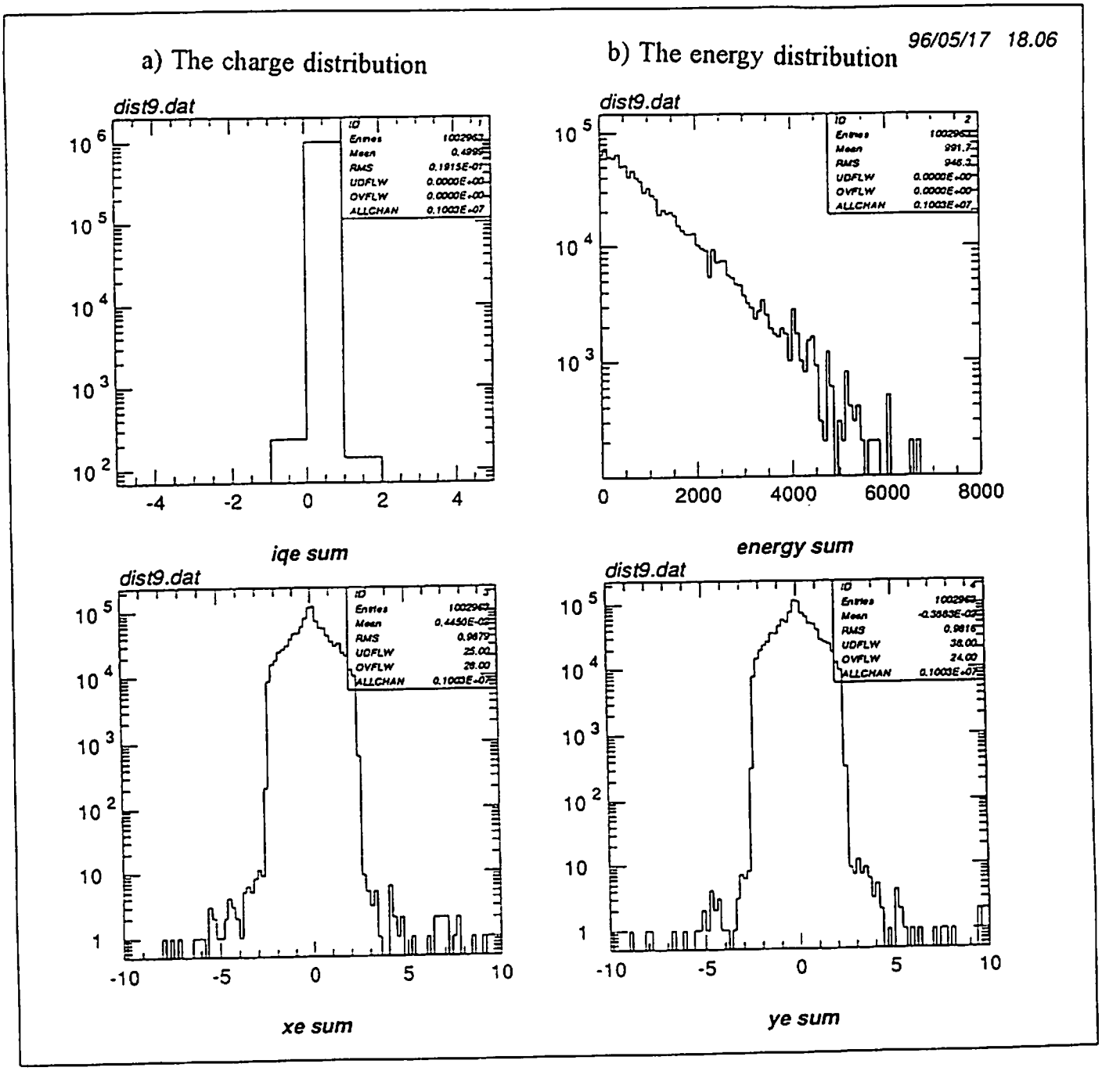

Fig.10 The beam characteristics at the experimental detector(5.95m behind the collimator system). In (a), -1 is for electrons, 0 is for gammas and +1 is for positrons.

a) Energy vs. x

b) Energy vs. charge

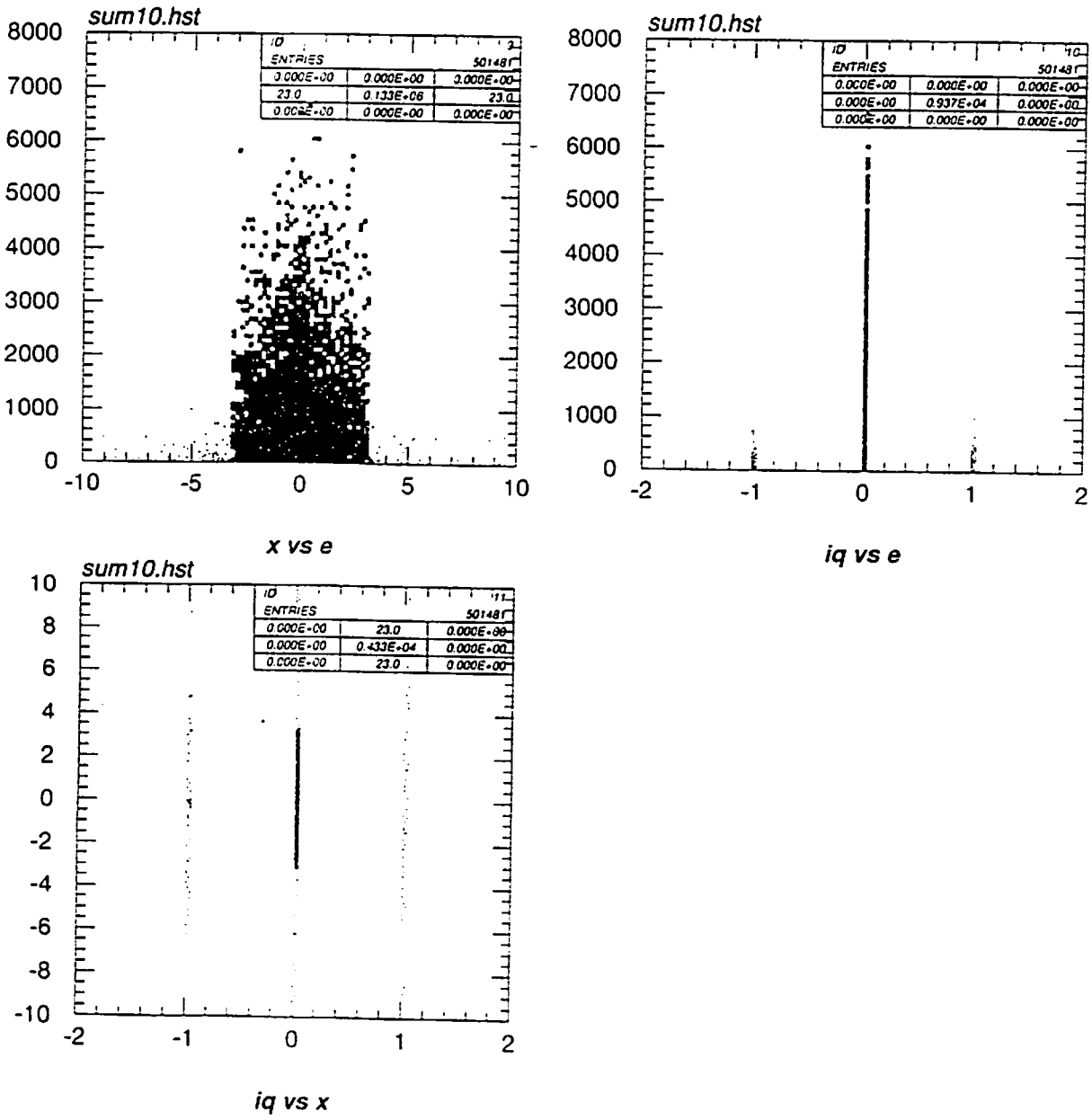

c) charge vs. x

Fig.11 Scatter plots for the beam at the experimental detector

CALCULATION OF DOSE FOR SKYSHINE RADIATION FROM A 45 MeV ELECTRON LINAC

M. HORI, M. HIKOJI, H. TAKAHASHI, K. TAKAHASHI,
M. KITAICHI, and S. SAWAMURA

Department of Nuclear Engineering, Hokkaido University
North 13, West 8, Kita-ku Sapporo, 060, Japan

I.Nojiri

Power Reactor and Nuclear Fuel Development Corporation
Tokai-mura, Naka-gun, Ibaraki 319-11, Japan

Abstract

Dose estimation for skyshine plays an important role in evaluation of environment around nuclear facilities. We performed calculations for the skyshine radiation from a Hokkaido University 45 MeV linear accelerator using a general purpose user's version of the EGS4 Monte Carlo Code. To verify accuracy of the code, the simulation results have been compared with our experimental results, in which a gated counting method was used to measure low-level pulsed leakage radiation. In experiment, measurements were carried out up to 600m away from the LINAC. The simulation results consist with the experimental values at the distance between 100 and 400 m from the LINAC. However agreements of both results up to 100 m from the LINAC are not so well because of the simplification of geometrical modeling in the simulation. It would be said that it is useful to apply this version to the calculation for skyshine.

1. Introduction

In a facility such as an electron linear accelerator is installed, dose estimations for skyshine have been one of important factors for environmental assessment around the facility. Despite of such importance, there are few benchmark data because of some difficulties of measurement of the dose around the facility. Since the radiation dose is very weak at far away from the facility, a strong intensive stationary radiation source, such as ^{60}Co, is need to measure the dose with good S/N ratios. But using a high intensive

stationary radiation source causes a serious problem to environments around such a facility. This difficulty could be prevent by using a pulsed radiation source with a gated counting system. For this reason it is necessary to develop the measurement system to obtain those experimental data, and also, to develop the calculation code applicable to the skyshine. In a facility of electron linear accelerator, radiation can be produced from accelerated electrons, bremsstrahlung and radio-activated materials such as concrete and air in a building. Radiation source for the skyshine can be considered as to be a leakage radiation from ceiling walls and stacks of the building. The purpose of this study is to investigate the skyshine using a general purpose user's version of the EGS4 Monte Carlo Code[1, 2] and verify capabilities of the program to the skyshine by comparing the simulation results with experimental data. The program has been developed to make the EGS4 easily usable to the analysis of nuclear facilities without requiring user-written subroutines and knowledge of language of MORTRUN3. By using this version, we perform calculations for the skyshine radiation from a 45 MeV electron linear accelerator installed at Hokkaido University. We also perform measurements of the skyshine dose up to 600 meters away from the LINAC. To our knowledge this is the first measurement of skyshine dose around a facility such as LINAC. Then those simulation results are compared with the experimental data to confirm capability of the version.

2. Skyshine from the 45MeV LINAC

Figure 1 shows shielding conditions of the accelerator room and the target room in the 45 MeV LINAC of Hokkaido University. These rooms are surrounded by concrete shields that maximal thickness is 3.5 m. The accelerator and the target room have 47 m in total length, 6.0 m in height and about 6.0 m in width. To produce bremsstrahlung, a Pb target with 9 mm in thickness is placed at 1.0 m in front of the electron beam exit. According to a periodical surveying around the area of the LINAC, the leakage radiation in operatin the LINAC mainly comes from the stack (shown in Fig. 1), which is conducted to the air-duct located at the upside of the target room. Therefore the leakage photon from the duct can be considered as a primary source of the skyshine radiation.

3. Measurements of skyshine

To measure a low-level pulsed leakage radiation, a gated counting system[3] was made. By adjusting a timing of sampling gate, only background radiation is reduced successfully. The electron LINAC was operated with 3 μs pulse duration and the frequency of 100 Hz. The gated pulse width was adjusted to 30 μs in the system. Hence the background counts can be reduced up to *ca.* 3×10^{-3}. The pulse signals synchronized with the electron beam emission were transmitted to the counting system with a coaxial cable. A NaI(Tl)

scintillation counter (with 3"ϕ × 3" crystal) was used as a detector. Measurements have been carried out up to 600 m away from the 45 MeV LINAC to the three directions (west, south and north). A total measurement points are 27. Experimental results are shown in Fig. 5. To prevent pile-up effects in NaI(Tl), the average current collected in the target is adjusted from 2 to 48 μA, depending on the measurement points. Experimental data in Fig. 5 are normalized based on a data for 48 μA. The skyshine exposure rates decrease with the distance from the facility up to r=400 m. However, since no remarkable differences are appeared in the values measured between 400 and 600 m, we have to pay more attention to the background radiation. This will be discussed in the next section.

4. Calculations of skyshine

Since it is important to evaluate an energy spectrum of the radiation source for the skyshine, we have carried out calculations with two steps. Firstly, calculations for the target room have been performed to get the energy spectrum around the stack. Next, by using this spectrum, calculations for the skyshine have been carried out.

4.1 Models and Methods

The geometry of the target room used for calculations by EGS4 is shown in Fig. 2. This model consists of a Pb target, regions of air-gas (in a target room and an air-duct), concrete walls and a 45 MeV electron source. A 45 MeV electron source is a disc-like shape with a radius of 0.25 cm. A thickness and radius of the cylindrical Pb target are 9.0 mm and 20 cm, respectively. By using this model, calculations of energy distribution at the stack have been carried out. Fig. 3 shows a schematic model for calculation of the skyshine dose rates. In this model, the radiation source is located at the stack of the facility. The source will spread upward with 180 degrees angle. All point detectors were located at 1.0 meters above the ground-level, and a photon fluence was calculated at each point detectors. Finally, the fluence was converted into normalized exposure rate to allow direct comparison with our experimental data.

4.2 Calculated results

The result of energy distribution at the air-duct by the EGS4 was shown in Fig. 4. The numbers of history were 1,000,000 in this calculation. It is found that the spectrum shows a peak close to 100 keV within a statistical errors. To prove the calculation results, we are planning to measure the dose in the vicinity of the funnel located at the top of the building. The skyshine dose rates were calculated up to 600 meters from the photon source by using the geometry in Fig. 3. Calculated results are presented in Fig. 5 with points. A parameter r is the distance from the source. The results of the simulation consist

well with the experimental results within 200 meters region. However, in the region of 400m far away from the facility, agreements of both results are not so well. The simulation results show smaller values than the experimental values. It may be due to a simplification of geometrical modeling in the simulation. In the calculation, we assumed that leakage photons from the air-duct are to be the only skyshine source. Therefore a better agreement could be expected when the photons penetrated the shield are taken into account. For example, effects of photons, which penetrate the roof of the accelerator or and the roof close to the Pb target, on the calculation results should be considered. We also think that exact evaluation of the background radiation at the distance between 400 and 600 meters would important in the measurement. We have previously done some calculations in the case of mono-energetic source. For comparison, the result 500 keV was also shown in Fig. 5. It is clear that the results for mono-energetic are underestimate of the experimental results, showing an importance of evaluating the energy spectrum.

5. Conclusion

We have measured skyshine radiation up to 600 meters from the 45 MeV linear accelerator using the gated counting system. To our knowledge this is the first measurement of the skyshine around an electron linear accelerator. However we may need to pay more attentions to the background radiation because exact evaluation of the background is consequent in measuring at far away from the source. We calculated the leakage X-ray at the air-duct on the electron LINAC using the general purpose user's version of the EGS4. The skyshine source spectrum was estimated though it contained some statistical errors. By using the leakage X-ray as the source of skyshine, the skyshine exposure rates were calculated up to 600 meters away from the LINAC. Simulation results agree well with the experimental values up to 200 meters. More good agreement with both results could be obtained when an improved skyshine source is applied.

Acknowledgment

We would like to thank to Prof. H. Hirayama in National Laboratory for High Energy Physics for his kind help and advice.

References

[1] W. R. Nelson, H. Hirayama and D. W. O. Rogers, The EGS4 Code System, SLAC-Report-265(1985)

[2] O. Narita, I. Nojiri and T. Momose, The Development of a General Purpose User's Version of the EGS4 Code System(II)

[3] Y. Ozawa, et al., Nihon-Genshiryoku-Gakkai shi (J. At. Energy. Soc. Japan), 5[3], 190(1963)

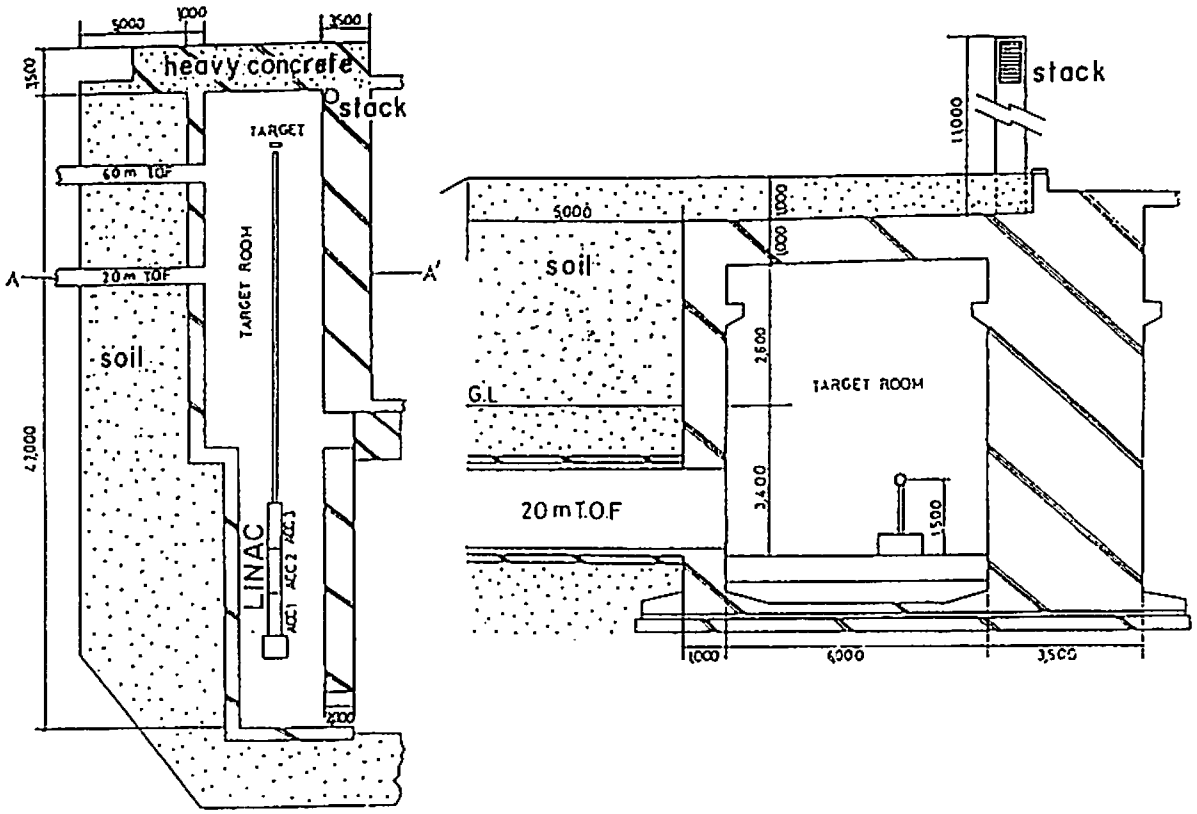

Fig. 1 Shielding Condition of the Linac

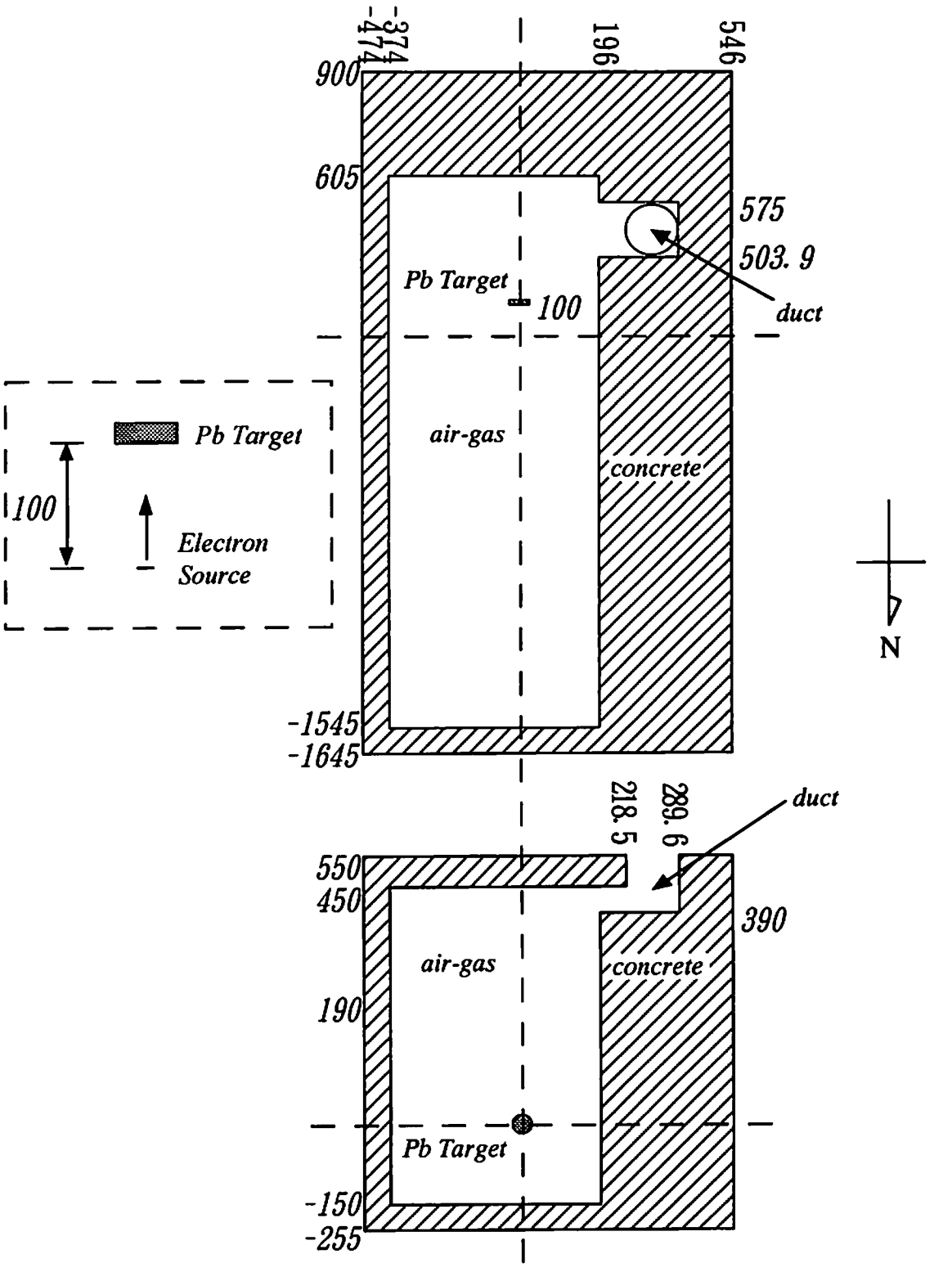

Fig. 2 Geometry of the Target Room by the EGS4(unit:cm)

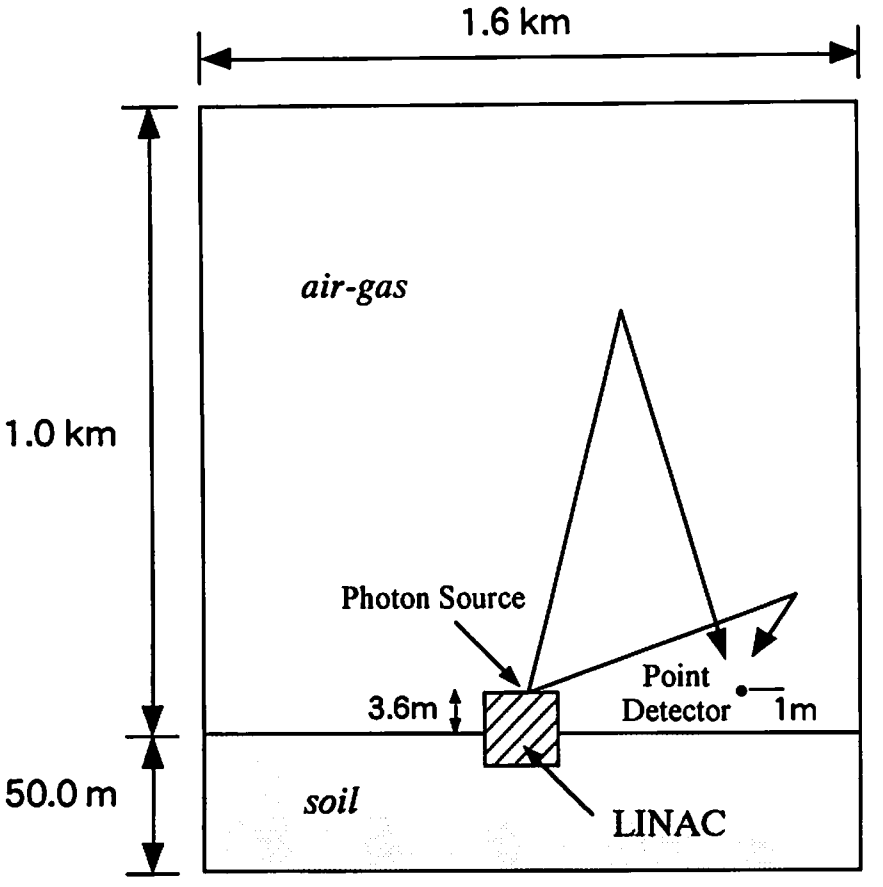

Fig. 3 Skyshine Dose Rates Calculated Model

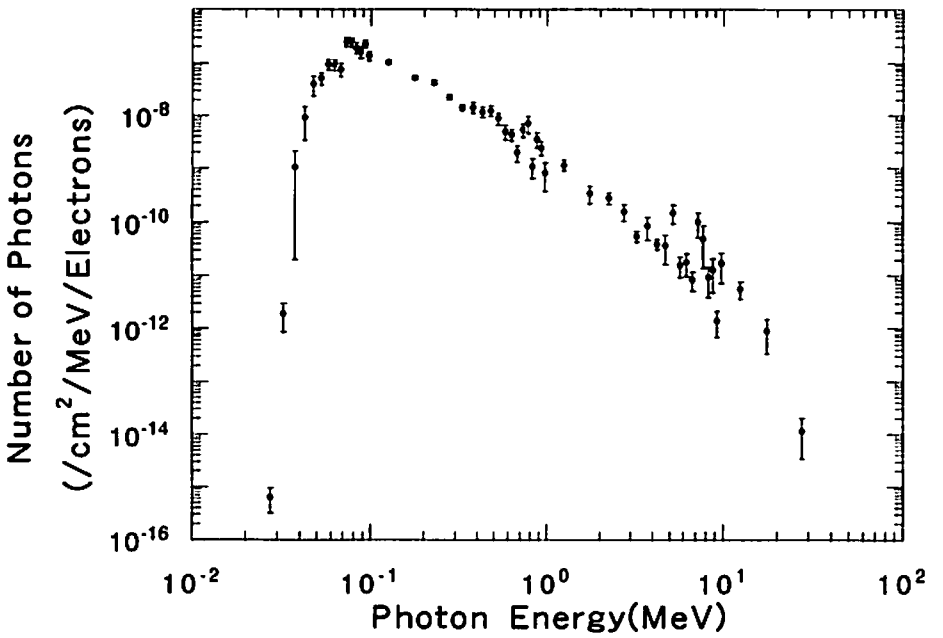

Fig. 4 Photon Energy Distribution at the Air-Duct

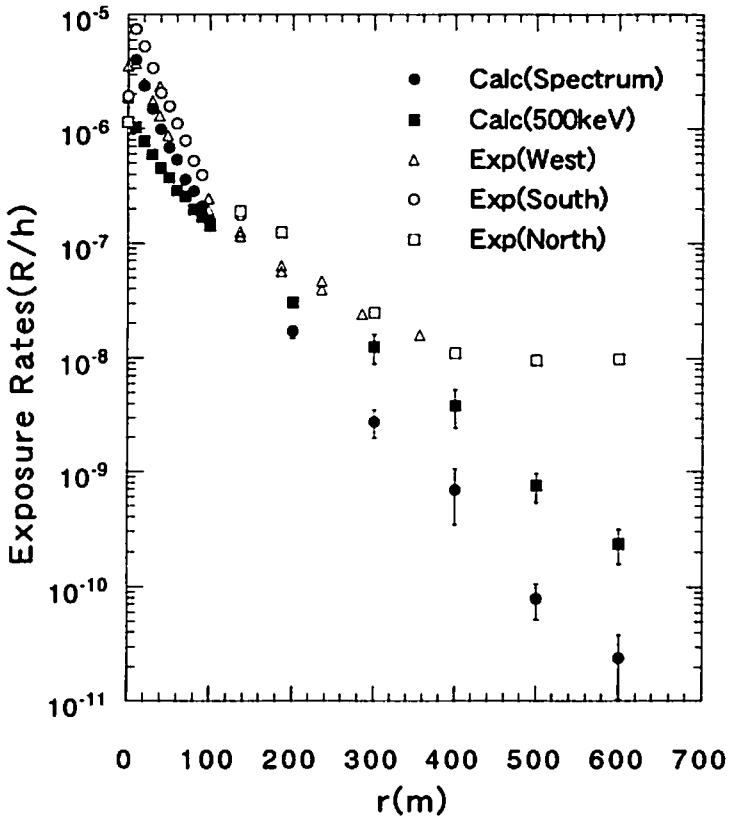

Fig. 5 Calculated and Measured Skyshine Exposure Rates

CONCEPTUAL DESIGN OF BEAM DUMP FOR HIGH POWER ELECTRON BEAM

H. TAKEI and Y. TAKEDA[1]

Power Reactor and Nuclear Fuel Development Corporation (PNC)
4002 Narita, Oarai-machi, Ibaraki-ken 311-13 Japan

Abstract

A high power CW (Continuous Wave) electron linac has been developed at PNC and its injector section has been completed in 1996. This paper presents the conceptual design of beam dump for a high power low energy beam (200 kW of 10 MeV electron). It has a Ring and Disk structure. The thermal analysis, stress analysis showed that 200 kW electron beam could be securely stopped in the beam dump. The temperature rise at highest position was estimated to be 343 degree.

1. Introduction

Design and construction of a high power CW electron linac to study feasibility of nuclear waste transmutation [1] was started in 1989 at PNC. The injector has been completed and started its operation at 3.5 MeV beam energy in summer 1996 and the whole facility is planned to be commissioned at 1997. Main specification of the accelerator is shown in Table 1.

Table 1 Main specification of the electron linac

Energy	10 MeV
Maximum Beam Current	100 mA
Average Beam Current	20 mA
Pulse Length	0.1~4 msec
Pulse Repetition	0.1~50 Hz
Duty Factor	0.001~20 %
Norm. Emittance	50 π mm mrad *
Energy Spread	0.5 % *

* estimated value by simulation

[1]Guest Scientist from Paul Scherrer Institut (PSI), Switzerland

As the beam is a considerably high power and of low energy electron, the average power density of heat generation due to the energy deposition is quite large, so that it is of extreme importance to realize the beam dump to be secured by removing the heat very efficiently. At the same time, radiation shielding of the beam dump is also of the major concern.

2. Design

The conceptual design of the beam dump is based on the following design criteria:

(1) to disperse the beam by magnet in front of the beam entry

(2) to stop the beam part by part in spatially separated blocks

(3) to minimize the induction of radioactivity

The first criteria is for making the power density smaller by defocusing/spreading the beam. It is also assuring to avoid mishaps of the pin point beam hitting the component. The second criteria makes also a reduction of power deposition in a small region of the beam dump. The third criteria eliminates the use of water to stop the beam. Liquid target does necessarily increase the total inventory of the radioactive materials. The concept of the present design is, as shown in Figure 1, Ring and Disk (RD) system : The part where energy is deposited consists of 17 rings and 5 disks (thickness of 5 cm). Each plate is made from OFHC (Oxygen Free High-purity Copper). All the rings have different inside diameters (the beam runs inside this ring.). The frontmost ring has the inside diameter of 19.6 cm and other rings have smaller diameter with increment of 1.2 cm from upstream to downstream.

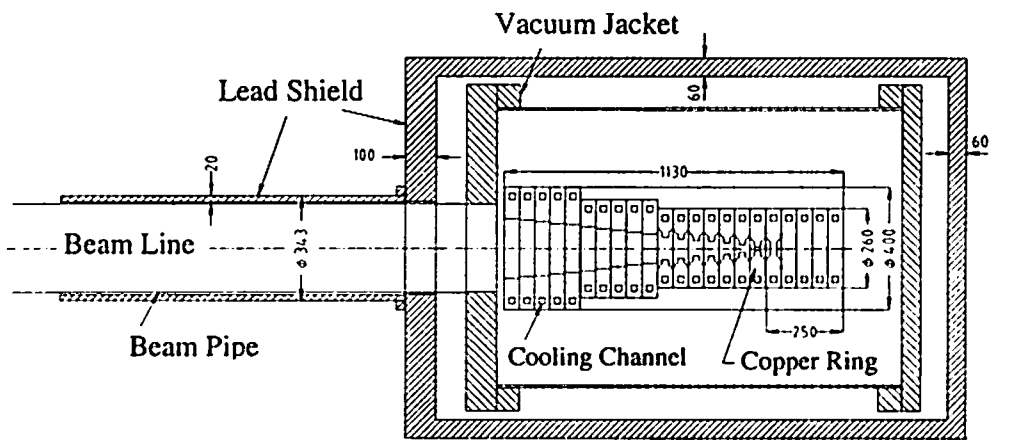

Fig. 1. Beam Dump in cross-section

The beam enters into the cylindrical vessel through a dispersion magnet which is located 2 m front of rings. Since the beam has spatially a Gaussian profile, the inner front edges of rings stop the narrow annual lobe of the beam, from outside as going to the backward. Finally the beam is stopped by the disk set at the backend of the block. Figure 2 is a front view of the inner front edges.

These rings and disks are formed into 4 modular units. Each module is electrically insulated from each other in order to measure the beam current deposited on them. It can be replaced/exchanged as a unit. In a module a cooling water flows in series from ring to ring. In order to reduce radiolysis of cooling water and to eliminate the vacuum window between the beam dump (target) and the accelerating tube, cooling water is not exposed to direct incident electron beam.

These modules form a total target block and it also electrically insulated from the main body of the beam dump. A total view of this target block is given in Figure 3 and the PNC beam dump is shown in Figure 4. The problem of connecting between the beam dump and the accelerator (the pressure difference between 1×10^{-5} torr and 1×10^{-7} torr in the accelerating tube) was solved by using a differential pumping stations and a low conductance beam transport tube.

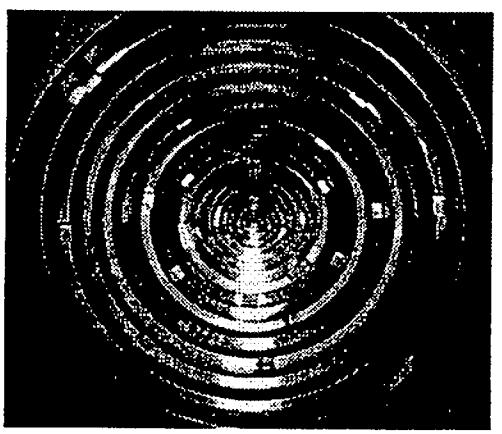

Fig. 2. A front view of the inner front edges

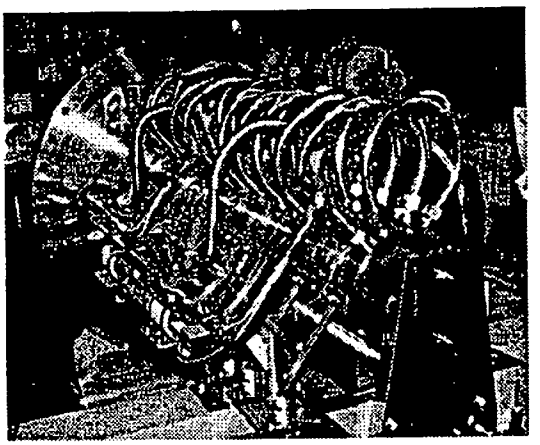

Fig. 3. A total view of target block

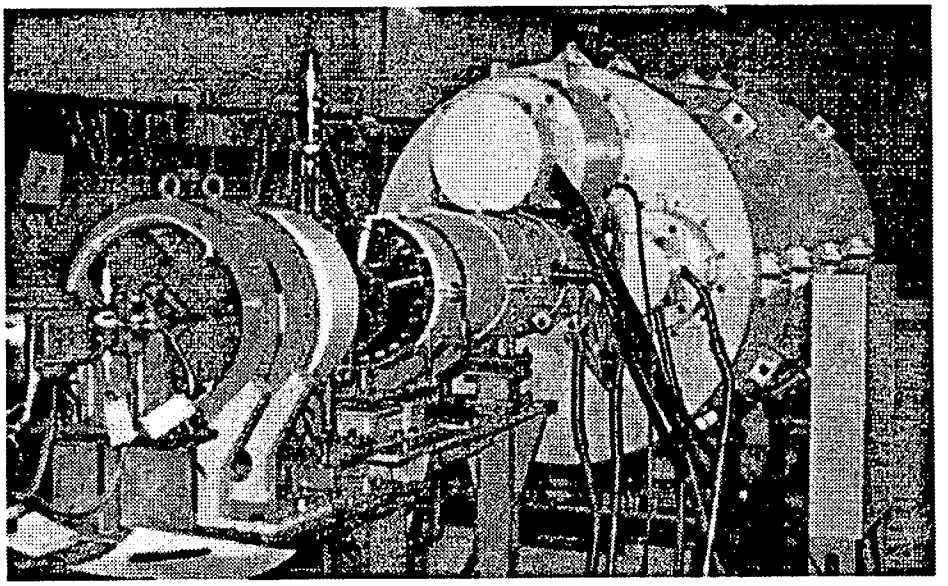

Fig. 4. View of the PNC beam dump

3. Thermal and Stress Analysis

Several computer codes were used in order to estimate the temperature rise and the stress of rings with full beam power. This calculation assumed that the transverse beam intensity is Gaussian distribution and the electron is injected to the target block with the angle of incidence varied between 0° and 3°.

Firstly, the power density in the target block is calculated using the EGS4 [2] code. The EGS4 code performs Monte Carlo simulations of the radiation transport of electrons, positrons and photons in any materials. Then we applied the PRESTA algorithm (Parameter Reduced Electron-Step Transport Algorithm)[3], which was developed by Bielajew and Rogers to improve the electron transport in EGS4 in the low-energy region. The maximum power density was estimated to be 2.2 kW/cm^3.

Using the power densities from the EGS4, we proceeded to the thermal analysis using the finite element method code ANSYS [4]. Examples of the results of the analysis are shown in Figures 5 and 6. They are cross-sectional views of a ring in which stress is estimated to become maximum. The results predicted that the maximum temperature rise in the ring is at the inner front edge of ring and is 343 degree, and peak stress of 2.3 kg/mm^2.

Since the Von Mises stress exceeds the yield stress of copper (0.63 kg/mm^2), a plastic deformation might be induced over a major portion of the ring. As it is considered that the thermal stress cracking could be generated by this deformation, we design the beam dump such a deformed disk is easily replaced with a new one.

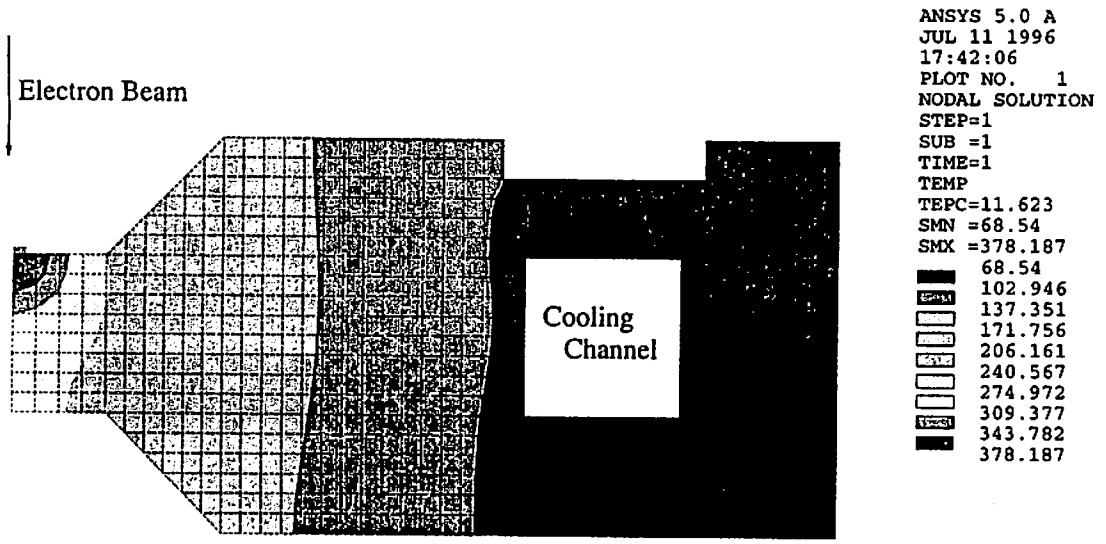

Fig. 5. Thermal analysis of a ring

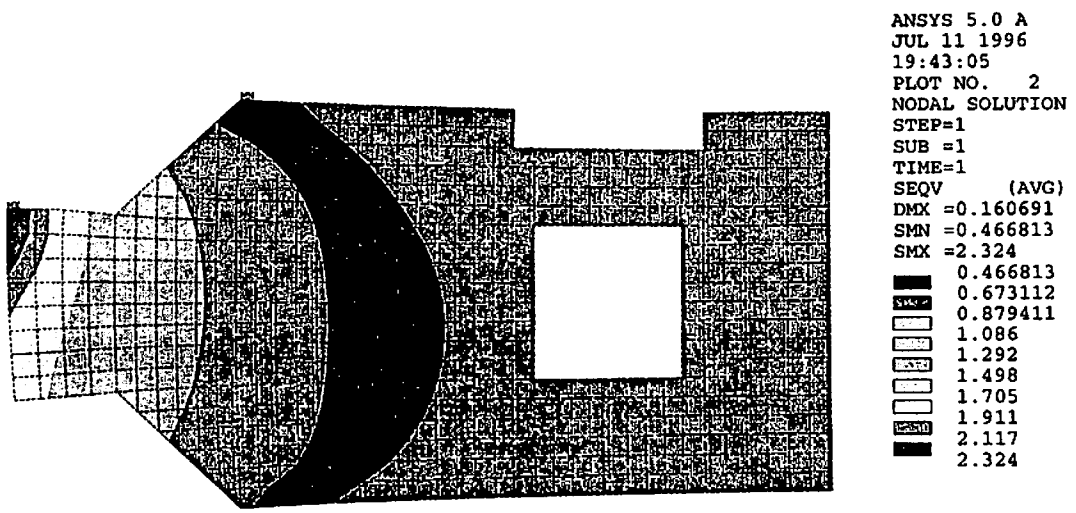

Fig. 6. The Von Mises stresses for the heat loads calculated with ANSYS

4. Photon Production

The energy distribution of photons (γ-rays) generated by incident electrons in the target block are studied using the EGS4 code. Figure 7 shows the relationship between its energy E and the scattering angle of the photon θ, where θ is the angle from the incident direction of electron beam.

Electrons are particularly susceptible to a large angle deflection by scattering from nuclei and they are backscattered out of the target block. In this context, Figure 7 shows

the concentration of backscattered photons in the direction of 180°. A preliminary estimate of the absorbed dose rate in the backward direction (180°) at 1 m is 9000 Gy/h with full beam power.

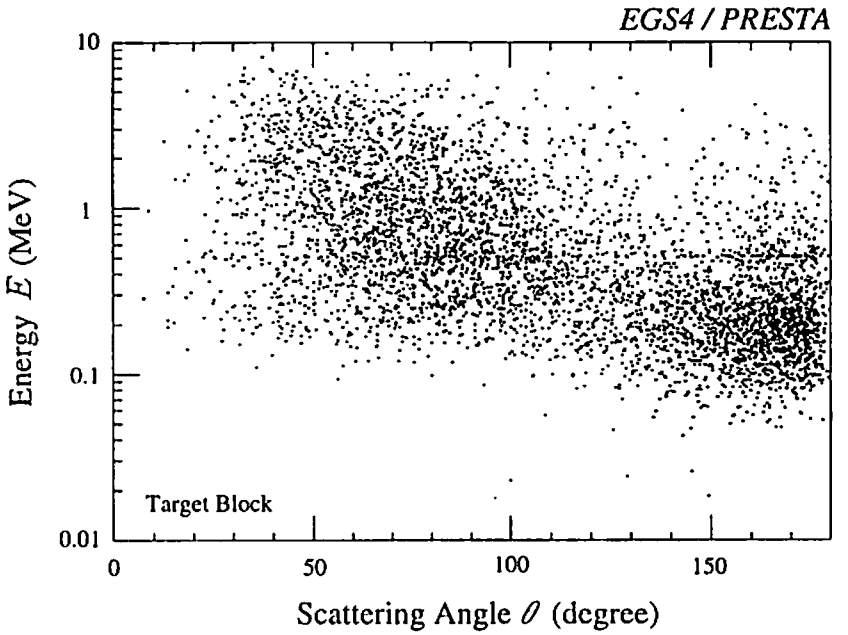

Fig. 7. Correlation between the photon energy E and the scattering angle θ

5. Conclusion

A beam dump at PNC, employing the Ring and Disk system, has been designed for the high power low energy beam (200 kW of 10 MeV electron). The beam could be stopped at the inner edge of the rings which are cooled by water. The maximum power density in the target block is 2.2 kW/cm^3 with full beam power assuming Gaussian distribution of the transverse beam intensity. The maximum temperature rise in the ring (at the inner front edge of ring) is estimated to be 343 degree.

References

[1] S. Toyama *et al.*, *Transmutation of long-lived Fission Product (^{137}Cs, ^{90}Sr) by a Reactor-Accelerator System*, Procceeding of 2nd International Symposium on Advanced Energy Research (1990).

[2] W. R. Nelson, H. Hirayama and D. W. Rogers,*THE EGS4 CODE SYSTEM*,SLAC-Report-265, December 1985.

[3] A. F. Bielajew and D. W. O. Rogers, *PRESTA: The Parameter Reduced Electron-Step Transport Algorithm for electron monte carlo transport*, Nucl. Instr. and Meth., **B18** (1987) 165.

[4] ANSYS, Ver. 5.0a, Swanson Analysis Systems. Inc.